The Dissertation Committee for Taylor D. Niehues
certifies that this is the approved version of the following dissertation:

Achieving Human-Like Dexterity in Robotic Hands: Inspiration from Human Hand Biomechanics and Neuromuscular Control

Committee:

Ashish D. Deshpande, Supervisor

James Sulzer

Raul G. Longoria

Raymond J. King

Achieving Human-Like Dexterity in Robotic Hands: Inspiration from Human Hand Biomechanics and Neuromuscular Control

by

Taylor D. Niehues

DISSERTATION

Presented to the Faculty of the Graduate School of

The University of Texas at Austin

in Partial Fulfillment

of the Requirements

for the Degree of

DOCTOR OF PHILOSOPHY

THE UNIVERSITY OF TEXAS AT AUSTIN

December 2017

Acknowledgments

I would first like to acknowledge and thank my advisor, Ashish Deshpande, who has been a constant source of guidance for not just my research, but also for life as a graduate student and for my career options going forward. Your advice and enthusiasm for research is part of what encouraged me to pursue a doctorate in the first place, and I'm very thankful for the opportunities you've given me.

To my committee members and professors at UT, who have guided me and given me the strong engineering knowledge base that is the foundation upon which this dissertation is built.

To my fellow grad students and researchers at UT, NASA, and Oculus Research. The open research discussions and collaborations we've had has positively shaped my views of the world around us, and seeing others' enthusiasm and excitement for innovative robotics and biomechanics research has been hugely motivating to me throughout my graduate career.

To Prashant, Gray, Jack, Stephen, Patrick, and everyone else who joined in our after-work happy hours. I've always looked forward to the company, the beers, and the wide, unpredictable range of conversations we might find ourselves a part of.

And finally, to my wife, Kristin, and my family, for your support and encouragement throughout my extended education. I would not be where I am today without you, and am excited for the future knowing that you will be beside me through it all.

Achieving Human-Like Dexterity in Robotic Hands: Inspiration from Human Hand Biomechanics and Neuromuscular Control

Publication No. _____

Taylor D. Niehues, Ph.D.
The University of Texas at Austin, 2017

Supervisor: Ashish D. Deshpande

The human hand's unique biomechanical structure and neuromuscular control combine to produce amazing dexterous capabilities in a way that is still not fully understood. The Anatomically Correct Testbed (ACT) hand is a robotic system that is designed as a physical simulation of the human hand, and can help us examine and potentially uncover the roles of biomechanics and neural control in achieving dexterity.

In this dissertation, I utilize the ACT hand and other robotic systems to explore the underlying sources of human hand dexterity, with the goal of understanding the fundamental differences between robotic and human hands in terms of (i) mechanical joint/tendon structure and (ii) control strategies. To begin, I develop comprehensive mechanical models that describe the musculoskeletal and tendon mechanics of the fingers and thumb of the human hand. Then, I work to isolate the contributions of biomechanical structure and neuromuscular control toward human dexterity.

I have developed and implemented control strategies for achieving fine object manipulation first with the robotic hand of a space humanoid, Robonaut 2, and then with the ACT hand. I examined the unique control challenges, including uncontrollable joints and the requirement of accurate internal models, that arise due to the human hand's complex musculotendon structure and the potential advantages offered by the human hand's design, such as passive joint coupling to facilitate grasp shape adaptation and force production capabilities that are ideally suited for common manipulation tasks. Finally, inspired by the neuromuscular control strategies of the human hand, I have developed a novel hierarchical control strategy for the ACT hand and experimentally demonstrated improved grasp stability and manipulation capabilities compared to conventional robotic control laws. Through an in-depth exploration of human hand biomechanics and neuromuscular control, theoretical control analysis of robotic and human hands, and experimental demonstration of fine object manipulation, this work uncovers crucial insights into the sources of human hand dexterity that have the potential to drive innovative design and control strategies and bring robotic and prosthetic hands closer to human levels of dexterity.

Table of Contents

Acknowledgments iv

Abstract v

List of Tables xi

List of Figures xii

Chapter 1. Introduction 1

1.1 Motivation and Goals . . . 1

1.2 Comparing the Design and Control of Existing Robotic Hands and the Human Hand System . . . 2

1.2.1 State of the Art Robotic Hand Designs . . . 3

1.2.2 Human Hand Musculoskeletal Structure . . . 4

1.2.3 Robotic Control Strategies for Dexterous Manipulation . . . 5

1.2.4 Human Neuromuscular Control . . . 6

1.2.5 The Anatomically Correct Testbed (ACT) Hand . . . 6

1.3 Contributions . . . 7

1.4 Dissertation Outline . . . 9

Chapter 2. Mechanical Modeling of the Human Hand 10

2.1 Modeling the Human Finger Extensor Mechanism . . . 10

2.1.1 Modeling of Interconnected Tendon Systems . . . 13

2.1.1.1 Force/Torque Relationships . . . 13

2.1.1.2 Tension Distribution . . . 14

2.1.2 Case Study: Human Finger Simulation Model . . . 17

2.1.2.1 Posture-Dependent Effective Moment Arms . . . 18

2.1.2.2 Changing Tension Distribution . . . 21

2.1.3 Experimental Validation of Tendon Modeling Framework . . . 21

2.1.3.1 Experimental Setup . . . 21

2.1.3.2 Model Parameter Identification . . . 23

2.1.3.3 Forward Problem: Fingertip Force Prediction 24
2.1.3.4 Inverse Problem: Muscle Force Prediction 27
2.1.3.5 Cartesian Force Control using Complex Tendon Model 28
2.1.4 Discussion 30
2.2 Variable Moment Arms and Thumb-Tip Force Production of the Human-Like ACT Thumb 30
2.2.1 Methods 32
2.2.1.1 Muscle Moment Arms 32
2.2.1.2 Thumb-Tip Forces 35
2.2.2 Results 36
2.2.2.1 Muscle Moment Arms 36
2.2.2.2 Thumb-Tip Forces 38
2.2.3 Discussion 39
2.3 Summary of Human Hand Mechanical Modeling 44

Chapter 3. Dexterous Manipulation with the Anthropomorphic Robonaut 2 Hand 45
3.1 Generalized Model of Tendon-Driven Robot 47
3.2 Cartesian Control of R2 Fingers and Thumb 48
3.2.1 Joint Torque Controller 49
3.2.2 Cartesian Stiffness Controller 50
3.2.2.1 Thumb 51
3.2.2.2 Primary Fingers 51
3.3 Object Manipulation Controller 53
3.4 Experimental Manipulation Results 56
3.4.1 Object Rotation 58
3.4.2 Object Translation 58
3.4.3 Disturbance Response 60
3.5 Discussion 62

Chapter 4. Dexterous Manipulation with the Anatomically Correct Testbed Hand 64
4.1 Kinematic Modeling 65
4.1.1 ACT Hand Design Upgrades 65
4.1.2 Muscle Moment Arms 68
4.1.3 Joint Posture Estimation 69

4.1.4 Joint to Fingertip Modeling . . . 70
4.2 ACT Hand Control . . . 70
4.2.1 Muscle Force Control . . . 71
4.2.2 Index Finger Control . . . 73
4.2.2.1 Joint Torque Control . . . 74
4.2.2.2 Joint Stiffness Control . . . 74
4.2.2.3 Cartesian Fingertip Force Control . . . 75
4.2.2.4 Conditional Controllability of DIP Joint . . . 78
4.2.2.5 End-tip Cartesian Stiffness Control . . . 81
4.2.3 Thumb Cartesian Control . . . 81
4.2.4 Fine Manipulation Control . . . 84
4.3 Discussion . . . 89
4.3.1 Tendon Structure and Joint Controllability . . . 89
4.3.2 Thumb Control Space . . . 90
4.3.3 Functionality of Human Hand Structure for Coordinated Manipulation . . . 91

Chapter 5. Human-Inspired Control of the ACT Hand 93
5.1 Stiffness Transformations . . . 95
5.1.1 Passivity Analysis . . . 96
5.1.1.1 Effect of Robotic Hand Design on Grasp Stability . . . 97
5.1.1.2 Effect of Task Parameters on Grasp Stability . . . 98
5.2 Object-Space Stiffness Control . . . 98
5.2.1 Control Law . . . 98
5.2.2 Experimental Testing with the ACT hand . . . 99
5.3 Muscle-Space Stiffness Control . . . 103
5.3.1 Inspiration from Human Neuromuscular System . . . 103
5.3.2 Control Design . . . 104
5.3.3 Experimental Results . . . 106
5.4 Discussion . . . 109

Chapter 6. Conclusions 110
6.1 Future Work . . . 111

Appendices 113

Appendix A. ACT Hand Joint Kinematics **114**
A.1 Index Finger 114
A.2 Thumb 115

Appendix B. Object-Space Transformations and Control **116**
B.1 Grasp Matrix 116
B.2 Internal Grip Force Calculation 117
B.3 Stiffness Transformation 118

Bibliography **120**

Vita **133**

List of Tables

2.1 Tendon moment arms for human finger model. 18
2.2 Experimentally collected ACT thumb-tip force data 38
2.3 Sensitivity analysis of thumb-tip force production 42

3.1 Description of generalized variables for tendon-driven robotic hands. . 47
3.2 Robonaut 2 controller parameters. 57

A.1 Parameters for a kinematic model of the ACT index finger. 114
A.2 Parameters for a kinematic model of the ACT thumb. 115

List of Figures

2.1 Human finger schematic . . . 11
2.2 Schematic of junction between muscle and connecting tendons . . . 15
2.3 Posture-dependent effective moment arms of extensor mechanism muscles. . . . 19
2.4 Human finger model simulation. . . . 20
2.5 Robotic finger testbed with customizable tendon routing . . . 22
2.6 Parameter identification to correctly replicate finger IP coupling . . . 23
2.7 Experimental validation: forward model prediction . . . 26
2.8 Experimental validation: inverse model prediction . . . 28
2.9 Experimental validation: Cartesian force control . . . 29
2.10 Musculoskeletal structure of the ACT thumb . . . 33
2.11 ACT thumb moment arms for nominal and adjusted models . . . 37
2.12 ACT thumb-tip force contributions from each muscle in key pinch posture 40
2.13 ACT thumb-tip force contributions from each muscle in opposition pinch posture . . . 41

3.1 The Robonaut 2 (R2) upper body system . . . 46
3.2 Block diagram of complete R2 control system for achieving object manipulation . . . 53
3.3 The R2 hand rotating an object about the z-axis . . . 58
3.4 The R2 hand translating an object laterally . . . 59
3.5 The R2 hand translating an object vertically . . . 60
3.6 The R2 hand maintaining a fixed object position while rejecting externally applied disturbances . . . 61

4.1 Index finger and thumb of the Anatomically Correct Testbed (ACT) hand . . . 66
4.2 Custom tendon tension sensor design . . . 71
4.3 Actuator force control capabilities with and without tension feedback 73
4.4 Joint stiffness control of the ACT index finger . . . 76
4.5 Cartesian force control of the ACT index finger . . . 77
4.6 Partial controllability of index finger DIP joint in free motion . . . 79

4.7 Partial controllability of index finger DIP joint during force production 80
4.8 End-tip trajectory tracking for the ACT index finger with Cartesian stiffness control 82
4.9 End-tip trajectory tracking for the ACT thumb with Cartesian stiffness control 84
4.10 Schematic of coordinate frames and the defined object-space coordinates. 85
4.11 Two-fingered object manipulation with the ACT hand 88

5.1 Experimental ACT hand results for object stiffness control with increasing stiffness gains 100
5.2 Object stiffness control with varying internal grasp force 101
5.3 Object stiffness control with a larger object width 102
5.4 Schematic of human-like control of the ACT hand. 105
5.5 Disturbance response for static muscle-space stiffness control 106
5.6 Disturbance response for muscle-space stiffness with updating resting lengths based on object stiffness control law 107
5.7 Object manipulation results for muscle-space stiffness control law . . 108

Chapter 1

Introduction

1.1 Motivation and Goals

The human hand's impressive dexterity and manipulation capabilities arise from its complex musculoskeletal structure, biomechanical properties, and neuromuscular control in a way that is not fully understood. State-of-the-art robotic hands are capable of grasping a variety of objects, but the abilities of these hands in fine object manipulation is quite limited. Superior human dexterity is paradoxical given the serious biological limitations, including sensorimotor delays and imprecise position sensing, compared to existing robotic hands. The Anatomically Correct Testbed (ACT) hand is designed as a physical simulation platform for examining the underlying mechanisms of human hand dexterity (Deshpande et al., 2013b). The ACT fingers are designed to accurately replicate the bone shapes and musculotendon routing and structure of the human hand, and sensing and actuation in the ACT hand also replicates key features of the human hand.

The complex mechanical structure of the human hand, replicated in the ACT hand, presents unique control challenges not present in other robotic hand systems. Robotic hands are typically designed with an anthropomorphic joint structure, such that they can utilize tools and objects designed for use by human hands, but with a relatively simple transmission between actuators and joints to facilitate more straightforward control. By comparison, the human hand has a highly nonlinear transmission

between the actuators (muscles) and joints due to its variable muscle moment arms and interconnected tendon networks (Deshpande et al., 2010; Niehues and Deshpande, 2017; Niehues et al., 2017), resulting in a complex joint control problem where multiple muscles must work in a highly coordinated fashion to achieve even simple joint motions (Deshpande et al., 2013a).

In this dissertation, I utilize the ACT hand, along with other robotic systems, to explore the underlying sources of human hand dexterity. In the process, the unique advantages and control challenges presented by the human hand's complex musculoskeletal structure are uncovered and explored, along with the roles of neuromuscular control on hand dexterity and robustness. This research provides a direct comparison between robotic and human hands, which can be applied to improve the design and control of robotic/prosthetic hands and to provide crucial insights to the fields of hand biomechanics and neuromuscular control.

1.2 Comparing the Design and Control of Existing Robotic Hands and the Human Hand System

In this section, I will compare the musculoskeletal structure of the human hand with the mechanical design of existing robotic hands, then describe the fundamental differences between typical robotic control algorithms and neuromuscular control strategies observed in humans. I also explore how the ACT hand can be utilized as a research platform to better understand the underlying reasons for the significant performance gap that exists between human and robotic hands.

1.2.1 State of the Art Robotic Hand Designs

While robotic hands are commonly designed with anthropomorphic shapes to allow human-like interactions with tools and objects, they do not possess human-like mechanical properties or actuation methods. Some robotic hands employ actuators directly connected to the joints (Butterfaß et al., 2001). However, the majority of robotic hand designs implement tendon-driven actuation they allow remote actuator placement, lower apparent finger inertia, and greater robustness to impacts. One common tendon arrangement is the $N+1$ configuration where the number of tendons is one more than the number of joints, which represents the minimum number of tendons for finger controllability (Bridgwater et al., 2012; Ficuciello et al., 2011; Melchiorri et al., 2013). Antagonistic $2N$ tendon arrangements have also been implemented, allowing straightforward independent joint control and, in cases with nonlinear tendon elasticity, independent joint stiffness regulation through co-contraction (Lee et al., 1994; Grebenstein et al., 2012). In all cases, great care must be taken to minimize friction as much as possible to facilitate accurate force and position tracking (Friedl et al., 2015).

Robotic hands are also often designed with a level of intrinsic passive compliance for increased robustness, safe environmental interactions, and fine force control capabilities. Examples include the variable stiffness design of the DLR Awiwi Hand (Grebenstein et al., 2012) and compliant twisted-string actuators of the UB Hand IV (Melchiorri et al., 2013). Additionally, in systems with highly geared position-controlled actuators, such as Robonaut 2 (Bridgwater et al., 2012), or with tension sensors that operate based on load-based deflection (Palli and Pirozzi, 2011), a level of series elasticity is explicitly required to achieve fine force control.

1.2.2 Human Hand Musculoskeletal Structure

Human fingers each have four joint degrees of freedom (DOFs) articulated by six[1] muscle-tendon units. There are two extrinsic[2] flexor muscles that route along the palmar side of each finger and insert directly into the distal and medial phalanx. The extrinsic extensor muscle and three intrinsic[3] muscles join to form an interconnected extensor mechanism that slides along the finger's dorsal surface. The human thumb has five joint DOFs articulated by eight[4] muscle-tendon units.

The way muscle forces act to produce torques at the finger and thumb joints can be defined by muscle moment arms, which vary nonlinearly as a function of joint posture (An et al., 1983; Smutz et al., 1998) and of applied load, due to the inherent viscoelasticity of tendon paths (Pearlman et al., 2004). Additionally, in human fingers, muscle tensions are distributed through the branches of the extensor mechanism as a complex function of posture, muscle forces, and interaction forces/torques (Lee et al., 2008; Valero-Cuevas et al., 2007; Niehues et al., 2017), which results in a passive coupling effect at the two interphalangeal joints and produces the natural curling motion observed in human fingers (Leijnse et al., 2010).

[1]The index and little fingers also have seventh muscles in the form of extra extensor muscles, namely the extensor indicis and extensor digiti minimi, that act to increase their independence of motion from the other fingers. For single finger control, these muscles have equivalent functions as the common extensor muscles (Brand and Hollister, 1999), and thus in this work the extensor muscles in these fingers are combined into a single muscle-tendon unit.

[2]Extrinsic refers to muscles located in the forearm.

[3]Intrinsic refers to muscles located in the hand.

[4]The adductor pollicis thumb muscle is commonly considered to consist of two separate muscle heads, oblique and transverse. Because these two heads have identical insertion points and relatively similar tendon paths and functionality, the adductor pollicis is considered as a single muscle in much of this work and in the ACT thumb.

1.2.3 Robotic Control Strategies for Dexterous Manipulation

The ability to control both the positions and applied forces of a robotic hand's end-tips is crucial when performing fine manipulation tasks. Impedance control represents an ideal control strategy for interacting with the external environment in an intuitive manner (Hogan, 1985). Impedance control can implemented in various ways, such as in tendon-space, joint-space (Abdallah et al., 2010; Chalon et al., 2011), or Cartesian-space (Biagiotti et al., 2003), depending on the task requirements and goals.

Object manipulation capabilities have been experimentally demonstrated in the literature for many different robotic hand systems. General overviews of dexterous manipulation can be found in the works of Bicchi (2000), Okamura et al. (2000), and Wimböck et al. (2012). For in-hand manipulation, it is beneficial to extend the control law to act in a virtual object frame to allow simultaneous regulation of the object's 3-D position and orientation, applied external forces/torques, and internal grasp forces (Schneider and Cannon, 1992). Various object-level control strategies have been developed and experimentally tested with joint torque-controlled hands, such as the DLR Hand II (Wimböck et al., 2006, 2012).

In tendon-driven robotic hand systems, the transmission from actuator-space to joint- and endtip-space is typically intentionally designed to be relatively straightforward. Fine manipulation has been demonstrated in several fully controllable tendon-driven hands, such as the planar hand of Lee et al. (1994) and the $2N$ Shadow Hand (Shadow Robot Company, 2017). Manipulation capabilities have also been demonstrated in under-actuated hands like the iHY Hand in a limited but useful workspace (Odhner and Dollar, 2015).

1.2.4 Human Neuromuscular Control

The neuromuscular control strategies of the central nervous system (CNS) afford our hands dexterity by exploiting certain aspects of the hand's complex biomechanical structure while also mitigating the inherent biological limitations. For example, the significant sensorimotor delay that exists between the sensory organs, CNS, and muscles makes pure feedback control infeasible for dexterous tasks (Morasso, 2011). Instead, the CNS takes advantage of the natural impedance-like behavior of muscles to achieve robustness in uncertain environments and fast reactions to disturbances (Gribble et al., 1998; Burdet et al., 2001). Additionally, accurate internal models of both hand biomechanics and the external environment are utilized by the CNS for control during complex manipulation tasks (Flanagan et al., 2006; Milner et al., 2007).

1.2.5 The Anatomically Correct Testbed (ACT) Hand

The ACT hand provides us with a unique research platform for understanding how human biomechanics and neuromuscular control combine to achieve amazing dexterity. From a mechanical design standpoint, it is still an open question whether aspects of the human hand's complex musculoskeletal structure would also be advantageous if implemented in robotic hands. Because moment arms vary significantly as a function of joint posture and muscle force inputs in some cases are distributed through interconnected tendon networks, the joint control problem becomes significantly more complex than for most other robotic hands (Deshpande et al., 2013a). Additionally, the ACT hand, consistent with human anatomy, has multiple uncontrollable joint DOFs (e.g. finger distal joints), making it an under-actuated system.

Experimental analysis with the ACT hand can provide key insights into the benefits and drawbacks of human-like joint and tendon structure, which can be utilized to improve robotic and prosthetic hand design and bring them closer to human hand capabilities. While the ACT hand's human-like structure represents a challenging control problem, the results in this work demonstrate the viability of such complex tendon-driven hand designs for dexterous tasks, which will hopefully encourage researchers to pursue innovative robotic hand designs that draw inspiration from the human system.

1.3 Contributions

The major novel contributions of this dissertation are:

- A generalized modeling for complex interconnected tendon systems is developed and validated, with the specific goal of modeling the mechanical structure of the human finger. The key feature of this model is its ability to predict how muscle forces will transmit through an interconnected tendon network based on tendon kinematics and the current joint posture, so that the transformation from input muscle forces to output joint torques and fingertip forces is accurately represented. The feasibility of this model is evaluated by using a tendon-driven robotic finger testbed, and subsequently used to explore the unique features of the extensor mechanism.

- The ACT thumb is validated as a physical model of the human thumb, capable of faithfully representing human. Experimental results demonstrate that the ACT thumb is capable of replicating human thumb musculoskeletal structure and

muscle functionality, provided tendon routing is properly adjusted to account for load-dependent moment arm changes that occur naturally in human thumbs.

- An object-space stiffness control algorithm is developed for the Robonaut 2 (R2) hand with the goal of performing fine object manipulation. The combined Cartesian end-tip control and object-space manipulation control algorithms are tested experimentally on the R2 hand, with results demonstrating tracking performance and robustness while simultaneously controlling object position/orientation, external interaction forces, and grasp forces.

- An object-space control algorithm is developed for the human-like musculoskeletal structure of the ACT hand to perform fine object manipulation. Using only proprioceptive feedback in the form of muscle force and position sensing, Cartesian control of finger and thumb end-tips is achieved by utilizing models of the ACT hand's tendon and joint structure. Experimental testing of the object-space stiffness control law with limited integral action demonstrates accurate tracking of the grasped object's 3-D position and orientation. Control analysis and experimental results with the ACT hand provide significant insights into the controllability and functionality of the human hand's mechanical structure for dexterous manipulation tasks.

- Finally, inspired by the hierarchical structure of the human neuromuscular system, a novel muscle-space stiffness control strategy is developed that implements low-level stiffness in muscle-space but can also emulate a separate object-space stiffness in quasi-static conditions. First, analytical modeling techniques and experimental ACT hand testing are used to identify the limitations of object-space stiffness control gains based on the inherent compliance of the robotic

system, object size/shape, and applied grasp forces. Then, for the developed human-inspired muscle-space control strategy, experimental ACT hand manipulation tests are performed to demonstrate the ability to significantly increase quasi-static object stiffness without sacrificing grasp stability, which can significantly improve manipulation capabilities.

1.4 Dissertation Outline

This dissertation is organized as follows. In Chapter 2, analytical and physical models of the human fingers and thumb are developed that (i) accurately representing the complex transformation from input muscle forces to output joint torques and end-tip forces and (ii) confirm that the ACT hand is capable of faithfully representing human musculoskeletal structure and muscle functionality. End-tip Cartesian and object-space control algorithms are developed and experimentally tested for the anthropomorphic tendon-driven Robonaut 2 hand in Chapter 3, and then for the human-like musculoskeletal structure of the ACT hand in Chapter 4. Finally, in Chapter 5, analytical modeling and ACT hand experimentation are utilized to explore the passivity bounds on object stiffness controllers for grasp stability, then a novel muscle-space control strategy is developed that draws inspiration from the the human neuromuscular system.

Chapter 2

Mechanical Modeling of the Human Hand

In this chapter, I develop analytical and physical models of that capture the complex biomechanical structure of the human hand. First, I create mechanical models for the interconnected tendon network of the human finger extensor mechanism, and then validate the model's accuracy using a robotic finger testbed. Then, I utilize the ACT thumb as a physical simulation of the human thumb in order to study the functional effects of the thumb's unique joint and tendon structure.

2.1 Modeling the Human Finger Extensor Mechanism

The interconnected tendon structure of the human finger results in a complex relationship between the input muscle forces and the output joint torques and fingertip forces. The distribution of muscle tensions through the extensor mechanism, which is a network of interconnected tendons on the dorsal surface of human fingers (see Figure 2.1), plays a critical role during everyday finger interactions and dynamic motions. A biomechanical model that fully captures the complex interactions within this interconnected tendon system would allow for an in-depth exploration of the

Portions of this chapter have been previously published in the proceedings of the 2017 IEEE International Conference on Robotics and Automation (ICRA) (Niehues et al., 2017) and in the ASME Journal of Biomechanical Engineering (Niehues and Deshpande, 2017).

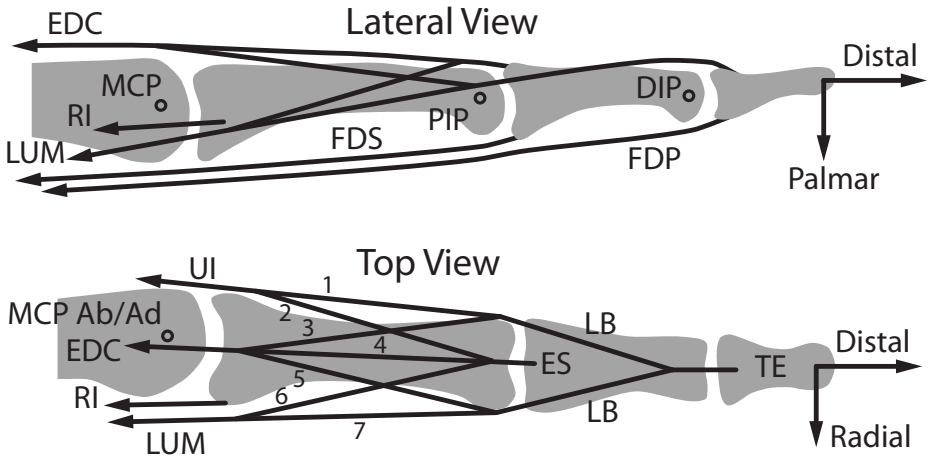

Figure 2.1: Human finger schematic. The four finger degrees of freedom, metacarpophalangeal (MCP) abduction/adduction (ab/ad), MCP flexion/extension, proximal interphalangeal (PIP), and distal interphalangeal (DIP) joints, are actuated by six muscles: extensor digitorum communis (EDC), lumbrical (LUM), ulnar interosseous (UI), radial interosseous (RI), flexor digitorum profundus (FDP), and flexor digitorum superficialis (FDS). The extensor mechanism consists of seven connecting tendons that converge to two lateral bands (LBs), the extensor slip (ES), and the terminal extensor (TE). In this model, the RI inserts directly into the proximal phalange (An et al., 1983).

unique features and functionality of the human finger.

In previous works of human finger modeling, tension distribution through the extensor mechanism has commonly been defined by constant ratios that split muscle forces between the various connecting tendons (Chao and An, 1978; Valero-Cuevas et al., 1998). A constant tension distribution may be valid in specific circumstances, i.e. static force production of a single muscle, but in reality the tension distribution ratios can vary significantly as a function of joint posture (Lee et al., 2008), relative activation levels of multiple muscles (Valero-Cuevas et al., 2007), and external forces/torques being applied to the finger.

Research efforts have also been made to develop more advanced models that

capture the kinematics of the human finger extensor mechanism and accurately predict how muscle forces distribute through the extensor mechanism in different scenarios. Kinematic models of the extensor mechanism have been developed with a strong focus on interphalangeal joint coupling (Leijnse and Kalker, 1995; Leijnse et al., 2010), but they have not been extended to model the transmission of muscle forces through the network. Other researchers have used optimization methods to determine tension distribution ratios within the extensor mechanism (Buchner et al., 1988; Brook et al., 1995). While this provides a level of insight into the effects of tension distribution variations, it cannot be considered a working mechanical model. Recently, more complete and accurate models of interconnected tendon systems, such as the custom computational modeling environment of Valero-Cuevas et al. (2007) or bond graph tendon model of King (2015), have been developed that are capable of capturing tension distribution as a function of system states, muscle inputs, and external interaction forces. These models require iterative numerical methods (i.e. a relaxation algorithm (Valero-Cuevas et al., 2007) or forward dynamic simulation (King, 2015)) to determine the equilibrium state of the extensor mechanism, which restricts their application. Our goal in this work is to create a finger model that accurately captures extensor mechanism mechanics, is computationally efficient, and is versatile for multiple applications, e.g. for dynamic simulation, forward/inverse force prediction, or real-time implementation.

In this chapter, I will develop and validate a generalized framework for modeling interconnected tendon systems. The functionality of the model is demonstrated by implementing a basic human finger model, and simulations demonstrate how dynamic variations in tension distribution are captured. Then, the model is tested and validated using a tendon-driven robotic finger testbed with human-like tendon structure.

A system identification method is introduced that utilizes observed interphalangeal joint coupling, which directly correlates to the structure and routing of the extensor mechanism, to improve model parameter estimation. Finally, I analyze the model's ability to accurately predict the force/torque transformations between the muscles, joints, and fingertip of the robotic finger.

2.1.1 Modeling of Interconnected Tendon Systems

In this section, a comprehensive framework is presented for the mechanical modeling of complex interconnected tendon networks.

2.1.1.1 Force/Torque Relationships

One of the challenges when modeling complex tendon systems lies in identifying the effective moment arm matrix R that describes how muscle forces ($\mathbf{f}_m$) are converted into joint torques ($\boldsymbol{\tau}$). In general, the effective moment arms are considered a function of joint angles ($\boldsymbol{\theta}$), such that:

$$\boldsymbol{\tau} = R(\boldsymbol{\theta})\mathbf{f}_m \tag{2.1}$$

In addition to posture-dependent changes in tendon lines of action (e.g. tendon bowstringing), joint angles also determine how muscle forces are distributed through the tendon network at any instant in time. Note that there may also exist load-dependent viscoelastic deformations, such that R is also a function of $\mathbf{f}_m$. The modeling framework presented here is capable of including load-dependent effects, but they are not included in this work.

To begin, moment arm functions are identified for each tendon segment. In a physical sense, these correspond to the perpendicular distance between a tendon's

instantaneous line of action and the joint's axis of rotation. The matrix $R_m(\boldsymbol{\theta})$ is defined as a *direct* moment arm matrix containing instances where muscles directly cross the joints; in the human index finger, this matrix would contain all metacarpophalangeal (MCP) joint moment arms and all FDP and FDS moment arms (see Figure 2.1). The connecting tendon moment arm matrix $R_{ct}(\boldsymbol{\theta})$ holds moment arm functions for all connecting tendon segments, e.g. the segments that make up the human finger extensor mechanism (segments numbered 1-7 in Figure 2.1). Thus, the total set of joint torques being applied to the system is defined as

$$\boldsymbol{\tau} = R_m(\boldsymbol{\theta})\mathbf{f}_m + R_{ct}(\boldsymbol{\theta})\mathbf{f}_{ct} \tag{2.2}$$

Methods exist in the literature for identifying the moment arms $R_m(\boldsymbol{\theta})$ and $R_{ct}(\boldsymbol{\theta})$ in human fingers (An et al., 1983; Fowler et al., 2001; Deshpande et al., 2010). The only remaining unknown term is $\mathbf{f}_{ct}$, the tension in the connecting tendons. In the next section, the tendon kinematics are analyzed to quantify how muscle forces transmit to connecting tendons depending on joint posture.

2.1.1.2 Tension Distribution

Here, a method is described for finding the tension distribution matrix $T(\boldsymbol{\theta})$ that quantifies how muscle forces transmit through junctions to the connecting tendons:

$$\mathbf{f}_{ct} = T(\boldsymbol{\theta})\mathbf{f}_m \tag{2.3}$$

The schematic in Figure 2.2 shows a single muscle splitting into multiple connecting tendons.

To begin, the relative tendon length changes that occur as a function of joint

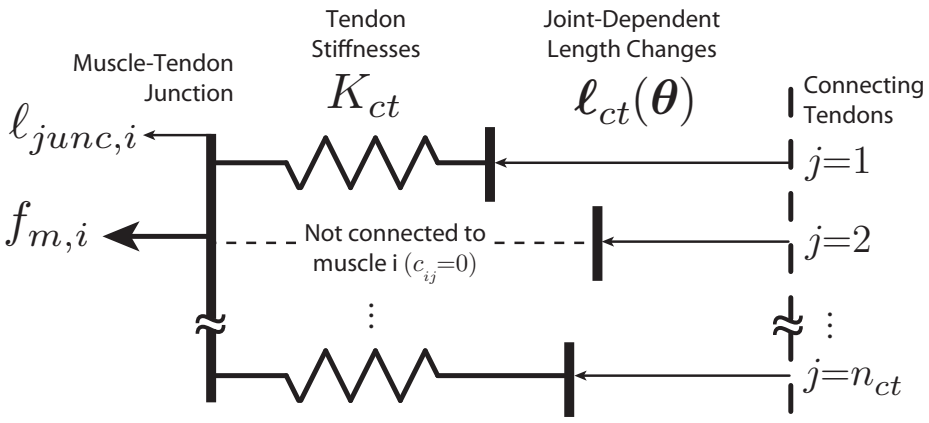

Figure 2.2: Schematic of junction between muscle i and connecting tendons.

angles are found through integration of $R_{ct}(\boldsymbol{\theta})$:

$$\boldsymbol{\ell}_{ct}(\boldsymbol{\theta}) = \int R_{ct}^{T}(\boldsymbol{\theta}) d\boldsymbol{\theta} + \boldsymbol{\ell}_{ct,init} \tag{2.4}$$

where $\boldsymbol{\ell}_{ct,init}$ describes the tendon resting lengths when all joint angles are zero.

Next, given $\boldsymbol{\ell}_{ct}(\boldsymbol{\theta})$ and the muscle force $f_{m,i}$ applied by only muscle i, the resulting tensions $\mathbf{f}_{ct,i}$ in the connecting tendons are found. Connecting tendon stiffnesses are located in the diagonal matrix K_{ct}. In order to account for the fact that zero force can be transmitted to tendons that are not attached to muscle i, a constant tendon connection matrix C is defined of the same size as $T(\boldsymbol{\theta})$, where $c_{ji} = 1$ if connecting tendon j is attached to muscle i and $c_{ji} = 0$ otherwise. Then, the effective connecting stiffness matrix $K_{ct,i}$ for muscle i can be calculated as:

$$K_{ct,i} = \text{diag}(C_i) K_{ct} \tag{2.5}$$

where C_i is the i^{th} column of C. In this way, if tendon j is not attached to muscle i (e.g. tendon $j = 2$ in Figure 2.2), element j of $K_{ct,i}$ is zero, so that no force from muscle i transfers to tendon j.

Then, the connecting tendon tensions that result from muscle force i can be found as:

$$\mathbf{f}_{ct,i} = K_{ct,i}\Big[\ell_{junc,i} - \boldsymbol{\ell}_{ct}(\boldsymbol{\theta})\Big]^{+} \tag{2.6}$$

where $\ell_{junc,i}$ is the muscle junction position (see Figure 2.2) and $[\mathbf{x}]^{+}$ is an element-wise operator such that $x_k^{+} = 0$ for $x_k \leq 0$ and $x_k^{+} = x_k$ otherwise, which is required since tendons can only apply pulling forces. From static force analysis at the junction point, total muscle force $f_{m,i}$ is equal to the sum of connecting tendon tensions $\mathbf{f}_{ct,i}$:

$$f_{m,i} = \sum_{j=1}^{n_{ct}} f_{ct,ij} = \sum_{j=1}^{n_{ct}} k_{ct,i,j}\Big[\ell_{junc,i} - \ell_{ct,j}(\boldsymbol{\theta})\Big]^{+} \tag{2.7}$$

Assuming knowledge of joint position $\boldsymbol{\theta}$ and applied muscle force $f_{m,i}$, Equation (2.7) can be solved for the junction position $\ell_{junc,i}$. Then, Equation (2.6) is used to calculate the connecting tendon forces $\mathbf{f}_{ct,i}$ that result from applied force f_{mi}, which is expressed as the function $\mathbf{f}_{ct,i}(\boldsymbol{\theta}, f_{m,i})$. Then, from Equation (2.3), the i^{th} column of T is:

$$T_i(\boldsymbol{\theta}, f_{m,i}) = \frac{1}{f_{m,i}} \cdot \mathbf{f}_{ct,i}(\boldsymbol{\theta}, f_{m,i}) \tag{2.8}$$

An exception occurs when C_i is a zero vector; in this case, muscle i has no connections and T_i is simply a zero vector.

With Equation (2.8), the way applied muscle forces will distribute through the connecting tendons as a function of $\boldsymbol{\theta}$ and $\mathbf{f}_m$ can be determined. In order to produce a linear force-torque relationship as in Equation (2.1), Equation (2.8) can be approximated for a constant operating muscle force f_{m0}, such that

$$T_i(\boldsymbol{\theta}) \approxeq \frac{1}{f_{m0}} \cdot \mathbf{f}_{ct,i}(\boldsymbol{\theta}, f_{m0}) \tag{2.9}$$

The effects of such an approximation will be explored in the next section.

Now, knowing $T(\boldsymbol{\theta})$ and combining Equations (2.1), (2.2), and (2.3), the effective moment arm matrix can be identified as:

$$R(\boldsymbol{\theta}) = R_m(\boldsymbol{\theta}) + R_{ct}(\boldsymbol{\theta})T(\boldsymbol{\theta}) \tag{2.10}$$

With this, the joint torques $\boldsymbol{\tau}$ that will be produced for any joint configuration $\boldsymbol{\theta}$ and combination of muscle forces $\mathbf{f}_m$ can be found using Equation (2.1).

The change in muscle lengths $\boldsymbol{\ell}_m(\boldsymbol{\theta})$, without considering the effects of tendon compliance, can be found as:

$$\boldsymbol{\ell}_m(\boldsymbol{\theta}) = \int R^T(\boldsymbol{\theta}) d\boldsymbol{\theta} \tag{2.11}$$

2.1.2 Case Study: Human Finger Simulation Model

In this section, the presented framework is implemented to model the human finger (Figure 2.1), with a particular focus on effective muscle moment arm variations due to changing tension distribution through the extensor mechanism. The finger is considered to be a planar system for simplicity, and the order of muscles and connecting tendons is defined as in Figure 2.1. The moment arm functions $R_m(\boldsymbol{\theta}) \in \mathbb{R}^{3\times 6}$ and $R_{ct}(\boldsymbol{\theta}) \in \mathbb{R}^{3\times 7}$ can be found in Table 2.1, and are equivalent to those proposed by Leijnse and Kalker (1995). The connection matrix $C \in \mathbb{R}^{7\times 6}$ is populated with ones at elements c_{13}, c_{23}, c_{31}, c_{41}, c_{51}, c_{62}, and c_{72}, and zeros elsewhere. The matrix $K_{ct} = \text{diag}\left([43, 75, 40, 126, 40, 75, 43]\right)\ \frac{N}{mm}$ is defined based on human data from the work of Garcia-Elias et al. (1991b), a nominal operating force is chosen for all muscles to be $f_{m0} = 10\ N$, and it's assumed all connecting tendons are taut when joint angles are zero ($\boldsymbol{\ell}_{ct,init} = \mathbf{0}$).

Table 2.1: Tendon moment arms for human finger model.

Simple Moment Arms (R_m)

	EDC	LUM	UI	RI	FDP	FDS
MCP Ab/Ad	1	-5	6	-6	1	1
MCP Flex	-9	9	6	6	11	13
PIP	—	—	—	—	10.5	8.5
DIP	—	—	—	—	6	—

Connecting Tendon Moment Arms (R_{ct})

	1	2	3	4	5	6	7
MCP Ab/Ad	—	—	—	—	—	—	—
MCP Flex	—	—	—	—	—	—	—
PIP	r_{LB}*	-5	r_{LB}*	-5	r_{LB}*	-5	r_{LB}*
DIP	-4	—	-4	—	-4	—	-4

Note: Moment arms taken from the work of Leijnse and Kalker (1995).

* $r_{LB} = -5\left[1 - \frac{2\theta_3}{\pi/2} + \frac{\theta_3^2}{(\pi/2)^2}\right]$, where θ_3 is PIP angle in radians.

2.1.2.1 Posture-Dependent Effective Moment Arms

The effective muscle moment arms of the muscles connected to the extensor mechanism (Figure 2.3) show a sharp switching behavior as various connecting tendons become taut or slack. The curve along which a sharp moment arm change occurs represents the IP coupling curve (Figure 2.3b). The effective PIP and DIP moment arms on each side of the coupling curve tend to stabilize the system toward the curve, producing the coordinated IP joint motions observed in human fingers (Leijnse et al., 1992). The location and shape of the IP coupling curve depends on model parameters. Changes to connecting tendon rest lengths ($\boldsymbol{\ell}_{ct,init}$) act to translate the IP coupling curve up or down. Its slope and curvature are determined by the moment arm functions of the LB, ES, and TE tendons in $R_{ct}(\boldsymbol{\theta})$.

How sharply the effective moment arms switch depends upon the connecting

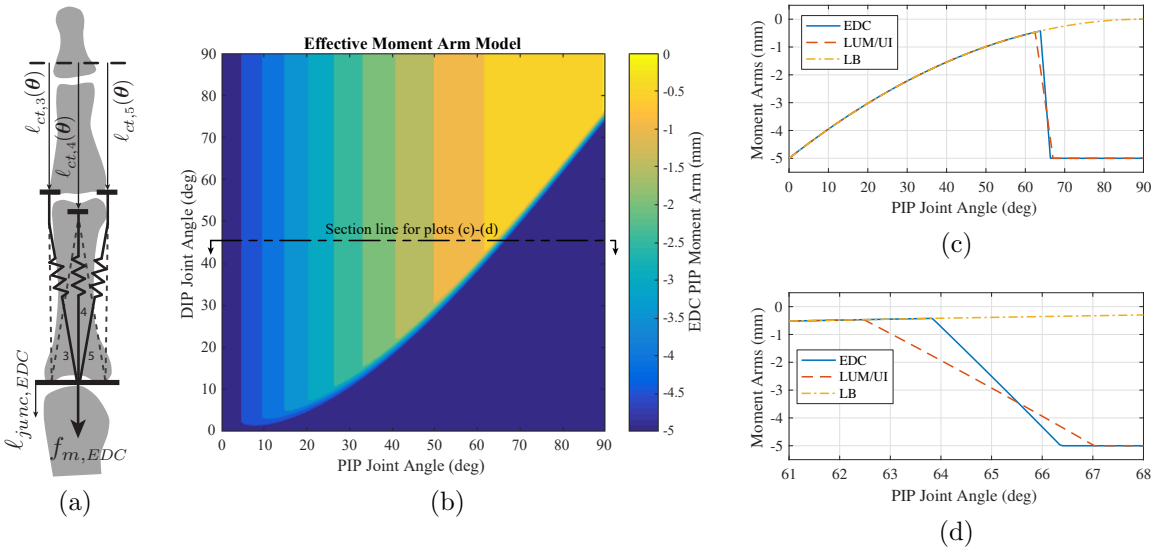

Figure 2.3: Posture-dependent effective moment arms of extensor mechanism muscles. (a) Tendon schematic for the EDC muscle. The dashed lines in place of tendons 1, 2, 6, and 7 signify they do not attach to the EDC, i.e. $c_{j1} = 0$. The lengths of connecting tendons that do attach to the EDC can be found using Equation (2.4). (b) Contour plot of the effective EDC moment arm across the PIP, as a function of PIP and DIP joint angle. In the top left section above the IP coupling curve, $\ell_{ct,3} \ll \ell_{ct,4}$, so all EDC force transmits through the LBs to the TE; in the bottom right section, $\ell_{ct,3} \gg \ell_{ct,4}$, so force transmits to the ES. (c) Section view of EDC, LUM, and UI moment arm functions for constant DIP angle $\theta_{DIP} = 45^o$. The EDC, LUM, and UI moment arms are equal to $r_{LB}(\boldsymbol{\theta})$ when LBs are taut (where r_{LB} is defined in Table 2.1), then sharply shift down to $r_{ES} = -5$ mm as the tension shifts to the ES. (d) Enlarged view near the switching point.

tendon stiffnesses K_{ct} and the chosen operating force f_{m0}. The LUM and UI show less sharp moment arm changes than the EDC because of their relatively less stiff connecting tendons (Figure 2.3d). A higher value of chosen operating muscle force f_{m0} also results in a less sharp change; conversely, as $f_{m0} \to 0$, moment arm switching becomes instantaneous. The approximation in Equation (2.9) has the effect of setting a constant slope of moment arm switching, as opposed to a slope that varies dynamically as a function of muscle input force. In this work, the switching slope does

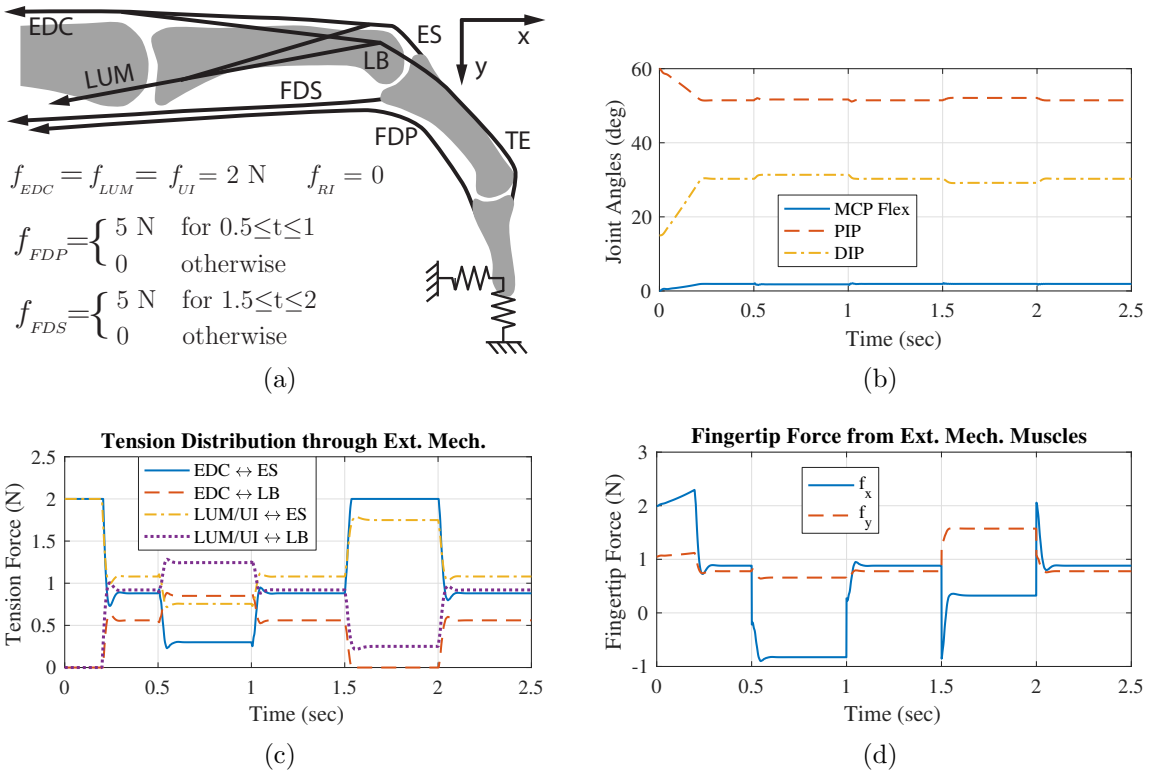

Figure 2.4: Simulation of a human finger model. Because dynamic response is not critical for our analysis, finger inertia and damping are chosen heuristically to produce a fast, damped response. (a) Simulation conditions and input muscle forces. Fingertip translational position is stiffly constrained, while fingertip angle is allowed to rotate freely, replicating a hard point contact with no slipping. (b) Simulated joint angles. Tensions in the muscles of the extensor mechanism act to stabilize the finger in a coupled pose. (c) Force distribution to connecting tendons ($\mathbf{f}_{ct}$), which change in response to disturbance forces such as the activation of the FDP or FDS. (d) Fingertip force contribution from only the extensor mechanism muscles (EDC, LUM, and UI). Changes in tension distribution alter the resultant fingertip force produced by these muscles, despite constant input muscle tensions and minimal changes in joint angle.

not play a significant role, so the approximation is desirable for a linear force-torque relationship as in Equation (2.1).

2.1.2.2 Changing Tension Distribution

To demonstrate how muscle tensions dynamically distribute through the extensor mechanism, a simulation study of a finger is performed with a fingertip constraint that replicates a hard point contact (Figure 2.4). Activation of any extensor mechanism muscles (i.e. EDC, LUM, or UI) tends to stabilize the PIP and DIP angles toward the IP coupling curve. Then, when a disturbance is introduced, in this case through activation of the FDP or FDS, small joint angle changes dynamically alter the tension distribution to connecting tendons (Figure 2.4c) until the system re-stabilizes to a new equilibrium state. These tension distribution variations change the effective moment arms of extensor mechanism muscles, and thus also change their contribution to force production at the fingertip (Figure 2.4d).

2.1.3 Experimental Validation of Tendon Modeling Framework

The proposed tendon model is tested and validated using a robotic finger with customizable tendon routing (Figure 2.5). In this section, the methods used to identifying model parameters for the robotic finger testbed with human-like tendon structure are described. Then, the capabilities of the interconnected tendon model are demonstrated for capturing complex muscle-to-fingertip force transformations.

2.1.3.1 Experimental Setup

In this work, the tendon routing and interconnections of the robotic finger were designed to mimic human finger structure. The tendons implemented correspond to the two flexors (FDP and FDS), extensor (EDC), and LUM muscles. In order to provide insights that are significant for our complex tendon model, focus is not directed toward lateral fingertip forces that depend only upon MCP ab/ad moment

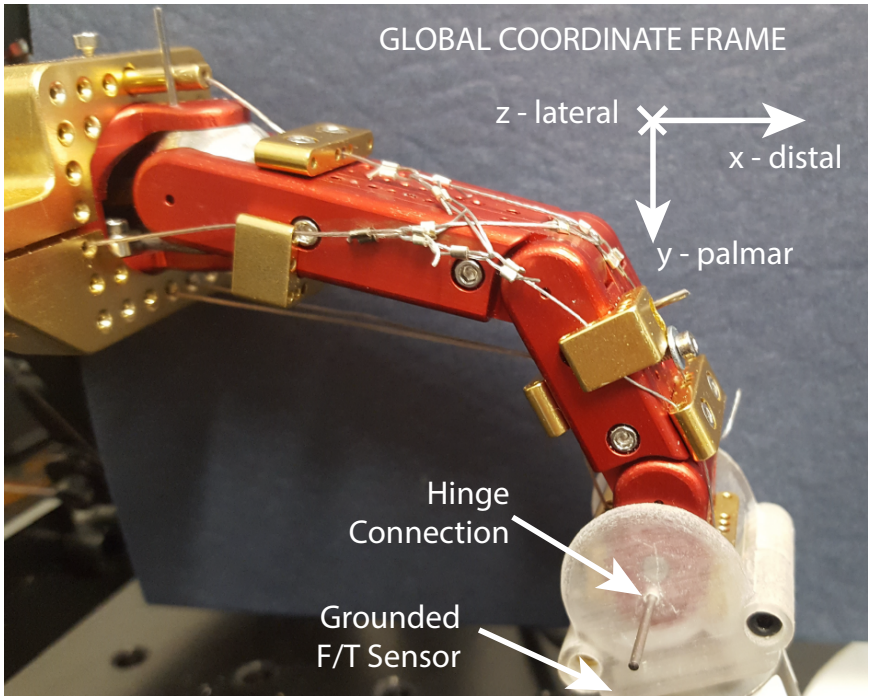

Figure 2.5: Robotic finger testbed with customizable tendon routing, originally designed and manufactured by Si Tech Engineering (Snoqualmie, WA). Tendons are connected to force-controllable moving coil linear actuators (LCA50-050-75-2, SMAC Corporation, Carlsbad, CA) with in-line tension load cells (MLP-10, Transducer Techniques, LLC, Temecula, CA). Finger joints contain embedded angle sensors (AS5048 Magnetic Rotary Encoder, ams AG, Premstaetten, Austria). For fingertip force analysis, a grounded six-axis force/torque transducer (F/T Nano17 SI-50-0.5, ATI Industrial Automation, Garner, NC) is connected to the fingertip using an adapter that constrains fingertip position but allows free rotation of the distal link.

arms. The interosseous muscles are not included because the UI has a virtually identical function as the LUM in the lateral x-y plane and the RI acts only on the MCP joint. For fingertip force analysis, fingertip position is constrained but the distal link is allowed to freely rotate, simulating a hard point contact at the fingertip.

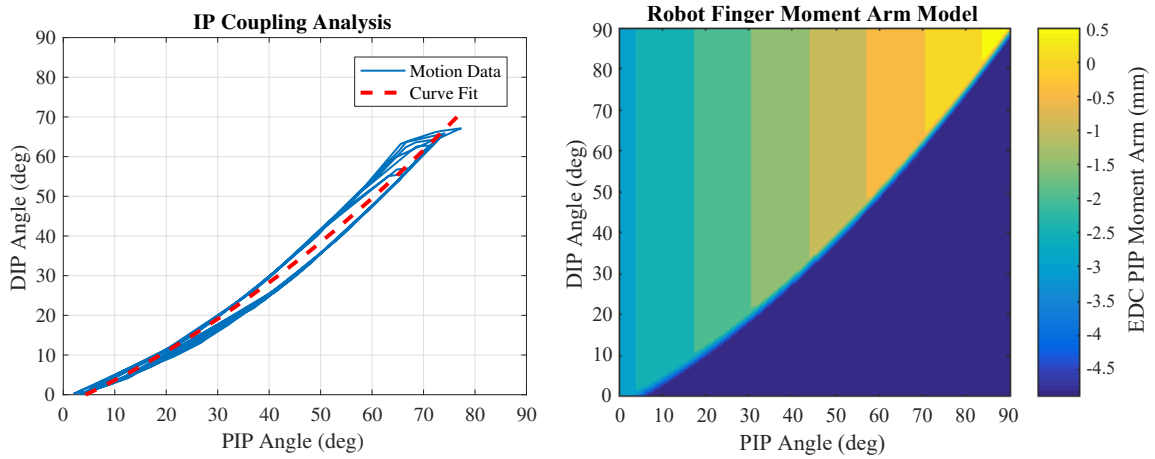

Figure 2.6: Model parameter identification to correctly replicate observed IP coupling. (a) With the extensor mechanism muscles (EDC and LUM) taut, FDP contraction/extension results in PIP/DIP joint motions along the coupling curve. (b) To replicate the observed IP coupling in the model, a constraint is enforced that the LB and ES are both taut along this curve, or $\ell_{LB}(\boldsymbol{\theta}) = \ell_{ES}(\boldsymbol{\theta})$. The DIP moment arm of the TE and PIP moment arm of the ES are assumed to be constant, while the PIP moment arm of the LB is modeled as a first-order function of PIP angle.

2.1.3.2 Model Parameter Identification

To identify tendon moment arms, extensive tendon kinematic data is collected by measuring tendon excursions as the joints are moved through their range of motion. Then, moment arms can be determined by finding the gradient of a forward kinematic mapping (An et al., 1983; Deshpande et al., 2010). The direct moment arm functions $R_m(\boldsymbol{\theta})$ were estimated by fitting a second-order forward kinematics function, i.e. $\hat{\boldsymbol{\ell}}_m(\boldsymbol{\theta}) = \frac{1}{2}A\left(\boldsymbol{\theta}^2\right) + B\boldsymbol{\theta} + \mathbf{c}$, using a least-square regression (LSR) of tendon kinematic data. Through differentiation $r_{ij}(\boldsymbol{\theta}) = \frac{\partial \hat{\ell}_{m,j}}{\partial \theta_i} = a_{ji}\theta_i + b_{ji}$, first-order moment arm functions are found to populate $R_m(\boldsymbol{\theta})$, which are considered sufficient to capture the angle-dependent moment arm variations in our system. Where muscles do not

directly cross the joints, the corresponding elements of R_m are set to zero.

Next, in order to identify the moment arm parameters R_{ct} and resting lengths $\boldsymbol{\ell}_{ct,init}$ of connecting tendons, tendon kinematic data is combined with additional motion data to identify finger joint coupling. A nonlinear optimization problem is formulated to minimize error between the predicted excursions $\boldsymbol{\ell}_m(\boldsymbol{\theta})$ from Equation (2.11) and tendon excursion measurements while simultaneously enforcing the constraint to reproduce observed IP coupling (see Figure 2.6 for details). Including IP coupling data in the parameter identification process reduces the parameter solution space, leading to more robust and accurate parameter estimation. The optimized model results in a muscle excursion RMS error of 1.54 mm for a kinematic data set of 700 points.

2.1.3.3 Forward Problem: Fingertip Force Prediction

Here, the accuracy of prediction of the fingertip force vector that will be produced by a given combination of applied muscle forces is examined. Joint angle measurements $\boldsymbol{\theta}$ are used to calculate the Jacobian matrix that transforms fingertip forces $\mathbf{f}_x = [f_x, f_y, f_z, \tau_{dist}]^T$, where τ_{dist} is an external torque applied to the distal phalange, into joint torques:

$$\boldsymbol{\tau} = J^T(\boldsymbol{\theta})\mathbf{f}_x \tag{2.12}$$

As long as the finger is not in a singularity position, the Jacobian is a full-rank matrix, meaning the inverse relation $\mathbf{f}_x = J^{-T}(\boldsymbol{\theta})\boldsymbol{\tau}$ can also be calculated.

Because the joint-dependent effective moment arm functions change abruptly near the IP coupling curve, it is infeasible to use joint angle measurements to directly determine $R(\boldsymbol{\theta})$. In our setup or during any hard point contact, the distal link

of the finger can freely rotate about that contact point, such that $\tau_{dist} \approx 0$. One possible method is to input measured muscle forces into a forward simulation to find where the system stabilizes, which would provide the tension distribution and effective moment arms $R(\boldsymbol{\theta})$ as functions of time. However, the system ordinary differential equations (ODEs) become very stiff near the IP coupling curve, which causes numerical ODE solutions to become computationally inefficient and unreliable. An alternative method that is used here is to directly identify the tension distribution ratios using an optimization that minimizes $|\tau_{dist}|$ for a given set of muscle forces.

Experimental results in Figure 2.7 demonstrate the model's forward prediction capabilities for chosen combinations of muscle forces. It was verified that the optimization method produces identical results when compared to forward simulation after settling of transient effects, but optimization is computationally much more efficient. The tendon structure is designed with similar tendon stiffnesses and tension switching curves for the EDC and LUM, such that the tension distribution ratios are approximately equivalent in all postures. Thus, it's assumed one parameter $\alpha \in [0, 1]$ is required, where α of the EDC and LUM tensions transmit to the ES and the other $(1 - \alpha)$ transmit to the TE.

The interconnected tendon model provides a relatively accurate prediction of fingertip force (Figure 2.7b, top). It was suspected that the errors were caused by unmodeled frictional effects at tendon routing points. Thus, in a separate test, the EDC and LUM were held taut at 5 N, then the finger was slightly disturbed in multiple directions and allowed return to its original pose. A fingertip force hysteresis of up to ± 0.5 N was observed, oriented primarily in the x-direction. This corresponds well to the observed prediction errors, supporting the claim that friction is the cause

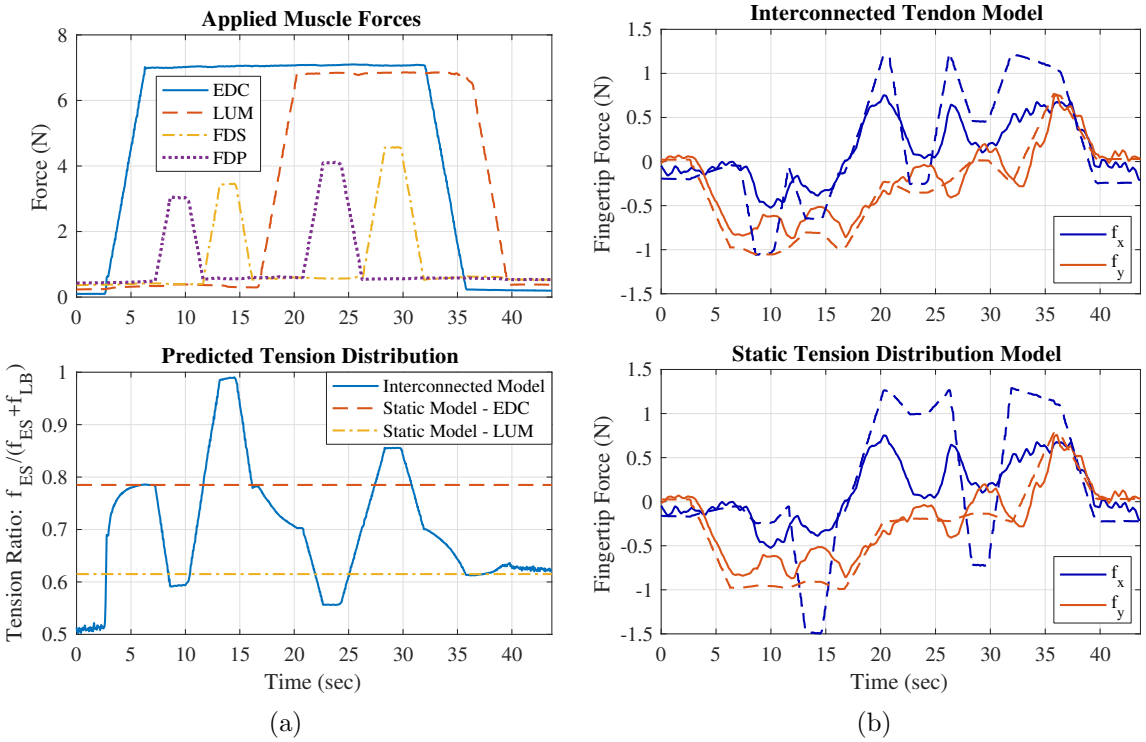

Figure 2.7: Experimental results for forward model predictions. (a) Chosen muscle force pattern (top) and predicted tension distribution ratio (bottom) represented as the fraction of EDC and LUM forces that transmit to the ES tendon. Values for the static tension distribution model, chosen to reproduce single-muscle force production of the EDC and LUM, are included for comparison. (b) Resultant fingertip forces in the lateral plane. Actual values are from the fingertip F/T sensor. The top plot shows fingertip force predictions based on the interconnected tendon model with muscle forces as input (RMSE = 0.29 N), while the bottom plot shows predictions based on a static tension distribution model (RMSE = 0.43 N). The static model also results in a significant fingertip torque, such that a forward simulation of fingertip point contact would predict unrealistic DIP hyper-extension or hyper-flexion.

of model prediction errors.

Without the ability to capture changes in tension distribution through the extensor mechanism, a static model fails to accurately predict the fingertip forces produced when multiple muscles are activated. To demonstrate this, results are also

presented using a model with static tension distribution ratios (Figure 2.7b, bottom). Distribution values were chosen such that when the EDC or LUM are activated individually (e.g. at $t \approx 6$ and $t \approx 36$ seconds), fingertip force prediction matches measured results; however, as multiple muscles become active, forward prediction using the static model cannot replicate experimental data.

2.1.3.4 Inverse Problem: Muscle Force Prediction

The inverse problem predicts muscle forces given externally applied forces/torques. This represents an under-determined problem, so optimization is helpful to choose an appropriate solution depending on a chosen cost function. The optimization problem is generalized as follows:

$$\begin{aligned} \underset{\hat{\mathbf{f}}_m, \boldsymbol{\alpha}}{\text{minimize}} \quad & \sum_{i=1}^{n_m} \left[\hat{f}_{mi} - f_{mi,est} \right]^2 \\ \text{subject to} \quad & \mathbf{f}_x = J^{-T}(\boldsymbol{\theta}) R(\boldsymbol{\theta}, \boldsymbol{\alpha}) \hat{\mathbf{f}}_m \\ & \hat{f}_{mi} \geq 0 \ , \ \alpha_j \in [0, 1] \end{aligned} \tag{2.13}$$

where $\hat{\mathbf{f}}_m$ are predicted muscle forces and $\boldsymbol{\alpha}$ contains the necessary tension distribution ratios to populate the T matrix (i.e. T is a function of $\boldsymbol{\alpha}$ instead of $\boldsymbol{\theta}$). By defining $\boldsymbol{\alpha}$ explicitly, it is not necessary to include $\boldsymbol{\theta}$ as an optimization variable, which could lead to unexpected results due to the angle-dependent nature of J, R_m, and R_{ct}. As in the previous case, only one α parameter is required corresponding to both EDC and LUM tension distribution. Because the UI or RI muscles are not included in our setup, the row corresponding to lateral force f_z is omitted from the equality constraint.

Muscle force predictions with the interconnected model are significantly more accurate than a static distribution model (Figure 2.8), even though we provided

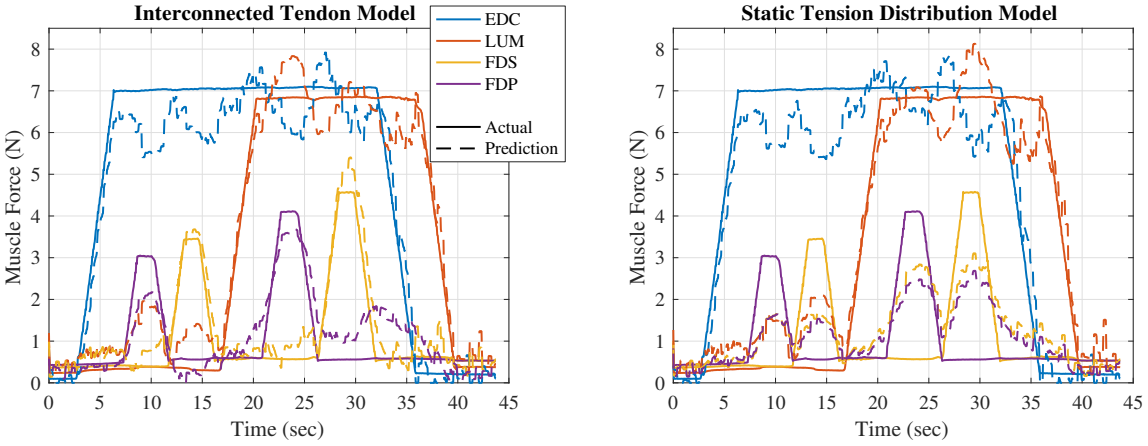

(a) (b)

Figure 2.8: Inverse prediction of muscle forces based on measured fingertip forces. (a) Muscle force prediction using interconnected tendon model (RMSE = 0.61 N). (b) Prediction using static tension distribution model (RMSE = 0.91 N). In both cases, actual muscle force values are utilized in the optimization algorithm in Equation (2.13) as muscle force estimates $\mathbf{f}_{m,est}$.

precise muscle force estimates $\mathbf{f}_{m,est}$ from tendon load cells in both cases. Both models are constrained to produce zero fingertip torque τ_{dist}, corresponding to a hard point contact. In the static model, this constraint forces the FDP and FDS activations to remain somewhat coordinated, such that their fingertip torque contributions offset. In the interconnected model, the FDP and FDS muscles can be independently activated while maintaining zero net fingertip torque because the extensor mechanism naturally offsets the resulting τ_{dist} to hold the finger's coupled pose.

2.1.3.5 Cartesian Force Control using Complex Tendon Model

Next, we demonstrate the feasibility of implementing the model for active control of Cartesian fingertip force using the tendon actuators. The controller performs the optimization in Equation (2.13) with $\mathbf{f}_{m,est} = 0$ to find the least-norm solution of

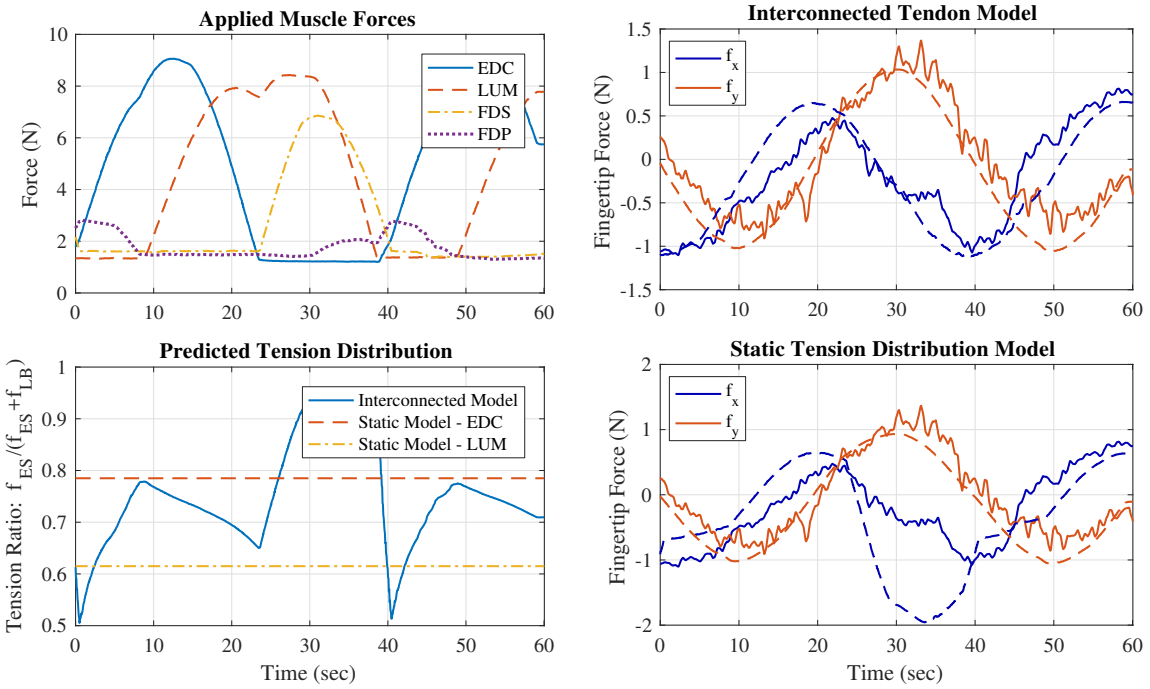

Figure 2.9: Experimental results for Cartesian fingertip force control for a circular commanded force trajectory in the x-y plane of radius 1 N. (a) Measured muscle tensions and tension distribution ratios for each model. (b) Measured fingertip force and predictions for the interconnected model (top, RMSE = 0.27 N) and the static tension distribution model for comparison (bottom, RMSE = 0.57 N). Predicted forces are calculated using muscle force measurements from tendon load cells, and differ slightly from original controller force commands due to actuator nonlinearities, creating slight deformations from the desired unit circle.

muscle forces. We commanded a circular fingertip force profile in the lateral plane, with zero fingertip torque and no constraint on lateral force production (see Figure 2.9).

2.1.4 Discussion

A modeling framework for complex interconnected tendon systems was presented, and its capabilities are demonstrated using a tendon-driven robotic finger testbed. Fingertip force prediction was shown to be more accurate than a standard static tension distribution model, demonstrating the benefit of accurately replicating muscle force transmission through the extensor mechanism. I also illustrated the model's ability to solve the inverse problem, in which muscle forces are estimated based on observed external forces/torques and, if available, rough muscle force estimates (e.g. EMG measurements). The versatility of the model is further demonstrated by implementing it directly in a fingertip Cartesian force control algorithm. The presented results are limited to a simplified human-like tendon structure and rigid routing points, but this work represents an improvement toward an anatomically accurate human finger model and a better understanding of the human hand's unique functionality.

2.2 Variable Moment Arms and Thumb-Tip Force Production of the Human-Like ACT Thumb

The human thumb plays a key role in hand functionality, inspiring researchers to use several unique methodologies to uncover the thumb's underlying biomechanical and neuromuscular properties. Cadaveric studies have proven effective for determining the thumb's musculoskeletal structure and biomechanical properties (Smutz et al., 1998; Pearlman et al., 2004), while in vivo experimentation (Johanson et al., 2001; Nataraj et al., 2015; Li and Harkness, 2004) allows for observation of the coordinated muscle activation patterns that produce appropriate thumb motions and forces during

everyday tasks. Biomechanical thumb modeling (Giurintano et al., 1995; Holzbaur et al., 2005) is a valuable tool for interpreting the collected human data and providing a comprehensive understanding of how biomechanical structure and neuromuscular control each contribute to provide thumb functionality.

Designing a robotic thumb that captures the critical properties of the human thumb is a challenging task. Thus far researchers have been unable develop a biomechanical thumb model that accurately reproduces human data (Valero-Cuevas et al., 2003; Wohlman and Murray, 2013), most likely due to the thumb's mechanical complexity, high anatomic variability (Santos and Valero-Cuevas, 2006), and the inherent challenges of conducting in vivo and cadaveric experiments. Without the existence of a well-defined thumb model, a definitive claim cannot be made that the ACT thumb represents a valid human thumb model. Here, I will present an iterative design process for the ACT thumb in order to reproduce multiple sources of human thumb data from literature as closely as possible. Thus far, only preliminary testing has been performed on the ACT thumb (Chang and Matsuoka, 2006; Deshpande et al., 2013b).

In this chapter, I analyze the muscle moment arms and thumb-tip force vectors in the ACT thumb in order to compare the ACT thumb's mechanical structure to the human thumb. The nominal ACT thumb tendon structure was designed to closely match cadaveric moment arm data reported by Smutz et al. (1998). Motion data was used to determine the joint-dependent ACT muscle moment arms. The ACT thumb's human-like muscle functionality was then analyzed by collecting 3-D thumb-tip force vectors produced when forces were applied to the ACT muscle/tendon units. An adjusted ACT thumb was designed with slightly altered tendon routing to improve

the matching of ACT thumb-tip forces to human data reported by Pearlman et al. (2004). Results are presented for both ACT models, along a sensitivity analysis to show how changes in tendon moment arms affect thumb-tip forces. Discussion is provided for choosing the ideal ACT model to best replicate the human thumb's mechanics depending on the desired task parameters, such as the expected magnitude of tendon forces.

2.2.1 Methods

The ACT thumb is designed with the five non-orthogonal, non-intersecting anatomical degrees of freedom (DOFs) (Giurintano et al., 1995; Hollister et al., 1992, 1995) and eight musculotendon actuator units[1] (see Figure 2.10). Details for the ACT thumb can be found in the work of Deshpande et al. (2013b), and a full model of the ACT thumb's joint kinematics can be found in Appendix A.2. While the internal joint structure is comprised of an aluminum beam structure, the bone shells, including tendon routing points, are manufactured using an SLA 3-D printer (Form 1+, FormLabs Inc.). Thus, the physical moment arms of the system can be adjusted by modifying the CAD models and subsequent re-printing of the bone shells.

2.2.1.1 Muscle Moment Arms

To begin, the moment arms of the ACT thumb are compared with cadaveric thumb moment arm data reported by Smutz et al. (1998). In their work, Smutz

[1]Note that the ACT hand implements the ADP as a single muscle, whereas in human thumbs the ADP is commonly described as having two separate heads. This decision was made to simplify the design of the ACT hand, due to the similar insertions, tendon paths, and functionality of the two ADP muscle heads. In this work, all human data comparisons for the ADP are for the oblique head, which more closely matches ACT ADP routing.

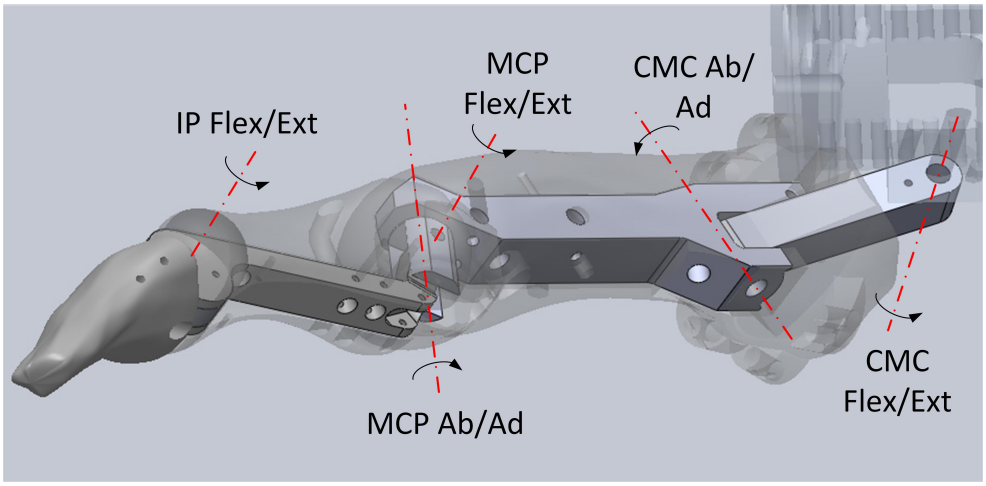

(a)

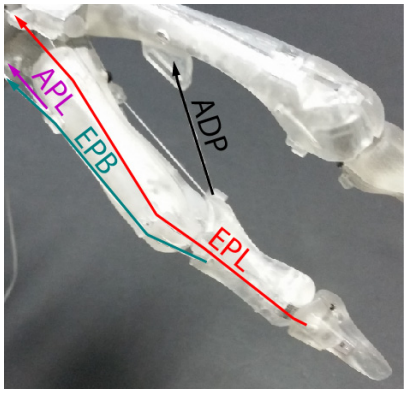

(b)

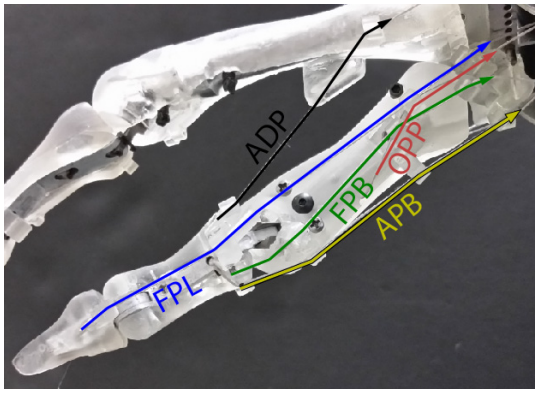

(c)

Figure 2.10: Musculoskeletal structure of the ACT thumb. (a) The joint axes for the ACT thumb's five anatomical DOFs, including flexion/extension and abduction/adduction of the carpometacarpal (CMC) joint, flexion/extension and abduction/adduction of the metacarpophalangeal (MCP) joint, and flexion/extension of the interphalangeal (IP) joint. (b) Dorsal view of the ACT thumb, showing the adductor pollicis longus (ADP), extensor pollicis longus (EPL), abductor pollicis longus (APL), extensor pollicis brevis (EPB) tendons. (c) Palmar view showing the flexor pollicis longus (FPL), flexor pollicis brevis (FPB), opponens (OPP), and abductor pollicis brevis (APB) tendons.

et al. (1998) define the CMC flexion/extension and abduction/adduction joint axes as orthogonal to the plane of the palm, which differs significantly the anatomical CMC joint axes (Hollister et al., 1992) that are present in the ACT thumb (Chang and Matsuoka, 2006). Therefore, ACT CMC joint angles are defined with respect to two virtual CMC joint axes defined orthogonal to the palm for all subsequent moment arm analyses.

Motion data was individually recorded for each joint using a motion capture system with active infrared LED markers (PhaseSpace Inc.) while holding all other joints stationary. The motion capture system has been shown to be sufficiently accurate for finger pose estimation (Yun et al., 2015). Additional validation tests were performed to verify motion capture accuracy by placing multiple markers on a single bone segment and moving the thumb through its range of motion. The resulting marker distance estimations, which should remain constant, had a standard deviation of ± 0.8 mm and a maximum variation of 2 mm that occurred near joint limits where markers become more obscured. The maximum variation would result in a joint angle estimation error of $\pm 4^o$, which I deem to be acceptable for this study. Muscle excursion data was simultaneously recorded from encoders in the musculotendon actuator units with the tendons held taut by constant torsion springs.

Three-layer feed-forward neural networks (McCulloch and Pitts, 1943) were trained for each joint using the MATLAB Neural Network Toolbox (Mathworks Inc.) with joint angle (θ) as input and muscle lengths ($\boldsymbol{\ell} \in \mathbb{R}^8$) as output to find forward kinematics functions $\boldsymbol{\ell} = \mathbf{f}_i(\theta_i)$ for each joint $i = 1, \ldots, 5$. Posture-dependent moment arm functions $\mathbf{R}_i(\theta_i)$ are found through differentiation:

$$\mathbf{R}_i(\theta_i) = \frac{\partial \boldsymbol{\ell}}{\partial \theta_i} = \frac{\partial \mathbf{f}_i(\theta_i)}{\partial \theta_i} \tag{2.14}$$

In previous work with the ACT hand, the forward muscle kinematics have been fitted using either Gaussian process regression (GPR) or LSR with a third-order polynomial function with fully populated coefficients (Deshpande et al., 2008, 2009, 2010). In this work, I avoid using GPR due to its high computational cost, which tends to severely limit control loop rates and will become infeasible when attempting to control multiple fingers simultaneously. I have chosen neural networks because they have lower computational cost compared to GPR and do not require a user-defined parametric equation as do LSR and many other smooth optimization techniques. The number of hidden nodes for each network was chosen heuristically between 3 and 5 to match kinematic data without over-fitting.

2.2.1.2 Thumb-Tip Forces

Next, I collected ACT thumb-tip force data for comparison with cadaveric data (Pearlman et al., 2004). A multi-axis force/torque sensor (ATI Nano25) was connected to the ACT thumb-tip while the thumb was statically positioned in either key or opposition pinch posture, and muscle forces are manually applied while recording tendon tensions (Omega DFG55). Thumb-tip force vectors are recorded while holding muscle tensions equal to the maximum muscle forces applied by (Pearlman et al., 2004).

Results will be presented from two distinct tendon routing designs. In the first case, the tendon origins, routing points, and insertions were specifically designed to match muscle MAs from cadaveric data (Smutz et al., 1998). However, as other researchers have also observed (Wohlman and Murray, 2013), a thumb model that matches reported MAs does not necessarily lead to matching of thumb-tip forces. Therefore, I also present results from a second ACT tendon routing design with

slight modifications, informed by a simulation model, to better match reported human thumb-tip forces.

Finally, the sensitivity of MA variations toward thumb-tip force matching was analyzed using a computer simulation thumb model. A nominal model based on human MA data leads to poor thumb-tip force matching, as already stated. Therefore, MAs and joint angles were optimized to generate a thumb model which accurately recreates thumb-tip force production of each muscle (see Table 2.3 for details of optimization). The range of allowable variation were then found for each MA while holding all others constant, with the requirement that corresponding thumb-tip force must remain within reported human ranges (Pearlman et al., 2004).

2.2.2 Results

2.2.2.1 Muscle Moment Arms

Using forward kinematic networks trained for each joint and Equation (2.14), angle-dependent moment arm plots were generated for all five thumb joints (Figure 2.11) and compared with cadaveric data reported by Smutz et al. (1998). The neural network models were validated for separately collected test motion data, which showed a mean absolute error of less than 0.02 mm in all cases. The neural network moment arm curves were also cross-validated with those generated using GPR with the same motion data in order to ensure the results are independent of the fitting method used. The MA plots are very similar for each case, with an average absolute error of 0.56 ± 0.51 mm for all muscle-joint combinations.

The nominal ACT model, designed to match human thumb moment arms, falls within experimental ranges in nearly all cases. Limitations preventing exact MA matching will be explored in more detail in the Discussion section. The adjusted

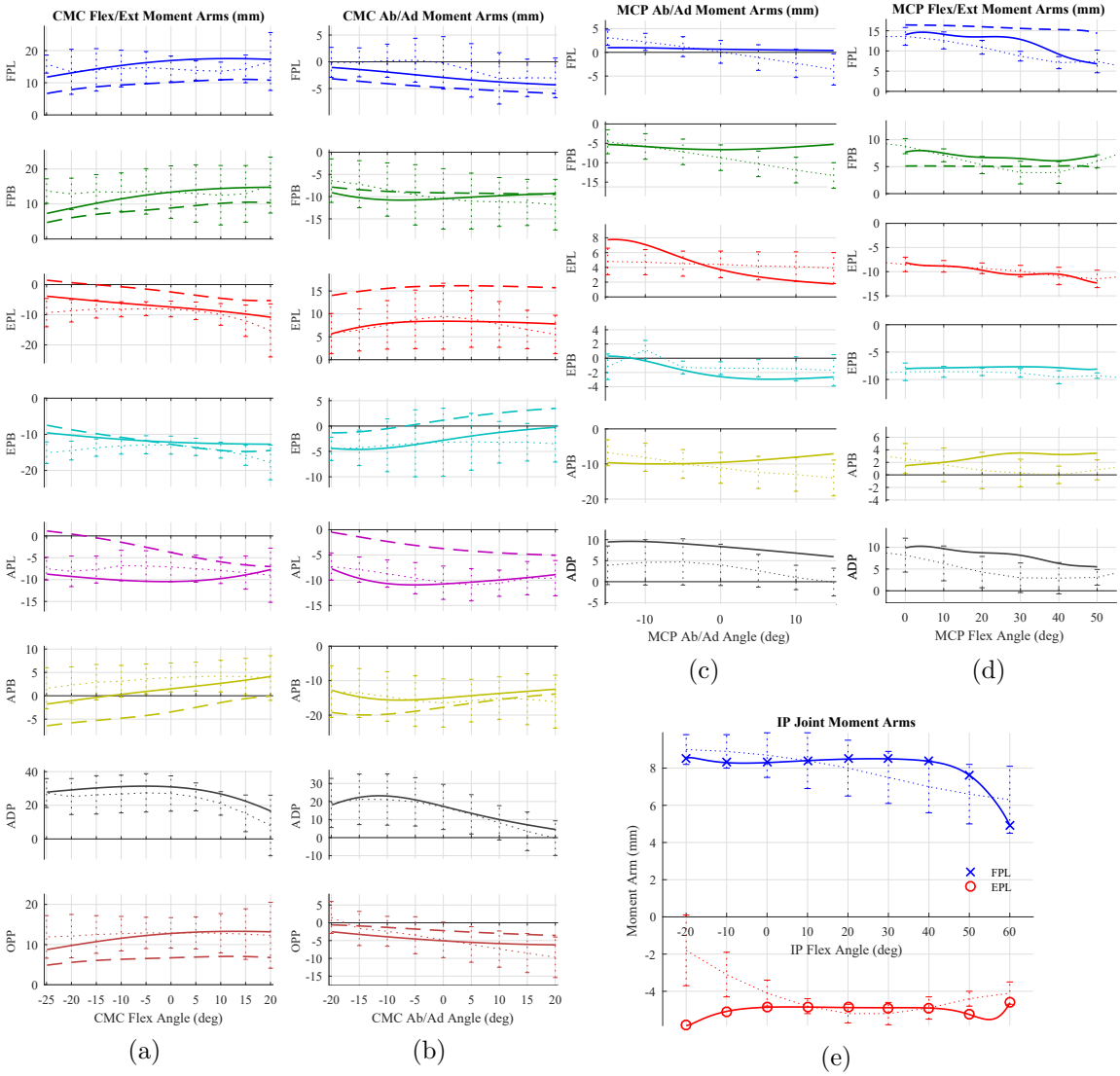

Figure 2.11: ACT thumb moment arms for the nominal model designed to match human MAs (solid lines) and the adjusted model designed to match thumb-tip forces (dashed lines, where modification was necessary), compared with experimental human data collected by Smutz et al. (1998) (dotted lines with error bars, mean ± 1 S.D.). Positive angles and moment arms for ab/ad joints correspond to thumb adduction (toward the palm).

Table 2.2: Experimentally collected ACT thumb-tip force data

	FPL	FPB	EPL	EPB	APL	APB	ADP	OPP
Opposition Pinch								
Nominal Model								
$\|F\|_{error}$ (%)[a]	57.8	**34.0**	51.3	43.6	90.9	**17.9**	**2.1**	185.7
ϕ_{error} (deg)[b]	81.3	**5.4**	**25.5**	43.7	**26.5**	31.6	**39.4**	**16.7**
Adjusted model								
$\|F\|_{error}$ (%)[a]	**10.0**	**12.3**	**6.2**	**0.3**	**4.5**	**1.0**	—[*]	**30.2**
ϕ_{error} (deg)[b]	**6.1**	**12.5**	**25.5**	**31.2**	**9.2**	**14.6**	—[*]	**13.2**
Key Pinch								
Nominal model								
$\|F\|_{error}$ (%)[a]	49.5	60.8	42.0	166.5	**15.3**	**25.1**	50.8	129.2
ϕ_{error} (deg)[b]	90.3	**8.3**	**36.4**	75.6	**26.2**	53.3	**18.6**	**2.3**
Adjusted model								
$\|F\|_{error}$ (%)[a]	**11.1**	**4.8**	29.1	**13.6**	43.0	**23.8**	—[*]	**43.9**
ϕ_{error} (deg)[b]	**6.2**	**10.1**	**27.6**	**25.8**	**9.9**	24.3	—[*]	**0.9**

[a] Force magnitude error: $\|F\|_{error} = \left|\frac{\|\mathbf{F}_{simulated}\| - \|\mathbf{F}_{reported}\|}{\|\mathbf{F}_{reported}\|}\right|$. Bold numbers indicate cases in which thumb-tip force magnitude is within experimental range (mean ± S.D.) reported by Pearlman et al. (2004).

[b] Force direction error: $\phi_{error} = cos^{-1}\left(\frac{\mathbf{F}_{simulated} \cdot \mathbf{F}_{reported}}{\|\mathbf{F}_{simulated}\|\|\mathbf{F}_{reported}\|}\right)$. Bold numbers indicate cases in which thumb-tip force directionality is within experimental ranges (mean ± S.D.) reported by Pearlman et al. (2004) in both the radial and dorsal planes (see Figures 2.12-2.13).

[*] Modification of the ADP tendon was deemed to be unnecessary, because the thumb-tip force vector already matched human data well enough that it did not require adjustment (see Figures 2.12-2.13). Thus, the ADP for nominal and adjusted models are identical.

model, designed to better match thumb-tip forces reported by Pearlman et al. (2004), deviates from human moment arm data and in many cases falls outside of reported ranges.

2.2.2.2 Thumb-Tip Forces

The thumb-tip force vectors produced by each muscle are next compared to cadaveric data from Pearlman et al. (2004). The nominal model did not match the reported force vectors in the majority of cases in either opposition or key pinch

postures, as seen in Table 2.2. However, in the adjusted model, tendon routing adjustments based on static thumb simulations lead to dramatically improved thumb-tip force matching, with nearly all thumb-tip forces falling within reported ranges (see Table 2.2 and Figures 2.12-2.13).

The moment arm sensitivity analysis indicates the necessary precision for thumb-tip force matching (Table 2.3). In general, flexion/extension moment arms required higher precision than abduction/adduction, likely due to the sensitivity of force magnitude and direction in the radial plane to the relative values of flexor moment arms. Additionally, thumb-tip forces are much more sensitive to moment arm variations in opposition pinch as compared to key pinch. This because the MCP joint is less flexed in opposition pinch (10^o vs. 45^o), meaning the thumb is closer to a kinematic singularity position, near which small changes in joint torques result in large deviations in end-tip force.

2.2.3 Discussion

Our results show that the ACT thumb is capable of faithfully representing human thumb mechanical structure and muscle functionality. It has been noted in the literature that the moment arms reported by Smutz et al. (1998) should not be considered definitive (Wohlman and Murray, 2013; Pearlman et al., 2004). Therefore, a nominal ACT model is created first based on data from Smutz et al. (1998). Then, informed by our static computer simulation model and sensitivity analysis (Table 2.3), the necessary modifications to ACT tendon routing are determined to create an adjusted ACT model that better replicates thumb muscle functionality and thumb-tip force production as reported by Pearlman et al. (2004).

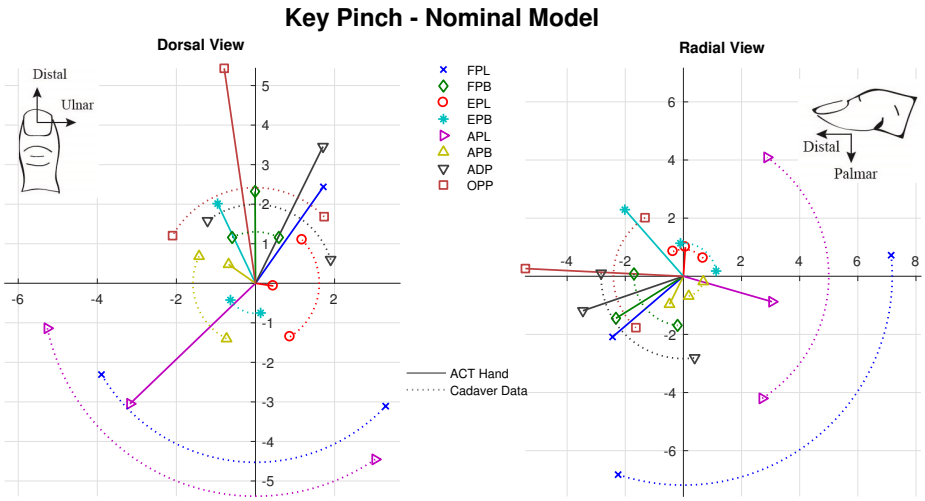

(a)

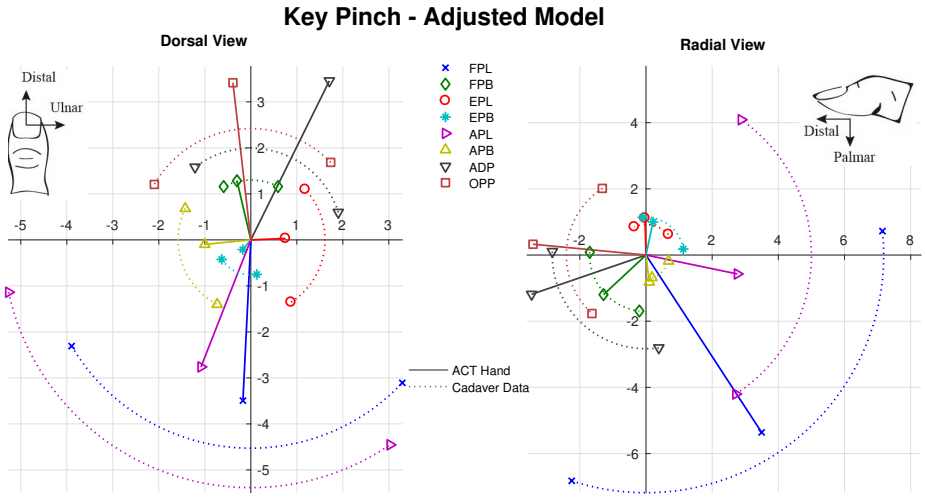

(b)

Figure 2.12: Thumb-tip force data from the ACT thumb in key pinch posture, i.e. thumb-tip touching index finger PIP joint, when forces are applied to each thumb muscle individually. All data is rotated to apply to a right hand. Muscle force values are identical to the maximum forces from cadaveric experiments from Pearlman et al. (2004). (a) Nominal ACT thumb model, designed to match cadaveric moment arm measurements from Smutz et al. (1998). (b) Adjusted ACT thumb model, re-designed to better match thumb-tip forces from Pearlman et al. (2004). Solid lines represent experimental force vectors from the ACT thumb, and dashed arcs represent the magnitude (mean) and angle (mean $\pm$ S.D.) of cadaveric data reported by Pearlman et al. (2004). The force vector is said to show a good directional match if it falls within the corresponding dashed arc. Actual values are reported in Table 2.2.

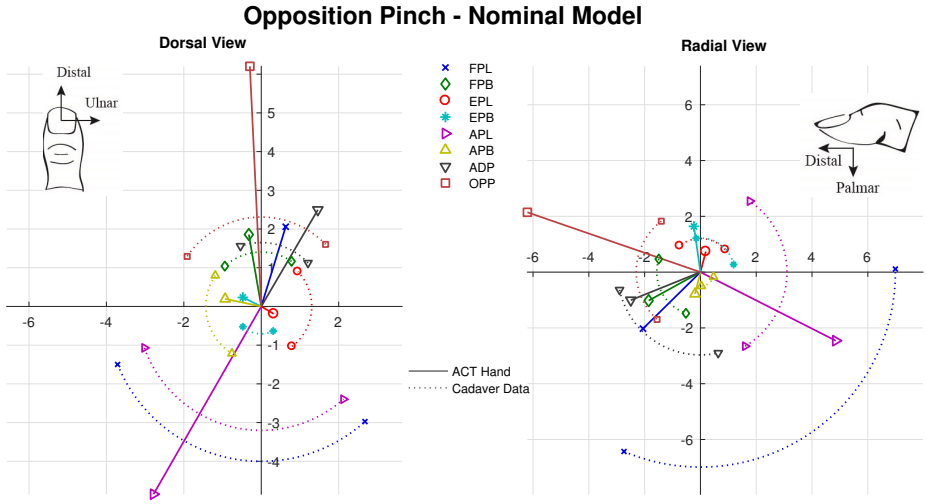

(a)

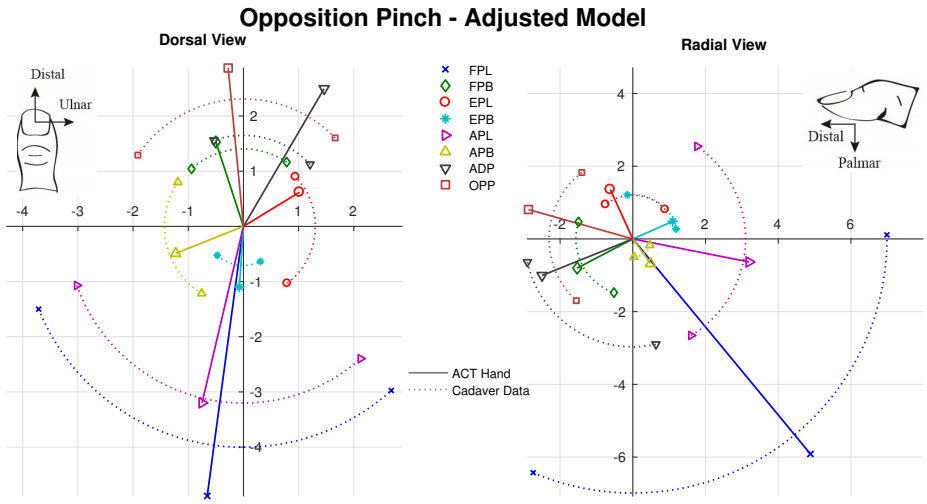

(b)

Figure 2.13: Thumb-tip force data from the ACT thumb in opposition pinch posture, i.e. thumb-tip touching index fingertip, when forces are applied to each thumb muscle individually. All data is rotated to apply to a right hand. Muscle force values are identical to the maximum forces from cadaveric experiments from Pearlman et al. (2004). (a) Nominal ACT thumb model, designed to match cadaveric moment arm measurements from Smutz et al. (1998). (b) Adjusted ACT thumb model, re-designed to better match thumb-tip forces from Pearlman et al. (2004). Solid lines represent experimental force vectors from the ACT thumb, and dashed arcs represent the magnitude (mean) and angle (mean $\pm$ S.D.) of cadaveric data reported by Pearlman et al. (2004). The force vector is said to show a good directional match if it falls within the corresponding dashed arc. Actual values are reported in Table 2.2.

Table 2.3: Sensitivity analysis of thumb-tip force production

	FPL	FPB	EPL	EPB	APL	APB	ADP	OPP
Opposition Pinch								
Nominal model								
$\|F\|_{error}$ (%)[a]	80.3	816.1	479.9	448.5	178.7	421.8	211.4	985.9
ϕ_{error} (deg)[b]	10.0	98.9	56.5	63.5	44.7	66.0	79.5	42.6
Adjusted model [c]								
MA bounds	±1 SD	±1 SD	±1 SD	±1.5 SD	±1.5 SD	±1 SD	±1 SD	±2 SD
$\|F\|_{error}$ (%)[a]	0.7	31.1	4.2	27.9	24.2	0.9	13.5	49.7
ϕ_{error} (deg)[b]	2.8	4.9	0.0	2.3	39.8	0.0	4.3	32.7
Allowable Variation (mm)								
CMC flex MA	1.2	1.6	1.3	1.3	0.9	1.8	2.8	3.6
CMC ab/ad MA	2.1	2.7	2.5	2.1	1.3	3.0	4.5	3.9
MCP ab/ad MA	0.9	1.1	0.9	0.9	—	1.4	2.0	—
MCP flex MA	0.5	0.7	0.5	0.6	—	0.8	1.1	—
IP flex MA	0.7	—	0.7	—	—	—	—	—
Key Pinch								
Nominal model								
$\|F\|_{error}$ (%)[a]	25.4	39.7	77.4	113.5	55.7	5.7	111.8	154.6
ϕ_{error} (deg)[b]	141.3	22.9	62.6	63.1	32.8	76.0	48.7	29.4
Adjusted model [c]								
MA bounds	±2 SD	±2 SD	±1 SD	±3 SD	±1 SD	±1 SD	±1 SD	±1 SD
$\|F\|_{error}$ (%)[a]	11.3	0.2	7.6	18.4	25.4	6.9	0.2	31.5
ϕ_{error} (deg)[b]	9.3	0.0	21.0	5.7	19.4	12.4	0.0	16.7
Allowable Variation (mm)								
CMC flex MA	3.6	8.1	7.0	4.4	6.5	6.6	10.5	8.2
CMC ab/ad MA	15.9	4.5	5.6	3.8	11.5	5.1	12.1	9.9
MCP ab/ad MA	12.6	4.6	5.4	3.4	—	3.4	10.4	—
MCP flex MA	1.2	4.2	2.6	2.3	—	2.3	5.8	—
IP flex MA	1.8	—	3.6	—	—	—	—	—

[a] Force magnitude error: $\|F\|_{error} = \left| \frac{\|\mathbf{F}_{simulated}\| - \|\mathbf{F}_{reported}\|}{\|\mathbf{F}_{reported}\|} \right|$.

[b] Force direction error: $\phi_{error} = cos^{-1}\left(\frac{\mathbf{F}_{simulated} \cdot \mathbf{F}_{reported}}{\|\mathbf{F}_{simulated}\|\|\mathbf{F}_{reported}\|} \right)$.

[c] Adjusted model obtained through minimization of the cost function $\|\mathbf{F}_{simulated} - \mathbf{F}_{reported}\|$, with moment arms constrained to the indicated ranges from nominal values (SDs as reported by Smutz et al. (1998)) to allow convergence of thumb-tip forces to within experimental ranges reported by Pearlman et al. (2004). For the APL and OPP (single-joint muscles), joint deviations of ± 15^o were allowed at the MCP and IP flexion joints to facilitate directional fit, particularly in the radial plane (Goehler and Murray, 2010).

The finding that a nominal biomechanical thumb model with experimental moment arms from Smutz et al. (1998) fails to replicate human-like thumb-tip force production has been reported in multiple previous works (Valero-Cuevas et al., 2003; Wohlman and Murray, 2013). The level of variability present in the thumb's musculotendon routing (Smutz et al., 1998) and joint structure (Santos and Valero-Cuevas, 2006) creating a normative model of a human thumb a challenging task. Additionally, there exist inconsistencies in the definitions of CMC joint axes, especially considering Smutz et al. (1998) defined CMC joint motions with respect to the plane of the palm. Thus, a biomechanical thumb model using anatomical non-intersecting CMC joint axes from Hollister et al. (1992) requires CMC moment arm transformation, something that to our knowledge has not been addressed in the literature. Initial support of this claim is evidenced by superior force matching of the nominal ACT model in Table 2.2, which accounts for the transformation, compared to the nominal simulation model in Table 2.3, which did not apply this transformation.

Analysis of the required modifications between the nominal and adjusted models can also provide insights into the sources of discrepancies between experimental human moment arms (Smutz et al., 1998) and experimental thumb-tip forces (Pearlman et al., 2004). For example, in the nominal model, the mono-articular OPP and APL produced force magnitudes much larger than human thumb-tip data, so the adjusted model implemented reduced moment arms for these two muscles. In the human thumb, it is possible that applying large tensions to the OPP or APL would lead to significant CMC joint translation due to inherent joint elasticity, which might similarly reduce their effective moment arms.

The relationship between thumb-tip force and muscle tension in human thumbs

has been reported to be nonlinear, most likely due to load-dependent bone translation and viscoelastic muscle-tendon paths (Pearlman et al., 2004). The ACT thumb has an arrangement of rigid tendon routing points that are incapable of replicating force-dependent changes in tendon lines of action. Instead, researchers can use the tools developed here to, depending on the task parameters such as expected muscle forces, design custom tendon routing that can approximate the human thumb's muscle-to-end-tip force transformation near the operating conditions they are exploring.

Although the ACT hand represents a powerful tool, there are inherent limitations that may affect the accuracy of these results. Differentiation of a fitted model has issues, especially near joint limits, which could effect the accuracy of presented moment arm plots. Joint angles of the ACT thumb during thumb-tip force testing may not precisely match thumb postures in human studies, which could affect the resulting thumb-tip force vectors (Goehler and Murray, 2010). The joints in the ACT thumb are hinge joints, but bone translations and sliding in human thumbs could result in a more complex kinematic model (Towles et al., 2008).

2.3 Summary of Human Hand Mechanical Modeling

In this chapter, I have investigated the kinematic and force relationships that arise from the unique musculotendon structure of the human hand, and developed analytical tools and physical models capable of closely matching the mechanics of human fingers and thumbs. Accurate models of the fingers and thumb provide us with a clearer understanding of human hand functionality during dexterous tasks, and will also be utilized in later chapters for the development of control algorithms for the human-like ACT hand system.

Chapter 3

Dexterous Manipulation with the Anthropomorphic Robonaut 2 Hand

The hands of the space humanoid Robonaut 2 (R2) are designed to achieve human-like grasping and manipulation in an unstructured environment such as the International Space Station (ISS) (Bridgwater et al., 2012). The fingers and thumbs are tendon-driven to allow for remote actuation and reduced finger size and weight. The primary (index and middle) fingers and the thumbs each have $N + 1$ tendons for N joints, which leads to full finger controllability ($N = 3$ for primary fingers and $N = 4$ for thumbs). While this $N + 1$ tendon arrangement is attractive due to the low actuator count and space requirement, it also results in a complex control problem, especially for impedance control. So far, a joint-space torque control law for the individual R2 fingers has been developed (Abdallah et al., 2010) that solves the tendon tension distribution problem and produces decoupled motions in the joint-space, but Cartesian control of the fingertips has not yet been explored.

In this chapter, first a Cartesian stiffness control algorithm is presented for the individual R2 fingers and thumbs. In the finger Cartesian control algorithm, modifications were made based on the finger kinematics for singularity avoidance and

Portions of this chapter have been previously published in the proceedings of the 2014 IEEE International Conference on Robotics and Automation (ICRA) (Niehues et al., 2014).

Figure 3.1: The Robonaut 2 (R2) upper body system and examples of the challenging manipulation tasks to be performed by the R2 hands on the International Space Station.

Table 3.1: Description of generalized variables for tendon-driven robotic hands.

Variable	Description
$\boldsymbol{\ell}_m$	muscle/tendon positions
$\mathbf{f}_m$	muscle/tendon forces (tensions)
$\boldsymbol{\theta}$	joint angles
$\boldsymbol{\tau}$	joint torques
$\mathbf{x}$	end-tip Cartesian position
$\mathbf{f}_x$	end-tip Cartesian forces
$\mathbf{z}$	object-space position/orientation
$\mathbf{f}_z$	object-space force/torque
$R(\boldsymbol{\theta})$	moment arm matrix
$J(\boldsymbol{\theta})$	Jacobian matrix
$W(\mathbf{x})$	grasp matrix

improved grasp closure capabilities, and force feedback is provided solely by tendon tension sensors.

Then, an object-level stiffness control strategy is developed to perform object manipulation tasks while remaining robust against impacts and other disturbances and uncertainties. In the past, the R2 hands accomplished grasping and manipulation tasks by defining finger joint trajectories which are generated specifically for a given object. This method requires complex path planning and makes contact force regulation difficult. The object stiffness controller developed in this work has the advantages of safer environmental interactions, user-definable object stiffness properties, and easily regulated grasp forces.

3.1 Generalized Model of Tendon-Driven Robot

I will begin by defining the variables and presenting equations for transforming displacements and forces between frames located in tendon-, joint-, end-tip, and object-space. A full table of variables with descriptions can be found in Table 3.1.

As previously defined in Section 2.1, the relationship between muscle/tendon forces, joint torques, and end-tip forces are defined as follows:

$$\boldsymbol{\tau} = R(\boldsymbol{\theta})\mathbf{f}_m \tag{2.1}$$

$$\boldsymbol{\tau} = J^T(\boldsymbol{\theta})\mathbf{f}_x \tag{2.12}$$

By conservation of power, the corresponding displacement relations are:

$$\delta\boldsymbol{\ell}_m = R^T(\boldsymbol{\theta})\delta\boldsymbol{\theta} \tag{3.1}$$

$$\delta\mathbf{x} = J(\boldsymbol{\theta})\delta\boldsymbol{\theta} \tag{3.2}$$

The object-space coordinates $\mathbf{z}$ and forces $\mathbf{f}_z$ are defined by an object frame, such that $\mathbf{z}$ corresponds to the translational position and orientation of the object and $\mathbf{f}_z$ to the force/torque applied to the object's center. If the end-tip forces $\mathbf{f}_{x,i}$ and positions $\mathbf{x}_i$ for each digit i are concatenated into a vectors of contact point positions $\mathbf{x}$ and forces $\mathbf{f}_x$, the transformation between end-tip-space and object-space can be defined through the grasp matrix:

$$\mathbf{f}_z = W(\mathbf{x})\mathbf{f}_x \tag{3.3}$$

$$\delta\mathbf{x} = W^T(\mathbf{x})\delta\mathbf{z} \tag{3.4}$$

3.2 Cartesian Control of R2 Fingers and Thumb

To begin, Cartesian control strategies are developed for the individual R2 fingers and thumbs. This problem is divided into two control sub-tasks: control of torques produced at each finger joint through tension feedback, and implementation of a Cartesian stiffness controller for regulation of both fingertip positions and forces.

3.2.1 Joint Torque Controller

To control the finger joint torques, the joint-space controller proposed by Abdallah et al. (2010) is utilized. The joint torques $\boldsymbol{\tau}$ and internal tension t can be calculated from measured tendon tension values, $\mathbf{f}_m$, through the relation:

$$\bar{\boldsymbol{\tau}} = \begin{bmatrix} \boldsymbol{\tau} \\ t \end{bmatrix} = \begin{bmatrix} R \\ \text{null}(R) \end{bmatrix} \mathbf{f}_m = P\mathbf{f}_m \tag{3.5}$$

where $P \in \mathbb{R}^{n_m \times n_m}$ is the tendon map matrix containing the moment arm matrix R, which is constant due to the R2 hand's circular tendon pulleys, concatenated with a row vector in the null-space of R corresponding to tendon force combinations that produce zero net joint torque.

The actuators already employ well-tuned PD position control loops, so the torque control algorithm should pass down desired actuator positions $\boldsymbol{\ell}_{m,d}$ to the motor controllers. Given a desired set of joint torques $\boldsymbol{\tau}_d$ as input, the tension distribution algorithm of Abdallah et al. (2010) is used to determine an appropriate internal tension parameter t_d and, if necessary, linearly scale down $\boldsymbol{\tau}_d$ until the tendon forces $\mathbf{f}_m$ fall within the desired bounds $[f_{min}, f_{max}]$. The resulting vector of desired joint torques and internal tension, $\bar{\boldsymbol{\tau}}_d$, will maintain a minimum tendon tension to avoid slacking and account for actuator saturation effects without introducing joint coupling.

Finally, a joint-space torque controller is defined as

$$\boldsymbol{\ell}_{m,d} = \boldsymbol{\ell}_m - k_d\dot{\boldsymbol{\ell}}_m + P^T K_p(\bar{\boldsymbol{\tau}}_{m,d} - \bar{\boldsymbol{\tau}}) \tag{3.6}$$

where k_d is a scalar damping gain and K_p is a proportional torque and internal tension feedback diagonal gain matrix. See the work of Abdallah et al. (2010) for more details

and experimental results for the tension distribution algorithm and joint-space torque controller.

3.2.2 Cartesian Stiffness Controller

For accurate control of fingertip positions and forces, it is desirable to create a fingertip Cartesian stiffness relation of the form:

$$\mathbf{f}_{x,d} = K_x(\mathbf{x}_d - \mathbf{x}) \tag{3.7}$$

where the fingertip position $\mathbf{x}$ is calculated from the joint angles $\boldsymbol{\theta}$ using the forward kinematics and K_x is the desired Cartesian stiffness matrix. The desired forces $\mathbf{f}_{x,d}$ could then be transformed to desired joint torques using Equation (2.12) and be sent to the joint torque controller in the previous section.

For the R2 system, stiffness control was chosen over a full impedance control strategy because it is not necessary to explicitly regulate the Cartesian damping or inertia properties of R2 hand. The joint torque control algorithm of the previous section can be easily tuned to produce a critically damped response, eliminating the need for damping controls, and the finger inertias are small enough that inertia shaping is not necessary (Bridgwater et al., 2012).

The above stiffness relation is the foundation of the R2 Cartesian stiffness controllers. However, slight modifications will be presented in the next section to account for the specific kinematics of the R2 thumb and primary fingers. Note that the ring and little fingers of the R2 hand are both under-actuated (3 tendons to control 4 DOFs) and thus not fully controllable in Cartesian-space, and so will not be addressed in this work.

3.2.2.1 Thumb

In the case of the thumb, simply using the Jacobian $J(\boldsymbol{\theta}) \in \mathbb{R}^{3\times4}$ to transform from 3-D Cartesian forces to four joint torques leaves one uncontrolled internal DOF. To address this, we explicitly control the thumb's distal joint angle θ_4 with a desired joint stiffness. Control of the distal joint angle is useful during grasping and manipulation tasks, allowing us to ensure contact that is being made with the flat pad of the thumb for a more stable grasp. This results in a new joint torque formulation,

$$\boldsymbol{\tau}_d = \begin{bmatrix} (J_{3\times3})^T K_{x,thumb}(\mathbf{x}_d - \mathbf{x}) \\ k_{dist}(\theta_{4d} - \theta_4) \end{bmatrix} \tag{3.8}$$

where $J_{3\times3}$ is the thumb Jacobian $J(\boldsymbol{\theta}) \in \mathbb{R}^{3\times4}$ with the last column removed and k_{dist} is the distal joint stiffness gain.

3.2.2.2 Primary Fingers

In the primary fingers, a singular position occurs when the fingertip is aligned with the proximal yaw joint. At this singularity, movement of the yaw joint produces zero change in the fingertip Cartesian position, meaning the finger cannot produce lateral motions or forces. Because the finger frequently must move through this singular position, combined with the yaw joint being already relatively ill-conditioned due to its smaller joint radii, the controller tends to perform poorly near this singularity. Therefore, instead of implementing Cartesian control of fingertip lateral motions, joint stiffness control of the yaw joint θ_1 is implemented, such that

$$\boldsymbol{\tau}_d = \begin{bmatrix} 1 & 0 & 0 \\ 0 & & \\ 0 & & (J_{2\times2})^T \end{bmatrix} K_{x,prim} \begin{bmatrix} \theta_{1d} - \theta_1 \\ y_d - y \\ z_d - z \end{bmatrix} \tag{3.9}$$

where $K_{x,prim} = \text{diag}(k_{yaw}, k_y, k_z)$ is the new stiffness gain matrix for primary fingers and $J_{2\times2}$ is the finger Jacobian $J(\boldsymbol{\theta}) \in \mathbb{R}^{3\times3}$ after removing the column representing

the yaw joint and the row representing the lateral Cartesian direction. Using this reduced Jacobian, we will only specify a Cartesian stiffness in two directions: the z-direction defined as orthogonal to the plane of the palm, and the y-direction defined parallel to the plane of the palm and orthogonal to the proximal flexion/extension joint axis.

This produces more stable and controllable motions throughout the finger's range of motion without hampering our ability to control fingertip Cartesian position and force, due to the simplicity of transforming from lateral position/force to yaw joint angle/torque, and vice versa. Control of the yaw joint also helps us in more effectively managing the location of the point of contact on the finger's surface during environmental interactions, i.e. to avoid grasping of an object with the side of a finger.

To avoid singularity positions and also to avoid hitting mechanical hard stops at the joint limits, repelling torques are used at each finger joint:

$$\tau_{lim,i} = \begin{cases} -k_i[\theta_i - (\theta_{i,max} - \delta_i)], & \text{for } \theta_i > \theta_{i,max} - \delta_i \\ k_i[\theta_i - (\theta_{i,min} + \delta_i)], & \text{for } \theta_i < \theta_{i,min} + \delta_i \\ 0 & \text{otherwise} \end{cases} \tag{3.10}$$

where $\theta_{i,min}$, $\theta_{i,max}$ are the joint limits, δ_i is the desired safe distance, and k_i is the repelling stiffness. This repelling torque is added to the joint torques of the Cartesian controller, and keeps both the primary fingers and thumb away from singularity positions.

The total desired torques $\boldsymbol{\tau}_d$ calculated here will be passed down to the joint-space controller in Section 3.2.1. The gains K_p and k_d in Equation (3.6) are tuned to give the Cartesian stiffness controller a critically damped step response.

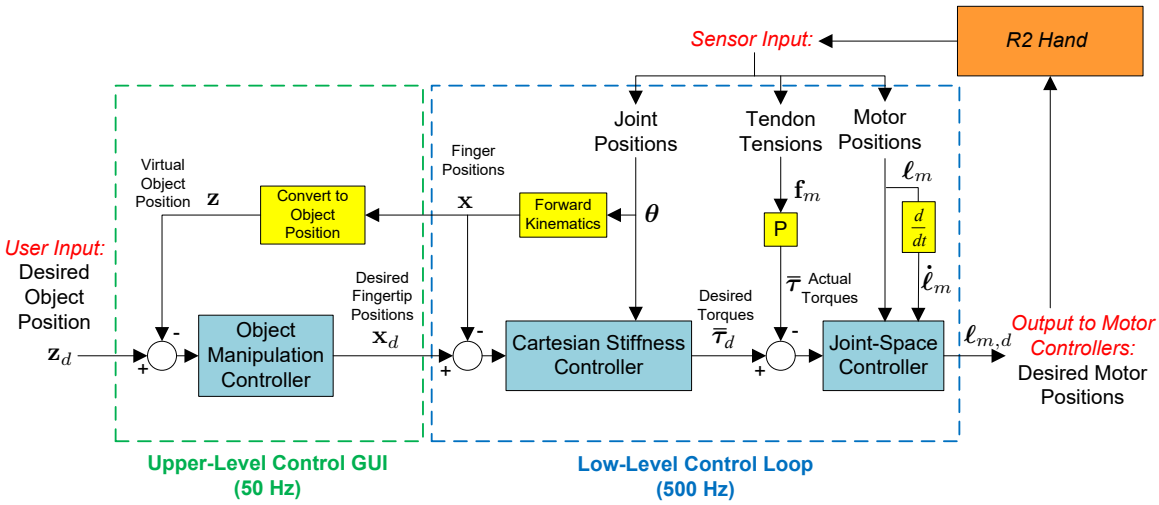

Figure 3.2: Block diagram for complete control system, including the high-level object stiffness controller and the low-level finger Cartesian stiffness and joint-space torque controllers. Note that the finger positions $\mathbf{x}$ and $\mathbf{x}_d$ include the primary finger yaw joint (θ_1) and thumb distal joint (θ_4) angles to be used by the Cartesian controllers.

3.3 Object Manipulation Controller

The goal of the object manipulation controller is to robustly grasp and manipulate an object using the thumb and two primary fingers. In this work, the manipulation problem is simplified by focusing only on 2-D motions on a plane parallel to the palm of the hand. The object-space coordinates are described by the 2-D translational position (x_o, y_o), defined as the centroid of the three fingertip positions, and the object angle ϕ, defined as the angle between (x_o, y_o) and thumb in a plane parallel to the palm (see Figure 3.3 for a visual representation). Thus, $\mathbf{z} = [x_o, y_o, \phi]^T$ and $\mathbf{x} \in \mathbb{R}^6$ contains only the 2-D (x,y) components of finger/thumb positions. Then, an object-space stiffness force is defined as:

$$\mathbf{f}_z = \begin{bmatrix} f_{x,o} \\ f_{y,o} \\ \tau_o \end{bmatrix} = K_z \begin{bmatrix} x_{od} - x_o \\ y_{od} - y_o \\ \phi_d - \phi \end{bmatrix} \tag{3.11}$$

where K_z is a diagonal object stiffness matrix.

The inverse relation, which will be used to calculate contact forces $\mathbf{f}_x$ to be applied by the fingers/thumb based on a desired $\mathbf{f}_z$, the generalized pseudo-inverse $W^+(\mathbf{x})$ is utilized along with the null-space matrix $N(\mathbf{x})$ containing the internal forces. However, simply calculating the null-space of $W(\mathbf{x}) \in \mathbb{R}^{3\times6}$ results in $N(\mathbf{x}) \in \mathbb{R}^{6\times3}$, which would require controller optimization of three separate internal force variables. To reduce the null-space, we introduce an additional constraint that the line of action of the internal forces must pass through the object's center. The internal forces produced using this constraint will act similar to those produced by the passivity-based object controller of Wimböck et al. (2006), which uses virtual springs connecting each fingertip to the center of the object.

For example, a constraint for the thumb would be:

$$\begin{aligned} \frac{f_{tb,y}}{f_{tb,x}} &= \frac{y_{tb} - y_o}{x_{tb} - x_o} \\ (y_{tb} - y_o) f_{tb,x} - (x_{tb} - x_o) f_{tb,y} &= C_1(\mathbf{x})\mathbf{f}_x = 0 \end{aligned} \tag{3.12}$$

where $C_1(\mathbf{x}) \in \mathbb{R}^{1\times6}$ is a constraint row vector. In the same way, we set up a similar constraint row vector $C_2(\mathbf{x})$ for either one of the primary fingers, such that $C_2(\mathbf{x})\mathbf{f}_x = 0$. Then, we can reduce $N(\mathbf{x})$ to a null-space column vector $\mathbf{n}(\mathbf{x}) \in \mathbb{R}^6$:

$$\mathbf{n}(\mathbf{x}) = \text{null}\left(\begin{bmatrix} W(\mathbf{x}) \\ C_1(\mathbf{x}) \\ C_2(\mathbf{x}) \end{bmatrix}\right) \tag{3.13}$$

This definition of the null-space ensures that forces acting in the space of $\mathbf{n}(\mathbf{x})$ produce zero net object forces or torques and also realize the two constraint equations, such that the internal force vector will only produce forces passing through the object's center. Now, the contact forces are calculated using the following equation:

$$\mathbf{f}_x = W^+(\mathbf{x})\mathbf{f}_z + \mathbf{n}(\mathbf{x}) f_{int} \tag{3.14}$$

The internal force component, f_{int}, is calculated such that the minimum normal force being produced at the three fingertips is greater than some prescribed minimum force $f_{grip,min}$.

The desired end-tip contact forces $\mathbf{f}_{x,i}$ for each digit i are then converted into desired fingertip positions using Equation (3.7) for the each finger's Cartesian control loop. For example, given a desired endpoint force $f_{x,ij}$ for digit i in the Cartesian direction j, the desired Cartesian position $x_{d,ij}$ is found as:

$$x_{d,ij} = x_{ij} + \frac{f_{x,ij}}{k_{x,ij}} \tag{3.15}$$

where $k_{x,ij}$ is the Cartesian stiffness for that particular finger and direction. Then, the desired position $\mathbf{x}_d$ for each finger will be passed down to the corresponding Cartesian controller in Section 3.2.2.

For the thumb, the commanded distal joint position θ_{4d} is set to an angle ideal for maximum contact area on the thumb pad. For the primary fingers, the total torque at the base required to produce the desired fingertip force is calculated as

$$\boldsymbol{\tau}_{base} = \mathbf{r}_{tip}^{base} \times \mathbf{f}_x \tag{3.16}$$

where $\mathbf{r}_{tip}^{base}$ is the vector from the finger base to the fingertip. The desired yaw torque τ_{yaw} is the component of $\boldsymbol{\tau}_{base}$ parallel to the finger's yaw joint axis. Then, the desired yaw angle is found as

$$\theta_{1d} = \theta_1 + \frac{\tau_{yaw}}{k_{yaw}} \tag{3.17}$$

and passed down to the Cartesian controller. The ability to control the finger yaw angles is especially useful for spreading out the finger contact points to maintain a quality force-closure grasp, without requiring inverse kinematics calculations to

ensure joint limits will be avoided. Additionally, to ensure stability in the case of loss of contact with the object, the commanded fingertip positions $\mathbf{x}_d$ are restricted to remain a specified minimum distance away from the virtual object's center.

In the end, the higher-level object manipulation controller will pass down commanded Cartesian positions $\mathbf{x}_d$, primary yaw joint angles θ_{1d}, and thumb distal joint angles θ_{4d} to the finger Cartesian stiffness controllers (see Figure 3.2).

3.4 Experimental Manipulation Results

The object manipulation controller is implemented on the Robonaut 2 hand. A diagram illustrating the overall control structure is found in Figure 3.2. Individual finger Cartesian controllers, combined with joint-space controllers to determine output motor positions, are implemented on in a lower-level control loop, communicating with the motor controllers at a rate of 500 Hz. The higher-level object manipulation controller runs on a separate computer running the R2 control GUI, which sends finger position commands down to the low-level controller at a rate of 50 Hz.

This relatively slow communication rate would result in instability without the inherent stability provided by the lower-level finger Cartesian controllers. This communication hierarchy shows a structure similar to human hand neuromuscular control: the communication rate of neural signals between the brain and the hand is relatively slow, but the inherent stability and stiffness properties of the individual fingers (due to muscles, tendons, ligaments, joint capsules, etc.) allow robust manipulation abilities (Morasso, 2011). A more in-depth exploration of such hierarchical control strategies will occur in Chapter 5.

The control law is evaluated using steps commands in object z-axis rotation

Table 3.2: Controller parameters (units are mm, rad, and tension sensor force units).

Parameter	**Value**
Primary Finger Stiffness	
$K_{x,prim}$	$= diag(k_{yaw}, k_y, k_z) = diag(1000, 0.05, 0.1)$
Thumb Stiffness	
$K_{x,thumb}$	$= diag(k_x, k_y, k_z) = diag(0.05, 0.05, 0.1)$
k_{dist}	250
Step Response Object Controller Parameters	
K_z	$= diag(k_x, k_y, k_\phi) = diag(2.0, 2.0, 1500)$
$f_{grip,min}$	0.2
Disturbance Response Object Controller Parameters	
K_z	$= diag(k_x, k_y, k_\phi) = diag(0.5, 0.5, 1000)$
$f_{grip,min}$	0.5

and step commands in translation in the x and y directions. In addition, disturbance rejection experiments are performed to test the controller robustness and ensure the desired object stiffness is being produced. For all cases, desired object height above the palm is set to a constant value, such that the finger and object motions remain in a 2-D plane parallel to the palm. The object is a standard 1.4 ounce racquetball with a radius of 2.25 inches.

The joint-space torque feedback gain K_p is determined experimentally for each finger to produce accurate joint torque tracking and internal tension maintenance; variations in K_p matrices between the R2 fingers is necessary primarily because of tension sensor calibration errors. The damping gain k_d is set to 0.01. The remaining controller parameters used in the experiments can be found in Table 3.2. The prescribed finger stiffness in the z-direction is larger to keep the fingertips on a fixed 2-D plane above the palm.

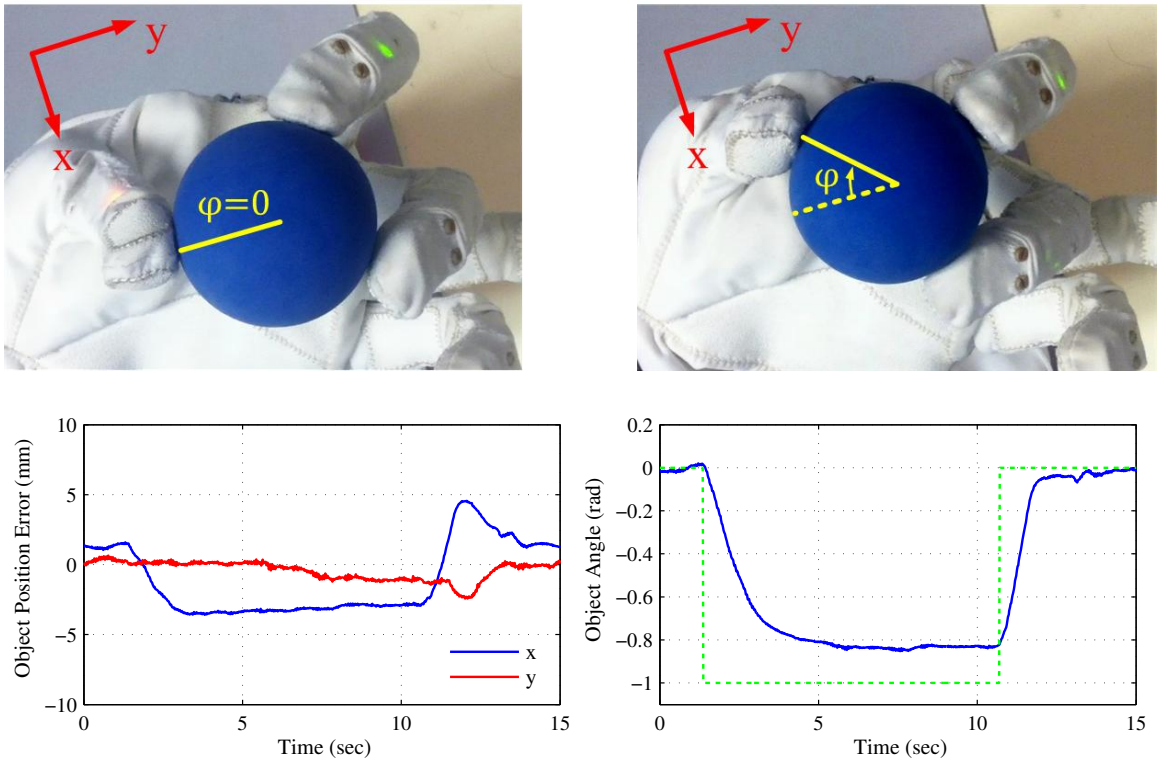

Figure 3.3: The R2 hand rotating an object about the z-axis, given a commanded object angle step input of $\Delta\phi = -1.0\ rad$.

3.4.1 Object Rotation

The object is rotated about the z-axis by giving a step input of $\Delta\phi = -1.0\ rad$ (Figure 3.3). The steady-state error in object angle and x occurs because the primary fingers both reach their yaw joint angle limits, causing the controller to compromise between the errors in x and object angle.

3.4.2 Object Translation

We perform object translation in the x-direction (laterally) by commanding a step input from from $x = -10\ mm$ to $x = -25\ mm$ (see Figure 3.4), where the

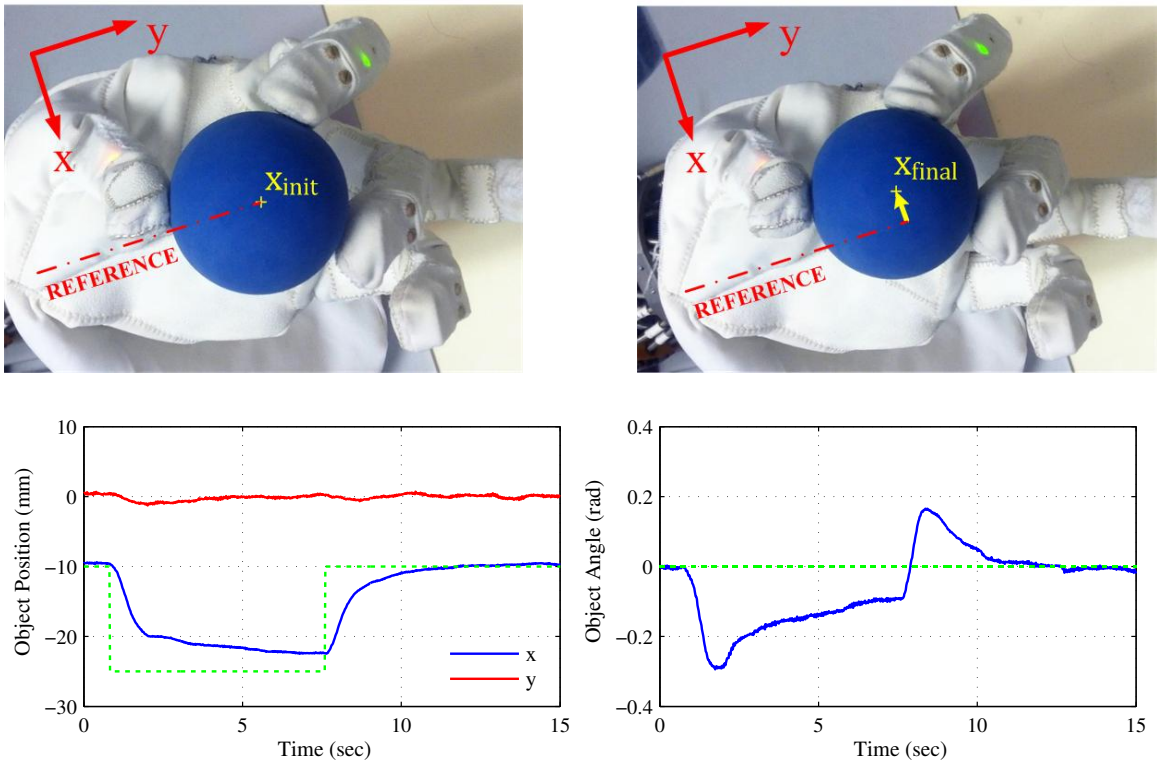

Figure 3.4: The R2 hand translating an object laterally, given a commanded x-direction step input from $x = -10\ mm$ to $x = -25\ mm$.

point $(x, y) = (0, 0)$ is located at the base of the middle finger. We once again see steady-state errors in x and object angle due to the primary fingers reaching their yaw joint limits.

Next, we test a step command in the y-direction of $y = 10\ mm$ to $y = -30\ mm$, as shown in Figure 3.5. We see minimal errors in x or object angle, and negligible steady-state error in y. The slower rise time moving in the positive y-direction is a result of the thumb overcoming the grip forces being applied the two primary fingers, which must remain fairly high to maintain contact without slipping.

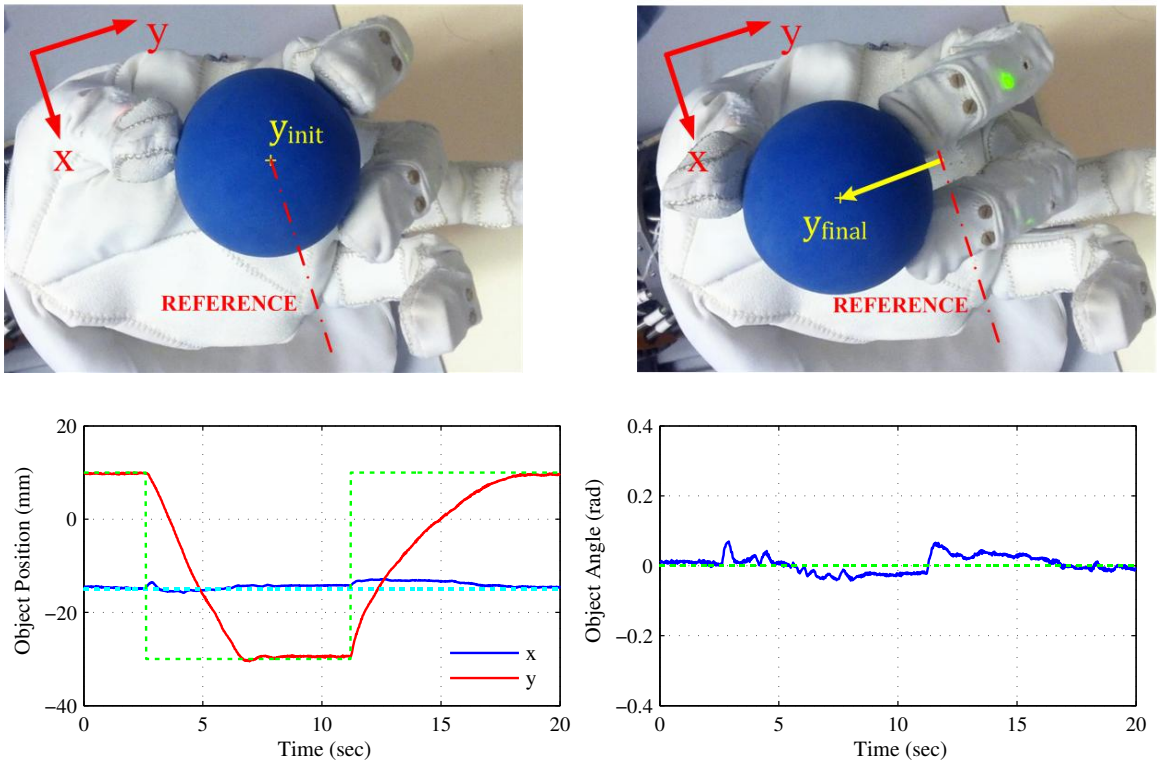

Figure 3.5: The R2 hand translating an object vertically, given a commanded y-direction step input from $y = 10\ mm$ to $y = -30\ mm$.

3.4.3 Disturbance Response

The disturbance response is analyzed to show the robustness of the controller. An external force is applied to the object, as shown in Figure 3.6, and the resulting position and tendon tensions were recorded. Note that the controller parameters were adjusted slightly (see Table 3.2) for clearer experimental results. The algorithm is able to maintain the desired posture effectively with an acceptable steady-state error. The advantages of this object stiffness controller over a more straightforward position controller is the ability to react to disturbances and continuously modify the fingertip forces to maintain a stable grasp.

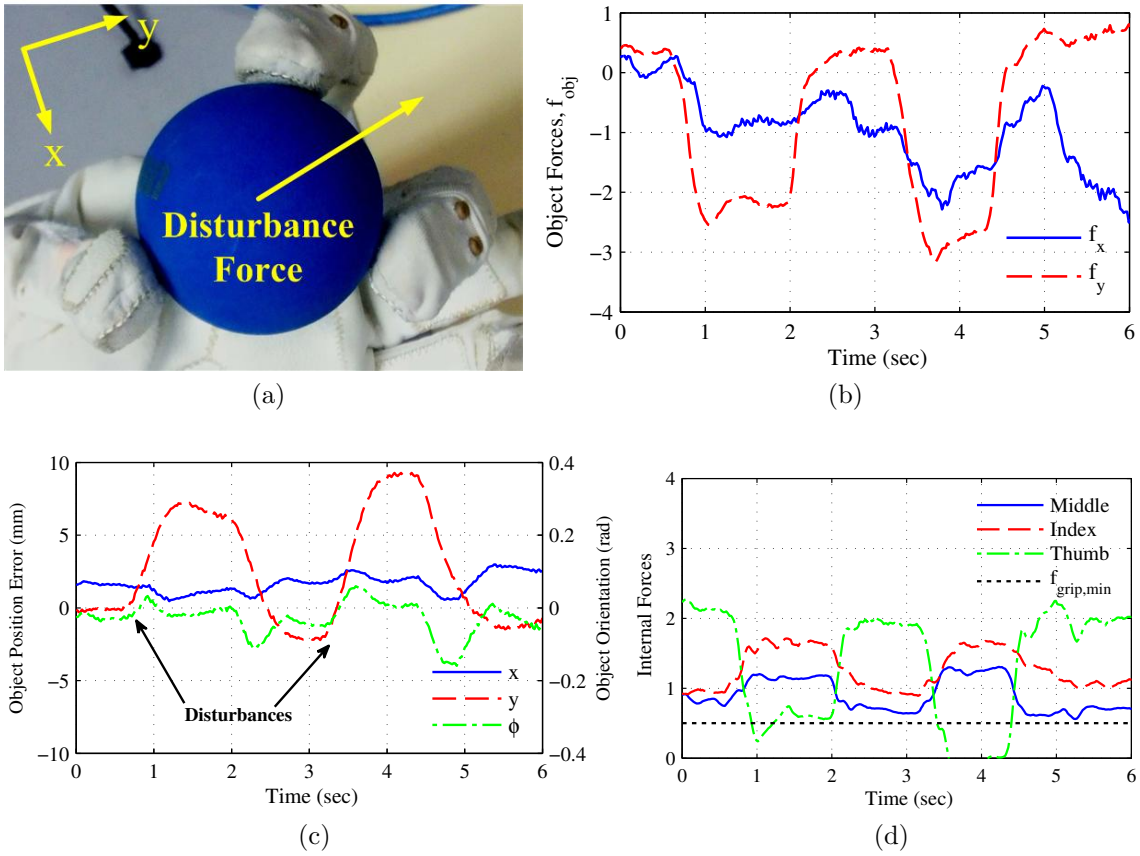

Figure 3.6: The R2 hand maintaining a fixed object position while rejecting externally applied disturbances, as shown in (a). The object's virtual position and orientation response through two disturbance impulses is shown in (c), while (b) and (d) shows the resulting object forces ($f_{obj,x}$, $f_{obj,y}$) and internal forces being exerted on the object by the fingertips.

The forces being applied to the object, calculated from the recorded tendon tensions and shown in Figure 3.6b, correspond approximately to the desired object stiffness. The internal forces in Figure 3.6d are defined as the component of fingertip forces passing through the center of the ball to produce a normal gripping force. There are intervals when the internal thumb force drops below the threshold. This occurs because the disturbance is being applied to the thumb instead of directly to the ball,

skewing measured thumb force values in the negative direction. Other than these instances, the desired minimum grip force of $f_{grip,min} = 0.5$ is maintained. Note that the tension sensors have an error of 5-10% caused by friction and interactions between tendon conduits (Bridgwater et al., 2012), which limits the controller's performance and precision.

3.5 Discussion

In this section, a Cartesian stiffness control law for the R2 fingers and thumb and a higher-level object control were developed to achieve fine manipulation with the R2 hand. The Cartesian controller is built upon a previously developed joint-space control algorithm with a number of novel additions and modifications. A novel hybrid Cartesian and joint stiffness control law was developed to avoid singularities in the primary fingers, and distal joint stiffness is added in the thumb for full controllability. The proposed controller provides intuitive control of fingertip positions and forces using position-controlled actuators and only tendon tension sensors as force feedback, and allows explicit control of key joint angles (primary finger yaw joints, thumb distal joints) that are important in manipulation tasks for ensuring good contact areas and stable grasping. The control law was then implemented on the R2 hand system as part of a higher-level object controller to perform fine manipulation with multiple fingers. The fingertip positions were used to define a virtual object position on a 2-D plane above the palm, which was subsequently used to implement an object stiffness control law. Experimental results demonstrate stable grasping, smooth object motions, and robustness against disturbances.

This chapter demonstrates how object manipulation is typically achieved in

robotic hands by using impedance control strategies. The R2 hand is designed with an anthropomorphic shape and an $N + 1$ tendon arrangement with circular pulleys, making joint control a relatively simple problem. By comparison, it was shown in Chapter 2 that the human hand has a much more complex tendon structure. In the next chapter, Cartesian and object-space impedance controllers will be developed for the human-like joint and tendon structure of the Anatomically Correct Testbed (ACT) hand. While this represents a significantly more complex control problem, it can potentially provide key insights into the unique functionality and dexterity of human hands.

Chapter 4

Dexterous Manipulation with the Anatomically Correct Testbed Hand

In this chapter, I will develop control strategies for the Anatomically Correct Testbed (ACT) hand with the ultimate goal of achieving fine object manipulation capabilities with the human-like musculoskeletal structure of the ACT hand. First, models of the kinematic and mechanical transformations between the hand's muscles, joints, and end-tips are generated using motion capture analysis and robotic modeling techniques. Because all sensory data in the ACT hand is currently limited to proprioceptive feedback in the form of muscle forces and positions, internal models are utilized extensively during control. Then, custom IR-based tendon force sensors are designed for the ACT hand's muscle-tendon actuators. Using the tension sensors, actuator-level force feedback is implemented to significantly reduce undesirable nonlinearities and allow precise muscle force regulation.

I then develop and test control algorithms for the ACT fingers and thumb based on standard robotic hand controllers from literature. The most widely accepted control methodology for robotic hands is impedance control, because of its ability to simultaneously regulate finger positions and applied forces/torques while allowing stable and intuitive environmental interactions (Hogan, 1985). Previous ACT hand research has focused only upon *position* control to track trajectories in either muscle-space, joint-space (Deshpande et al., 2013a) or a reduced synergy-space (Rombokas

et al., 2011; Malhotra et al., 2012). However, these position control strategies are incapable of controlling the interaction forces and torques that are critical for stable grasping and manipulation. To begin, we develop and experimentally demonstrate Cartesian impedance control of the ACT index finger and thumb, using only proprioceptive feedback in the form of muscle force and position sensing. Then, a controller is designed to achieve two-fingered fine manipulation, a complex task requiring precise and robust coordination of the thumb and fingers. Experimental results demonstrate simultaneous control of the 3-D object position, orientation, and applied grasping forces.

4.1 Kinematic Modeling

4.1.1 ACT Hand Design Upgrades

The ACT hand is designed to faithfully replicate the human hand's joint structure, musculotendon routing, and inertial properties (see Figure 4.1). One difference is that the ACT index finger, the EDC and EI are combined into a single muscle-tendon unit, which we will hereby refer to as simply the EDC, because these two muscles have equivalent functions for single-finger control (Brand and Hollister, 1999). Also, while the ADP in the human thumb is commonly considered to consist of two separate muscle heads, the transverse and oblique heads, it is represented by only one muscle-tendon unit in the ACT thumb. Details of the ACT hand's mechanical structure can be found in the work of Deshpande et al. (2013b).

We have also made design modifications to the ACT hand since the most recently published version of Deshpande et al. (2013a). The finger extensor mechanism was previously held in place on the finger's dorsal surface with ligament-like connec-

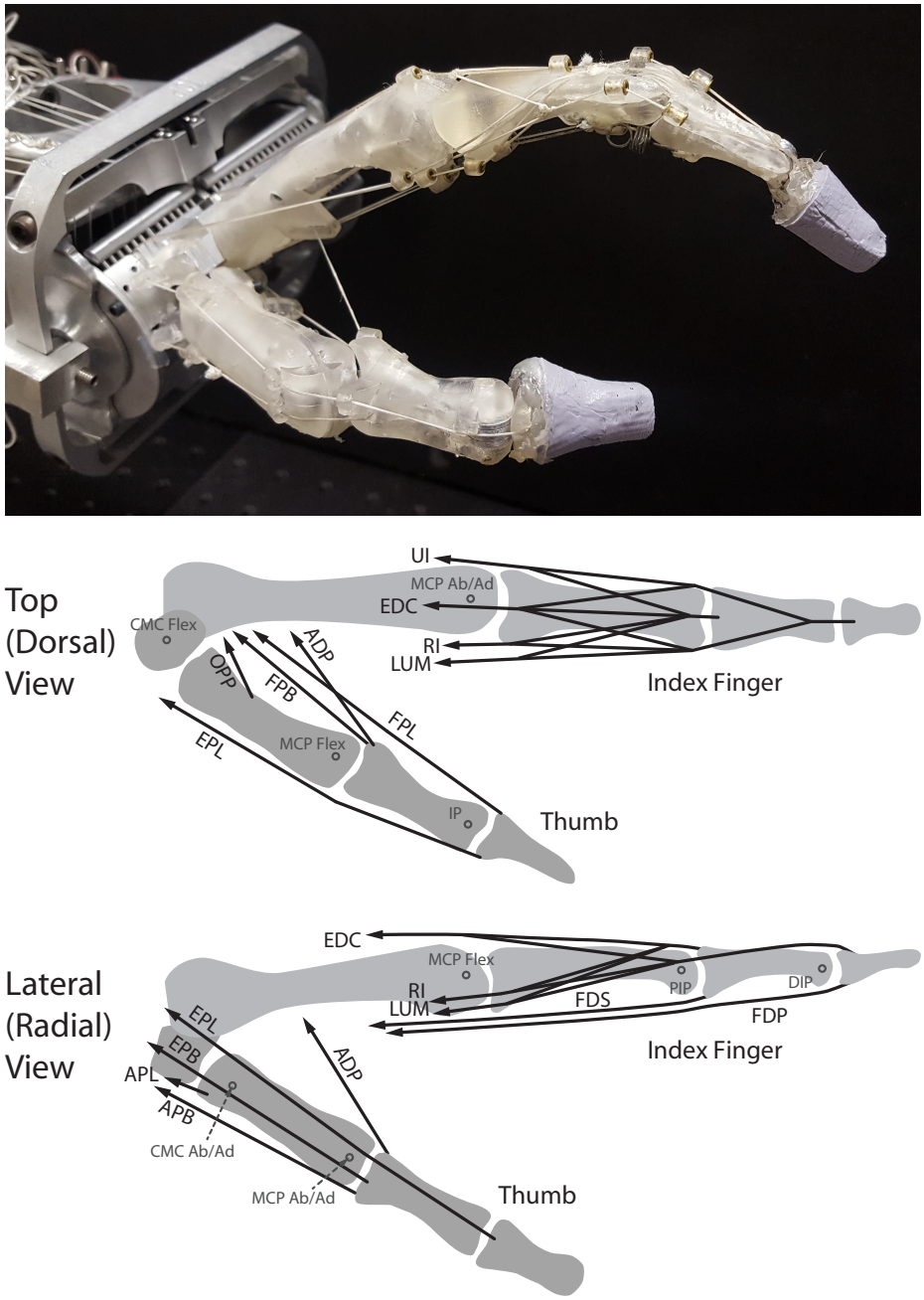

Figure 4.1: The index finger and thumb of the Anatomically Correct Testbed (ACT) hand, along with schematics of their tendon structure and approximate joint axis locations.

tions inserted into the metacarpal and proximal bones. This design led to anatomically inaccurate tension transfer through the extensor mechanism. The extensor mechanism displayed excessive lateral or medial shifting when forces were applied to the UI/LUM or RI, respectively, but if the ligaments were tightened, muscle forces in some cases transferred directly to ligament insertions instead of to the extensor slip and lateral bands. In the current version, the extensor mechanism is held in place using routing points near the MCP and PIP joints, facilitating the free transfer of tensions through the extensor mechanism while retaining anatomically accurate tendon moment arms. The tendon routing points of the ACT hand are designed to mimic human index finger moment arms (An et al., 1983; Fowler et al., 2001). Additionally, lateral band routing points across the PIP joint replicate the quantitative observations of Garcia-Elias et al. (1991a), such that the bands experience a palmar shift of 2 to 3 mm during PIP flexion.

Despite having anatomically accurate moment arms, we found that the PIP joint of the ACT index finger tended to become locked in a fully extended position. This occurs because the moment arms of all tendons crossing the PIP joint tend to move in the extension direction as the PIP is extended (Fowler et al., 2001), shifting the torque balance until no muscle force combinations can move the PIP joint back from a hyperextended position. This phenomenon is analogous to the swan-neck deformity observed in human fingers, which is known to occur if the PIP joint structures and ligaments that oppose PIP hyperextension are weakened, stretched, or destroyed (Dreyfus and Schnitzer, 1983). Based on this, we have added a ligament-like elastic element to the PIP joint in the form of a mechanical spring such that the finger moves out of the locked position when the muscle-tendon actuators are relaxed.

In the current version of the ACT thumb, the ADP and APB have been modified to insert directly to the base of the proximal phalanx, as opposed to joining the EPL in a dorsal expansion that acts as the extensor of the IP joint (Niehues and Deshpande, 2017; Deshpande et al., 2013b). This modification is based on anatomical research indicating that while the APB and ADP do have partial insertions into the dorsal insertion, they act primarily through their partial insertions directly into the base of the proximal phalanx, and in most cases IP extension is not a result of active pull of the APB or ADP through the dorsal expansion (Napier, 1952).

4.1.2 Muscle Moment Arms

The mechanical transformation between the muscles and joints of the hand can be defined through a posture-dependent muscle moment arm matrix $R(\boldsymbol{\theta})$, which relates muscle forces $\mathbf{f}_m$ to joint torques $\boldsymbol{\tau}$ through Eq. (2.1). In order to identify the joint-dependent moment arm functions of the ACT fingers and thumb, we use a methodology similar to that in Section 2.2.1.1, utilizing motion capture and actuator encoders to collect an extensive data set of joint angles and muscle lengths as the system is moved throughout its ROM.

Then, we utilize least squares regression (LSR) to fit second-order forward kinematic mapping functions without cross-joint terms, such that differentiation (see Eq. (2.14) will produce linear moment arm functions of the form $r_{ij}(\theta_i) = a_{ij}\theta_i + b_{ij}$ for every joint i and muscle j combination. This LSR fitting strategy was chosen for control because utilizing more complex fitting strategies, such as the neural networks in Section 2.2.1.1 or higher-order LSR, tends to result in unrealistic moment arm values, particularly near joint limits, due to inherent differentiation issues. We will show that the linear moment arm functions from a second-order LSR fit are sufficiently

accurate for control of ACT hand joint torques, and have the advantage of more predictable moment arm estimates throughout the ACT hand's ROM to ensure safe control in all scenarios.

4.1.3 Joint Posture Estimation

The current version of the ACT hand is limited to proprioceptive position sensing in the form of muscle lengths, and thus joint posture must be estimated through an inverse muscle mapping. For this, we used the same motion data set to train a feedforward neural network with muscle excursions as input and joint angles as output using the MATLAB Neural Network Toolbox (Mathworks Inc.). Because a gradient calculation is not necessary as it is for moment arm identification, we can use a neural network for more accurate joint angle estimates without encountering numerical differentiation issues.

The tendon compliance introduced by the deformable beam of the tension sensors lead to inaccurate joint angle estimation when large muscle forces are being applied. To account for this, we experimentally calculate the stiffness $k_{t,i}$ of tension sensor for muscle i by locking the fingers in place, ramping up commanded motor forces, and recording the change in linear actuator position using the motor encoders. We can then compensate for the deflection $\Delta\ell_{m,i} = f_{m,i}/k_{t,i}$ using IR tension sensor measurements. Utilizing tension sensor measurements for joint estimation makes the control law non-passive (Wimböck et al., 2008), such that control gains must be carefully chosen to ensure stability. However, the significant increase we gain in pose estimation accuracy is crucial for performing precision tasks such as fine manipulation.

4.1.4 Joint to Fingertip Modeling

The kinematic relationships between the ACT hand's joints and fingertips are obtained analytically, using the serial chain kinematic models that can be found in Appendix A. In the fingers, the four joint DOFs can be transformed into four Cartesian DOFs, represented by three fingertip translational DOFs ($\mathbf{x} \in \mathbb{R}^3$) and one rotational DOF of the distal phalanx ($\boldsymbol{\phi}_{dist} \in \mathbb{R}^1$). For the thumb, the additional joint DOF results in a second distal phalanx rotational DOF, such that $\boldsymbol{\phi}_{dist} \in \mathbb{R}^2$. Using the serial chain models, we determine the forward joint kinematics $\mathbf{x}(\boldsymbol{\theta})$ and $\boldsymbol{\phi}_{dist}(\boldsymbol{\theta})$ relating joint angles to Cartesian end-tip position and orientation. Then, the Jacobian matrix for a given ACT finger/thumb is found through differentiation:

$$J(\boldsymbol{\theta}) = \begin{bmatrix} J_x(\boldsymbol{\theta}) \\ J_\phi(\boldsymbol{\theta}) \end{bmatrix} = \begin{bmatrix} \frac{\partial \mathbf{x}(\boldsymbol{\theta})}{\partial \boldsymbol{\theta}} \\ \frac{\partial \boldsymbol{\phi}_{dist}(\boldsymbol{\theta})}{\partial \boldsymbol{\theta}} \end{bmatrix} \tag{4.1}$$

The Jacobian matrix relates joint torques $\boldsymbol{\tau}$ to the end-tip Cartesian force vector $\mathbf{f}_x$ and distal phalanx torque $\boldsymbol{\tau}_{dist}$ as follows:

$$\boldsymbol{\tau} = J^T(\boldsymbol{\theta}) \begin{bmatrix} \mathbf{f}_x \\ \boldsymbol{\tau}_{dist} \end{bmatrix} \tag{4.2}$$

With the presented joint posture estimation, Jacobian, and moment arm matrix functions, the force/torque transformations between muscle-, joint-, and Cartesian-space are fully defined through Equations (2.1) and (4.2).

4.2 ACT Hand Control

In this section, we present control strategies for implementing actuator-level muscle force feedback, then develop joint- and endtip-space force and stiffness controllers for the ACT index finger and thumb. The developed end-tip control capa-

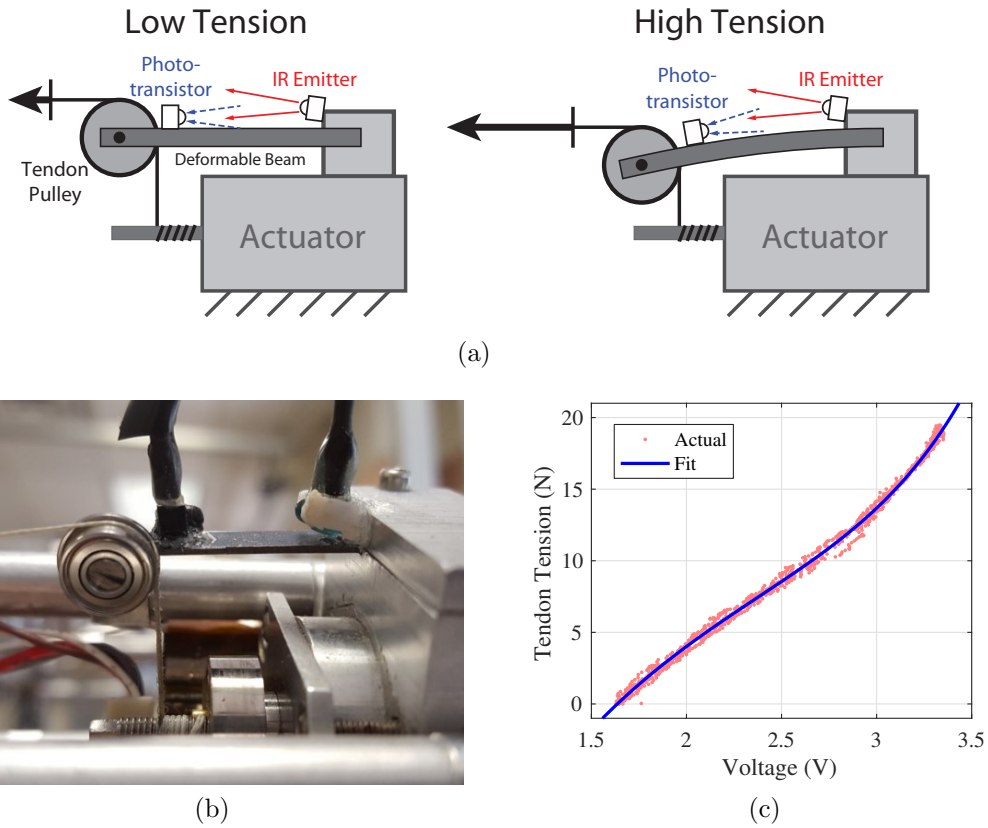

Figure 4.2: Custom tendon tension sensor based on an infrared (IR) emitter and phototransistor couple. (a) The operating principle of the IR tension sensor. As increasing levels of tension are applied, lower levels of IR light are received by the phototransistor. (b) Actual implementation with an ACT muscle-tendon actuator. (c) Example of the voltage to tension relationship exhibited by the sensor. The fitted curve is a double exponential function.

bilities are utilized to perform two-fingered fine object manipulation with the ACT hand.

4.2.1 Muscle Force Control

In previous works, the forces applied by the ACT hand's direct-drive brushless DC muscle-tendon actuators were regulated through motor current control. However, undesirable actuator nonlinearities such as friction and cogging leads to jerky finger

motions and significantly deteriorates the fine force control capabilities of the ACT hand. Thus, we designed custom IR-based force sensors, based on the concept introduced by Palli and Pirozzi (2011), to provide a direct measurement of tendon tension (Figure 4.2), similar to Golgi tendon organs in humans (Jami, 1992). Actuator proportional-integral (PI) feedback force controllers update the force commands $\mathbf{f}_{com}$ based on the error $\Delta f_m = f_{des} - f_m$ between measured force f_m and desired force f_{des}.

$$\mathbf{f}_{com} = \mathbf{f}_{des} + K_p \Delta \mathbf{f}_m + K_I \int \Delta \mathbf{f}_m dt - K_d \dot{\boldsymbol{\ell}}_m \tag{4.3}$$

where K_p and K_I are the PI gains and K_d is a motor damping gain for improved stability. Commanded forces $\mathbf{f}_{com}$ are transformed using motor torque constants and pulley radii into actuator current commands and sent to a low-level current controller.

We experimentally compare actuator force control performance with tension feedback ($K_p = 0.1$, $K_I = 20\ s^{-1}$) and without tension feedback ($K_p = K_I = 0$) in Figure 4.3. Without force feedback, the tendon force can vary by approximately ± 1 N from desired values, and significant Coulomb friction can be observed when positional displacements are applied to the tendon (see the intervals $t \in [7, 9]$ and $t \in [12, 14]$ seconds in Figure 4.3). The addition of force feedback compensates for these undesirable nonlinearities and greatly improves the precision of applied muscle forces, and even allows the precise application of low tensions (as low as 0.5 N) without the occurrence of tendon slacking. The ability to apply low tensions is crucial to minimize tendon sliding friction and facilitate smooth relaxation of antagonistic tendons.

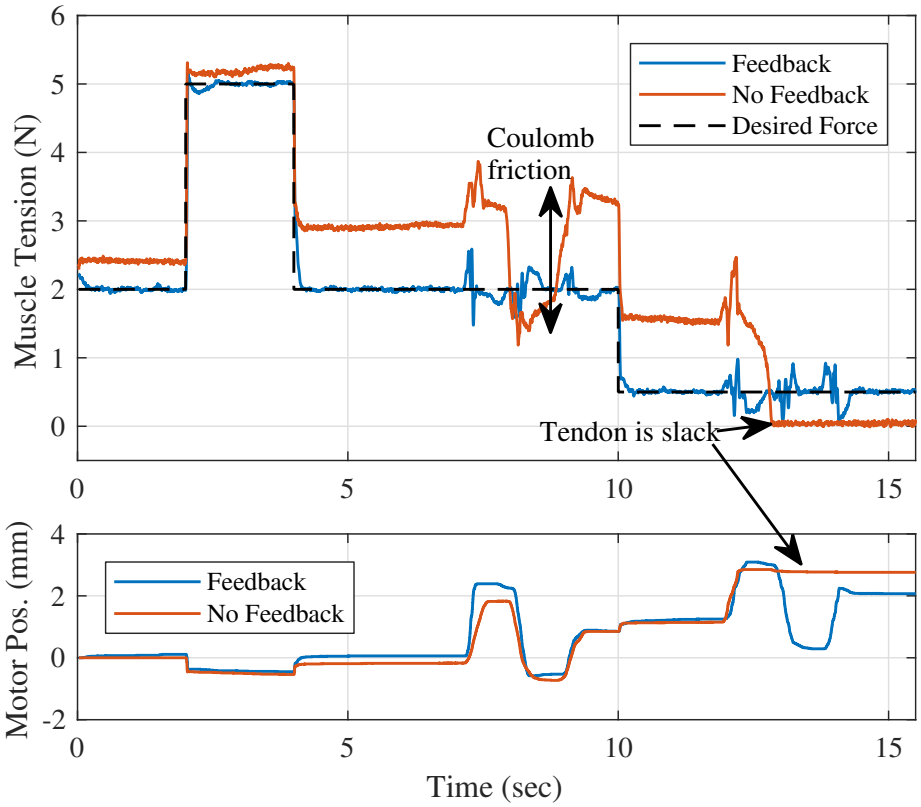

Figure 4.3: Comparison of actuator force control capabilities with and without the tension feedback control law in Equation (4.3).

4.2.2 Index Finger Control

In this section, we develop and test joint- and Cartesian-level control strategies for the ACT index finger. We first design a joint torque control algorithm to independently regulate the torques applied by the muscle-tendon actuators at the three controllable finger joints: MCP ab/ad, MCP flex, and PIP. We utilize the joint torque controller to develop a Cartesian control law for regulating the fingertip force vector produced by muscle inputs. We then develop joint-space and Cartesian-space stiffness controllers, with limited integral action to overcome friction, and demonstrate accurate trajectory tracking in either joint-space and Cartesian-space. Finally, we

show that the DIP joint, while not independently controllable, can still be partially regulated as a secondary control objective through proper force distribution between the two flexor muscles.

4.2.2.1 Joint Torque Control

For the ACT index finger, our goal is to control the MCP ab/ad, MCP flex, and PIP joint torques. The DIP joint torque will not be explicitly controlled, although the DIP angle will still be observed for inclusion in the kinematic model. In order to achieve some desired joint torques $\boldsymbol{\tau}_{des}$ through control of the muscle-tendon actuator forces $\mathbf{f}_m$, we form the following optimization problem:

$$\begin{aligned} \underset{\mathbf{f}_m,\alpha}{\text{minimize}} \quad & \mathbf{f}_m^T\mathbf{f}_m + \gamma(1-\alpha)^2 \\ \text{subject to} \quad & \alpha\boldsymbol{\tau}_{des} = R(\boldsymbol{\theta})\mathbf{f}_m \ , \ 0 < \alpha \leq 1 \\ & f_{min} \leq f_{m,i} \leq f_{max} \ , \ i = 1, \ldots, n_m \end{aligned} \tag{4.4}$$

Here, f_{min} and f_{max} are the minimum and maximum allowable tendon forces, n_m is the number of muscle-tendon actuators, α is a torque scaling term such that directionality is preserved when actuator saturation occurs, and γ is a large gain. Note that the torque constraint in this optimization does not include a row corresponding to the DIP joint.

4.2.2.2 Joint Stiffness Control

Next, we develop a joint stiffness controller to allow simultaneous control of the positions and torques at the controllable MCP ab/ad, MCP flex, and PIP joints through an intuitive spring-like impedance relationship:

$$\boldsymbol{\tau}_{des} = K_\theta(\boldsymbol{\theta}_{des} - \boldsymbol{\theta}) \tag{4.5}$$

where K_θ is the user-defined desired joint stiffness matrix, $\boldsymbol{\theta}_{des}$ is a desired joint trajectory, and current joint angles $\boldsymbol{\theta}$ are calculated using the joint estimation neural network. Because tension sensor compliance degrades the accuracy of a transformation from muscle to joint velocity, control damping is only applied directly to actuator velocities as in Equation (4.3),

Although muscle force feedback has eliminated undesirable actuator friction and cogging nonlinearities, there still exists some friction at the ACT hand's joints and tendon routing points that degrades trajectory tracking performance. To compensate, we add a limited amount of integral action to the control law, such that

$$\boldsymbol{\tau}_{des} = K_\theta(\boldsymbol{\theta}_{des} - \boldsymbol{\theta}) + K_{\theta,I} \int (\boldsymbol{\theta}_{des} - \boldsymbol{\theta}) dt \tag{4.6}$$

where $K_{\theta,I}$ is the integral gain matrix. In order to maintain a primarily impedance-like behavior, the integral terms were limited to magnitudes of 0.05 N·m.

The experimental results in Figure 4.4 demonstrate the effectiveness of the above joint stiffness controller for achieving independent joint control of the ACT index finger. Control of the MCP ab/ad and MCP flex joints has been demonstrated previously with the ACT hand (Deshpande et al., 2013a), but independent PIP joint control was previously not feasible because of inaccurate muscle force inputs and high levels of friction. The addition of tension feedback to the muscle-tendon actuators greatly reduces the negative effects of these key problems.

4.2.2.3 Cartesian Fingertip Force Control

Fine manipulation requires control of the forces being produced at the fingertips. Since DIP joint torque is not currently being explicitly controlled, we cannot independently control the corresponding distal phalanx torque τ_{dist} Cartesian DOF.

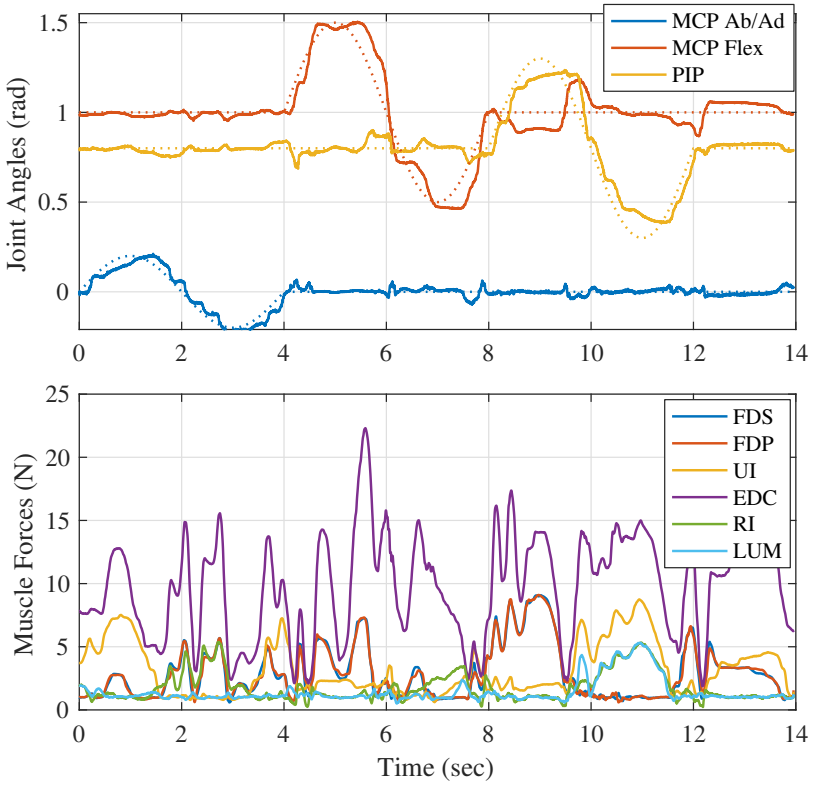

Figure 4.4: Index finger joint stiffness control experimental results. *Top:* Actual joint angle estimates (solid lines) and desired trajectories (dotted lines) for the task of independently moving each controllable joint through its range of motion at 1/4 Hz. *Bottom:* Corresponding muscle force patterns, which illustrate the following relationships between the muscles and joints of the human finger: (i) MCP ab/ad motions are generated by the intrinsic muscles (UI, RI, and LUM), (ii) MCP flex motions are generated primarily by the flexor (FDS and FDP) and extensor (EDC) muscles, and (iii) co-activation of the EDC with either the flexors or the intrinsic muscles generates PIP flexion or extension, respectively.

Thus, in this work we assume zero distal phalanx torque is being applied to the fingertip, e.g. hard point contact. Then, in order to produce a desired endtip force vector $\mathbf{f}_{x,des}$, we use in Equation (4.2) with $\tau_{dist} = 0$ to calculate the desired joint torques $\boldsymbol{\tau}_{des}$ at the three controllable joints, which would then be sent to the joint torque controller in Equation (4.4) to calculate muscle force commands.

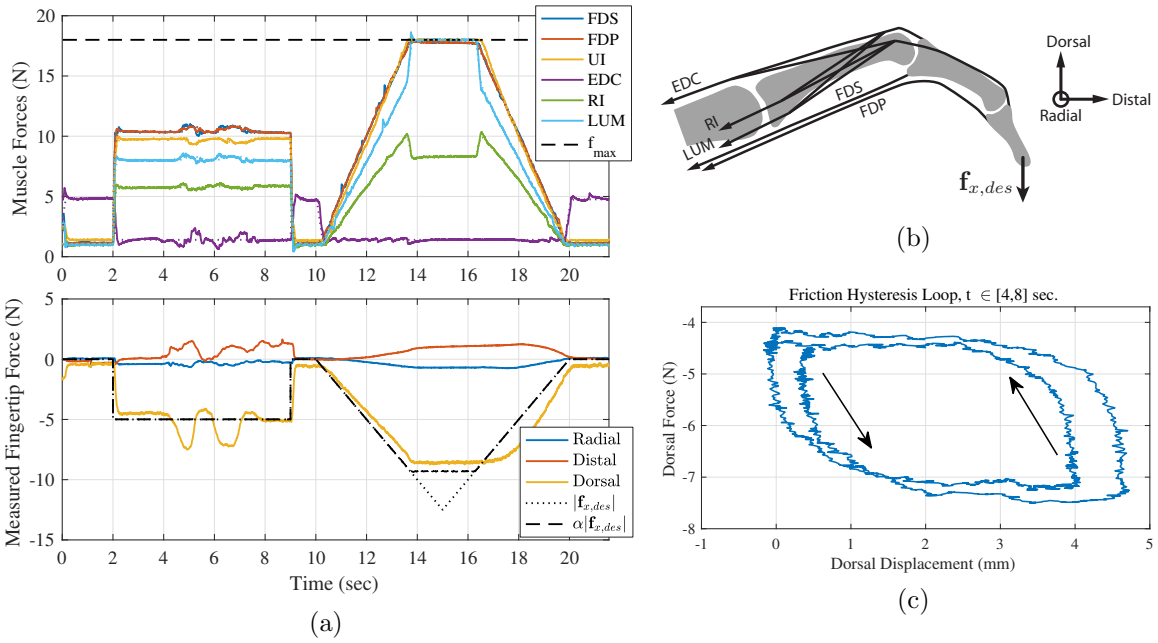

Figure 4.5: Index finger Cartesian force control for the task of producing fingertip force of varying magnitude in the palmar direction. (a) Applied muscle forces and endtip force measurements, taken from a 6-DOF force/torque sensor attached to the fingertip, for the task of tracking the palmar force trajectory denoted by the black dotted line. From $t \in [14, 16]$ sec., the muscles reach their maximum force limit $f_{max} = 18N$, so $\mathbf{f}_{x,des}$ is scaled via the α parameter through Equation (4.4) such that muscle forces stay within $[f_{min}, f_{max}]$ while preserving force directionality (black dashed line). (b) Approximate finger posture and direction of desired fingertip force. (c) From $t \in [4, 8]$ seconds, small applied fingertip perturbations in the palmar/dorsal directions produce a frictional hysteresis loop, demonstrating the level of friction (primarily Coulomb friction) remaining on the joint-side.

We implemented this Cartesian force control strategy in the ACT index finger, and performed experiments to test static fingertip force production. Fingertip force vectors were measured using a multi-axis force/torque sensor (F/T Nano25 SI-250-6, ATI Industrial Automation, Garner, NC). The results in Figure 4.5 demonstrate accurate tracking of a desired endtip force trajectory. Coulomb friction exists on the joint-side, as seen when perturbations are applied at $t \in [4, 8]$, due primarily to

tendon sliding friction (Figure 4.5c). As desired force is increased past the maximum force production capabilities of the actuators (see $t \in [14, 16]$ in Figure 4.5a), the optimization in Equation (4.4) scales down the produced endtip force vector to preserve force directionality.

4.2.2.4 Conditional Controllability of DIP Joint

Thus far, we have operated under the assumption that the tendon structure of the human finger is such that the DIP is not independently controllable. We verify this assumption by analyzing the ACT index finger moment arms with the controllability conditions outlined by Kobayashi et al. (1998). However, it is also true that in scenarios where the flexor muscles are being activated, e.g. when applying a grasp force, it is possible to manipulate the torque at the DIP joint, to a certain degree, without affecting the torques applied to the other joints by modulating the relative activations of the FDP and FDS.

To accomplish this, we will add an additional step to the muscle force optimization from Equation (4.4). Given a user input $\Delta\tau_{DIP}$ term defining the amount of DIP torque to be added to an initial muscle force solution $\mathbf{f}_m$ and assuming the FDP and FDS have approximately equivalent moment arms at the MCP/PIP joints, we adjust the flexor forces from the initial values, f_{FDP} and f_{FDS}, to modified values, $\bar{f}_{FDP}$ and $\bar{f}_{FDS}$, as follows:

$$\begin{aligned} \bar{f}_{FDP} &= f_{FDP} + \beta \frac{\Delta\tau_{DIP}}{r_{DIP}} \\ \bar{f}_{FDS} &= f_{FDS} - \beta \frac{\Delta\tau_{DIP}}{r_{DIP}} \end{aligned} \tag{4.7}$$

where r_{DIP} is the DIP moment arm of the FDP tendon. The scaling term β is defined to be the maximum value within the range $[0, 1]$ such that Equation (4.7) satisfies the

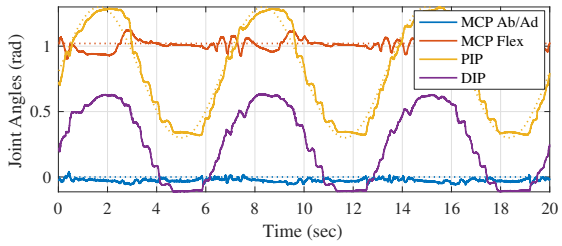

(a) $\Delta\tau_{DIP} \gg 0$

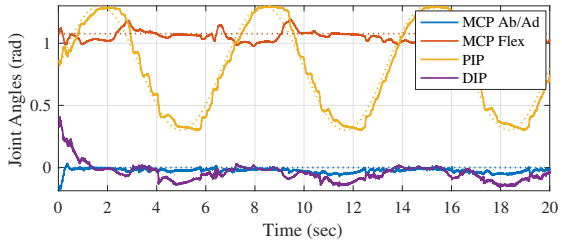

(b) $\Delta\tau_{DIP} \ll 0$

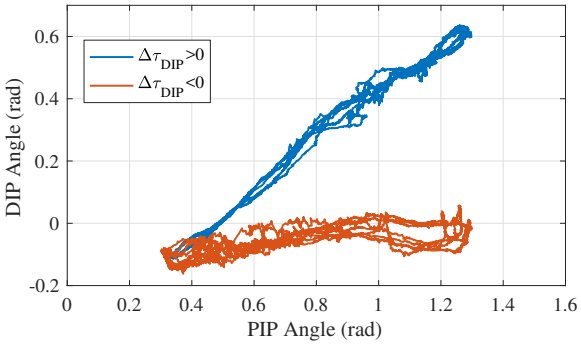

(c) Relationship between PIP and DIP joints

Figure 4.6: Experiments for PIP joint flexion and extension with differing values of the secondary DIP torque control parameter $\Delta\tau_{DIP}$. (a) If $\Delta\tau_{DIP}$ is set to be a large flexion torque, the FDP muscle is more active than the FDS. As a result, the extensor mechanism's lateral bands to remain taut, causing the DIP to flex with the PIP in a coupled curling motion. (b) If $\Delta\tau_{DIP}$ is set to be a large extension torque, the FDS muscle is more active than the FDP. In the absence of flexion torque from the FDP, the DIP joint moves to full extension and remains there. (c) The relationship between PIP and DIP joint motions depends on the relative FDP and FDS activation levels, which can be regulated through the secondary DIP joint controller.

muscle force constraints $\bar{f}_{FDP} \in [f_{min}, f_{max}]$ and $\bar{f}_{FDS} \in [f_{min}, f_{max}]$. In this way, the DIP joint torque is altered as a secondary task without affecting the primary task of producing torques at the other three joints.

The experimental results in Figure 4.6 demonstrate the effects of secondary DIP control during free motion. In human fingers, the DIP joint commonly moves in motions kinematically coupled with the PIP joint, but humans are also able to flex the PIP joint without flexing the DIP by activating only the FDS muscle (Leijnse et al., 2010). With the secondary control law, the DIP of the ACT index finger exhibits a

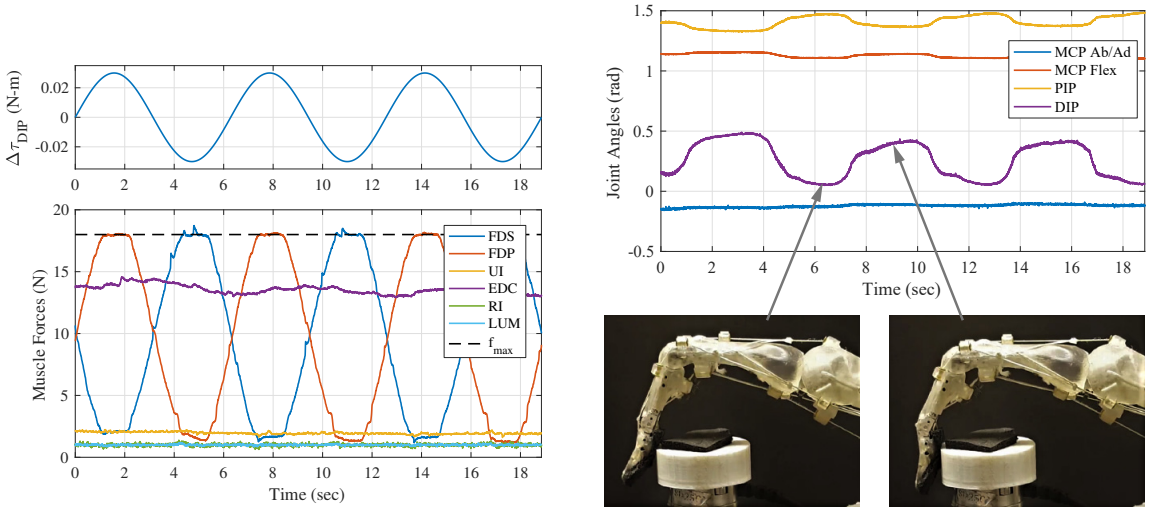

(a) (b)

Figure 4.7: Task demonstrating partial controllability of the index finger DIP joint. (a) Given the primary task of producing a constant endtip force of 3 N in the proximal direction, an additional DIP joint torque $\Delta\tau_{DIP}$ is applied as a secondary task (top). The activations of the FDS and FDP are adjusted based on $\Delta\tau_{DIP}$ through Equation (4.7), but are not allowed to pass outside the range $[f_{min}, f_{max}] = [1, 18]$ N (bottom). (b) Because the finger is making hard point contact, i.e. the distal phalanx angle is not constrained, changes in DIP torque results in corresponding changes to DIP joint angle. When $\Delta\tau_{DIP} < 0$, the DIP joint becomes fully extended (left photo). When $\Delta\tau_{DIP} > 0$, the DIP flexes until the lateral bands of the extensor mechanism becomes taut, such that the PIP and DIP joints are in a coupled posture (right photo).

level of DIP joint controllability in free motion that is consistent with human anatomy.

Next, we demonstrate a more direct control of the DIP joint during static force production (Figure 4.7). By varying the control input parameter $\Delta\tau_{DIP}$, the DIP joint angle can be partially regulated. This capability is important for grasping and manipulation, because it allows adjustment of distal phalanx angle to maximize contact with the flat pad of the finger for improved grasp stability.

4.2.2.5 End-tip Cartesian Stiffness Control

We then extended the joint-space controller in Equation (4.6) to Cartesian-space as follows:

$$f_{x,des} = K_x(\mathbf{x}_{des} - \mathbf{x}) + K_{x,I} \int (\mathbf{x}_{des} - \mathbf{x})dt \tag{4.8}$$

where K_x is the user-defined desired Cartesian stiffness matrix, $K_{x,I}$ is the integral gain matrix, $\mathbf{x}_{des}$ is a desired Cartesian trajectory, and current end-tip position $\mathbf{x}$ is calculated using the joint estimation neural network and the forward joint kinematics. To maintain a primarily impedance-like behavior, the integral terms were saturated to a magnitude no greater than 1 N in each direction.

Experimental results in Figure 4.8 show the index finger tracking a prescribed Cartesian trajectory with a Cartesian stiffness of $K_p = 0.2\ \frac{N}{mm}$ in all directions. For clarity, we present only motions in the sagittal plane; the finger commonly passes through a singularity position when the fingertip becomes aligned with the MCP ab/ad axis, causing a loss of controllability in the radial direction.

4.2.3 Thumb Cartesian Control

For the thumb, we will control the joint torques applied to four of the thumb joints: CMC flex, CMC ab/ad, MCP flex, and IP. The MCP ab/ad joint is not independently controllable, and thus is only passively observed for use in the Cartesian model. Given a set of desired joint torques $\boldsymbol{\tau}_{des}$, joint torque control is achieved using the same algorithm in Equation (4.4) that was used for the index finger.

Initially, we designed a controller to regulate four Cartesian DOFs, consisting of thumb-tip 3-D force $\mathbf{f}_x$ and distal phalanx torque τ_{dist}, using the aforementioned

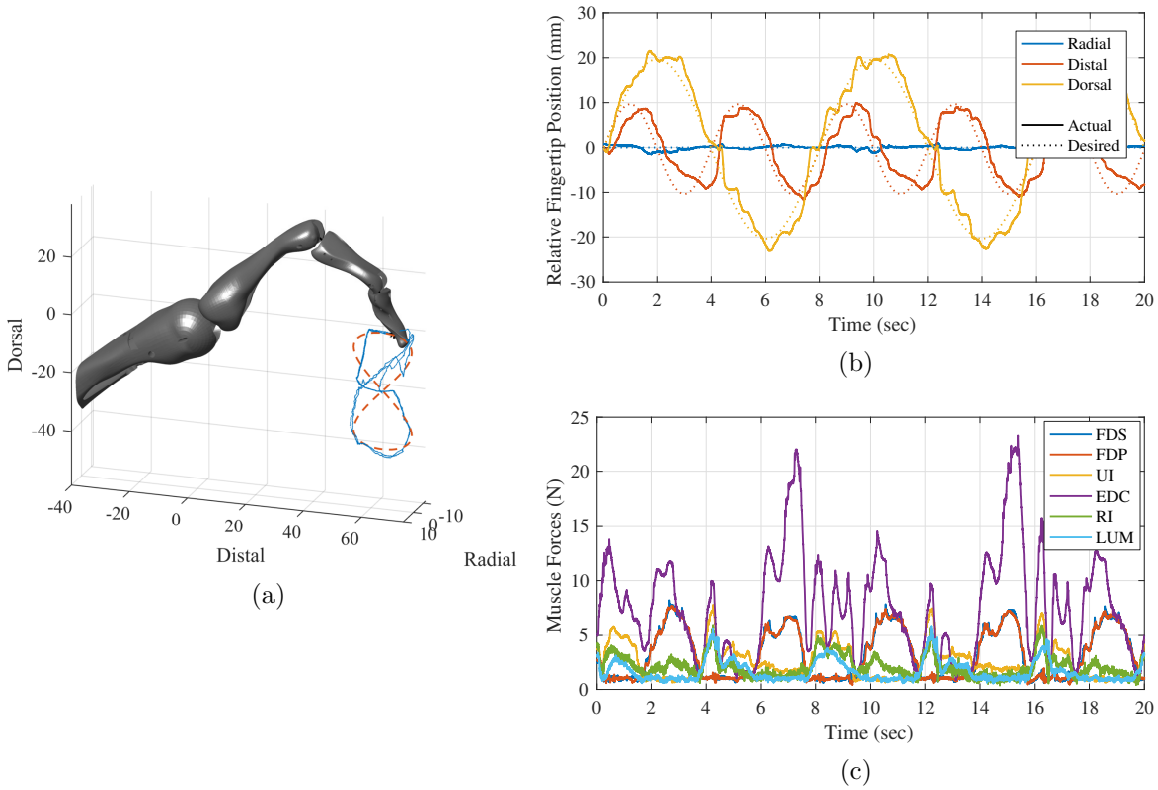

Figure 4.8: Cartesian control of the ACT index finger. (a)-(b) The desired trajectory (dashed/dotted lines) and actual trajectory (solid lines) for the task of tracing the prescribed shape with the fingertip in the sagittal plane. (c) Applied index finger muscle forces.

four controllable thumb joints through Equation (4.2). However, preliminary experiments showed that the thumb muscle moment arms are such that independent control of four thumb DOFs requires high levels of muscle co-contraction, resulting in frequent actuator saturation and poor system performance.

Intuitively, this occurs because the multi-articular tendon routing and moment arms of the human thumb make independent movement of the MCP flex joint a challenging task. In humans, it has been shown that thumb MCP flexion tends to be coupled with flexion of the CMC and IP joints (Li and Tang, 2007), indicating to

us that attempting to independently control the three flexion joints might be overly constraining the problem. The primary flexors of the MCP joint, the FPL, FPB, and ADP, are also major flexors of the other two thumb flexion/extension joints, such that independent MCP flexion requires large levels of antagonistic forces from extensor muscles.

To improve performance, the number of constraints in the control optimization is reduced from four to three by eliminating the constraint corresponding to distal phalanx torque production τ_{dist}, so that the controller is only constrained to achieve a desired 3-D thumb-tip force vector $\mathbf{f}_{x,des}$. To achieve this, the torque control optimization of Equation (4.4) is reformulated into a Cartesian force optimization as:

$$\begin{aligned} \underset{\mathbf{f}_m,\alpha}{\text{minimize}} \quad & \mathbf{f}_m^T\mathbf{f}_m + \gamma(1-\alpha)^2 \\ \text{subject to} \quad & \alpha\mathbf{f}_{x,des} = [J^{-T}(\boldsymbol{\theta})]_x R(\boldsymbol{\theta})\mathbf{f}_m \ , \ 0 < \alpha \leq 1 \\ & f_{min} \leq f_{m,i} \leq f_{max} \ , \ i = 1, \ldots, n_m \end{aligned} \tag{4.9}$$

where $J^{-T}(\boldsymbol{\theta}) \in \mathbb{R}^{4\times4}$ is the inverse transpose of the reduced thumb Jacobian, for which the rows and columns associated with the uncontrollable MCP ab/ad joint and corresponding end-tip torque are removed, and the term $[J^{-T}(\boldsymbol{\theta})]_x$ contains only the first three rows of $J^{-T}(\boldsymbol{\theta})$. In this way, muscle force magnitudes are reduced as much as possible while fulfilling the constraint of producing a desired 3-D thumb-tip force vector $\mathbf{f}_{x,des}$.

For experimental testing, we implemented a high-level thumb-tip Cartesian impedance controller with limited integral action similar to Equation (4.8) that was used for the index finger. Experimental results in Figure 4.9 show thumb-tip tracking with a Cartesian stiffness of $K_p = 0.2 \ \frac{N}{mm}$ in all directions. Results show accurate tracking in the radial and dorsal directions. The distal direction experiences higher

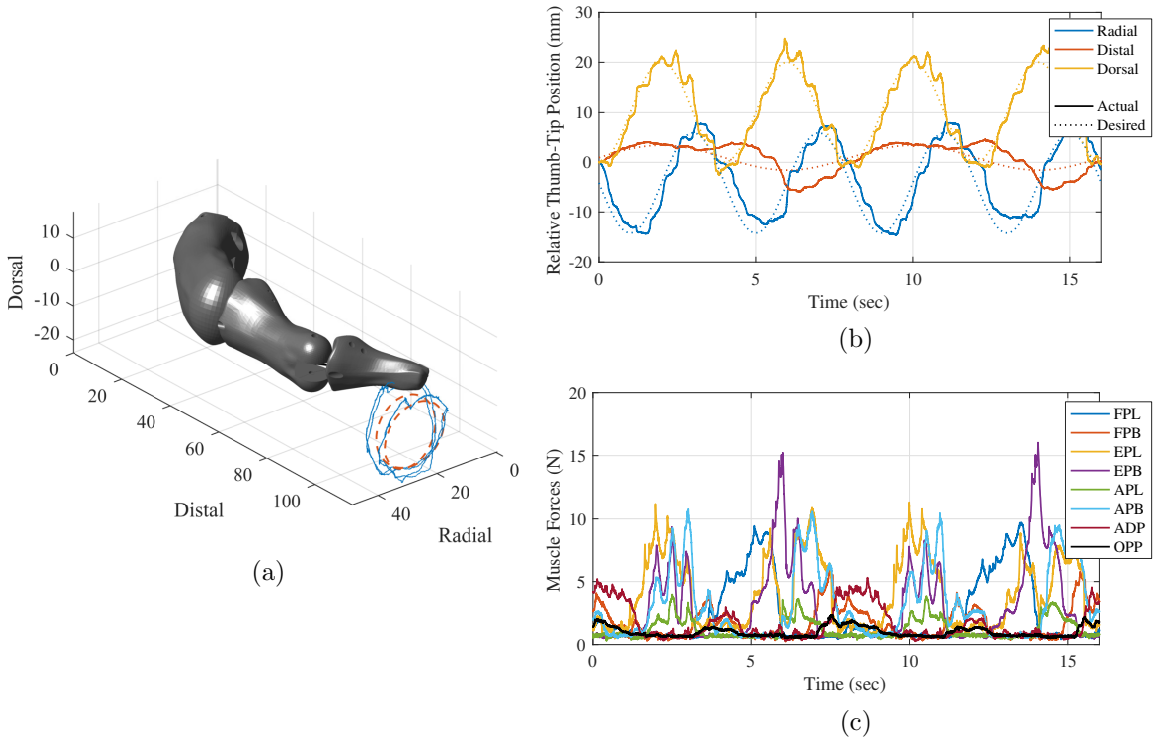

Figure 4.9: Cartesian control of the ACT thumb. (a)-(b) Desired trajectory (dashed/dotted lines) and actual trajectory (solid lines) for the task of tracking a prescribed thumb-tip sinusoidal trajectory in all three Cartesian directions. (c) Applied thumb muscle forces.

levels of friction because of how joint friction transforms to Cartesian space, and thus shows poorer tracking performance.

4.2.4 Fine Manipulation Control

To demonstrate the capabilities of the developed ACT thumb-tip and fingertip force controllers, we address the complex task of two-fingered fine object manipulation. Given the vector of end-tip Cartesian positions $\mathbf{x} = [\mathbf{x}_f, \mathbf{x}_t]^T$, where $\mathbf{x}_f$ and $\mathbf{x}_t$ correspond the index finger and thumb, respectively and global x-y-z coordinates represent the radial, distal, and dorsal directions, we define the vector between the

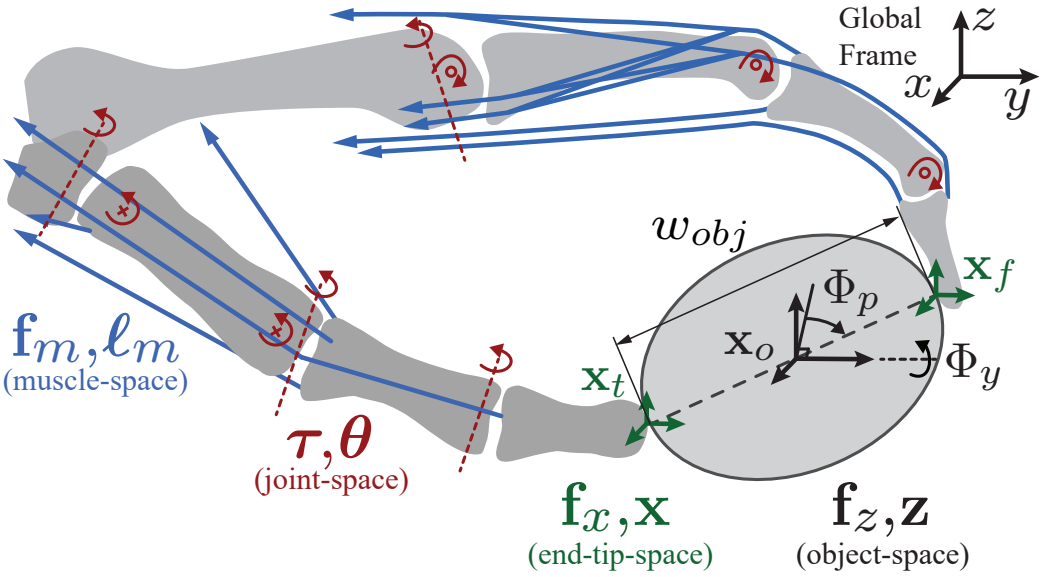

Figure 4.10: Schematic of coordinate frames, along with a visualization of defined object coordinates $\mathbf{z}$.

end-tips as $\mathbf{x}_{ft} = \mathbf{x}_f$ - $\mathbf{x}_t = [x_{ft,1}, x_{ft,2}, x_{ft,3}]^T$. Then, we can define a set of object-space coordinates z (see Figure 4.10 for schematic) as:

$$\mathbf{z} = \begin{bmatrix} \mathbf{x}_o \\ \Phi_y \\ \Phi_p \\ w_{obj} \end{bmatrix} = \begin{bmatrix} \frac{1}{2}[\mathbf{x}_f + \mathbf{x}_t] \\ \text{atan2}(x_{ft,3},\ -x_{ft,1}) \\ \text{atan2}(x_{ft,2},\ \sqrt{x_{ft,1}^2 + x_{ft,3}^2}) \\ ||\mathbf{x}_{ft}|| \end{bmatrix} \tag{4.10}$$

The translational object position $\mathbf{x}_o \in \mathbb{R}^3$ is the midpoint between the two end-tip positions. Object orientation is defined by yaw and pitch Euler angles, where yaw angle Φ_y is the rotation of $\mathbf{x}_{ft}$ about the global distal axis and pitch angle Φ_p is the angle between $\mathbf{x}_{ft}$ and the transverse x-z plane (see Figure 4.10). The object's third rotational degree of freedom (DOF) is about an axis aligned with $\mathbf{x}_{ft}$, which cannot be controlled in a two-fingered grasp, and is thus not included in our definition object-space coordinates. The final term is defined as object width w_{obj}, which will vary only if there exists a level of compliance between the contact points.

To determine the grasp matrix W, we derive an inverse object kinematics function $\mathbf{x}(\mathbf{z})$ that returns end-tip positions $\mathbf{x}$ as a function of object coordinates $\mathbf{z}$:

$$\mathbf{x}(\mathbf{z}) = \begin{bmatrix} \mathbf{x}_o + \frac{1}{2}\mathbf{x}_{ft}(\mathbf{z}) \\ \mathbf{x}_o - \frac{1}{2}\mathbf{x}_{ft}(\mathbf{z}) \end{bmatrix} \tag{4.11}$$

Here, the vector $\mathbf{x}_{ft}(\mathbf{z})$ is expressed in object coordinates:

$$\mathbf{x}_{ft}(\mathbf{z}) = w_{obj} \begin{bmatrix} -\cos(\Phi_y)\cos(\Phi_p) \\ \sin(\Phi_p) \\ \sin(\Phi_y)\cos(\Phi_p) \end{bmatrix} \tag{4.12}$$

Then, the grasp matrix W is found, based on the kinematic relationship of Equation (3.4), as:

$$W^T(\mathbf{z}) = \frac{\partial \mathbf{x}(\mathbf{z})}{\partial \mathbf{z}} \tag{4.13}$$

With this definition of $\mathbf{z}$ that includes internal force term, the internal grasp force f_{int} is inherently included as the last term of $\mathbf{f}_z$ and the last row of W in the end-tip-to object-space force relation of Equation (3.3). The full analytical representation of $W(\mathbf{z})$ can be found in Appendix B.1.

To manipulate object position/orientation within the hand, the object-level controller will produce an object-space force/torque based on object position/orientation error. Thus, we define an object-space PI controller as follows:

$$\mathbf{f}_z = \begin{bmatrix} \mathbf{f}_{xo} \\ \tau_y \\ \tau_p \\ f_{int} \end{bmatrix} = \begin{bmatrix} K_{obj} \begin{bmatrix} \mathbf{x}_{o,d} - \mathbf{x}_o \\ \Phi_{y,d} - \Phi_y \\ \Phi_{p,d} - \Phi_p \end{bmatrix} + K_{obj,I} \int \begin{bmatrix} \mathbf{x}_{o,d} - \mathbf{x}_o \\ \Phi_{y,d} - \Phi_y \\ \Phi_{p,d} - \Phi_p \end{bmatrix} dt \\ f_{int} \end{bmatrix} \tag{4.14}$$

where K_{obj} and $K_{obj,I}$ are object-space stiffness and integral gains. Note that f_{int} has not yet been determined, but will instead be calculated analytically in the next step.

For object-level control, Equation (3.3) is inverted:

$$\mathbf{f}_x = W^{-1}(\mathbf{z})\mathbf{f}_z \tag{4.15}$$

The grasp matrix W will always be invertible so long as $\mathbf{x}_{ft}$ does not coincide with the object yaw axis and $w_{obj} > 0$ (see Appendix B.1 for details). At this point, the parameter f_{int}, which regulates the amount of internal forces being applied along $\mathbf{x}_{ft}$, is determined analytically to produce a prescribed minimum normal force $f_{grip,min}$ at each contact point. The method for calculating f_{int} can be found in Appendix B.2. If contact slippage is expected, e.g. for low-friction objects, f_{int} could instead be calculated such that the contact force vectors fall within a friction cone (Kerr and Roth, 1986), but this more complex method is not implemented in this work. The resulting $\mathbf{f}_x$ from Equation (4.15) sent to the index and thumb Cartesian force controllers developed in the previous section.

Using this object-space control law, experimental results for two-fingered object manipulation are shown in Figure 4.11. The control gains (using units of N, mm, rad, and sec) are set to $K_{obj} = \text{diag}([0.1, 0.1, 0.1, 100, 150])$, $K_{obj,I} = \text{diag}([0.1, 0.1, 0.1, 400, 800])$, and $f_{grip,min} = 2$ N, with integral force and torque terms saturated at 1 N and 70 N·mm, respectively. The purpose of this experiment is to perform in-hand manipulation of the two controllable object orientation DOFs. The results show accurate tracking of the desired object yaw and pitch angles and relatively small deviations (< 8 mm) from the desired translational position (Figure 4.11a).

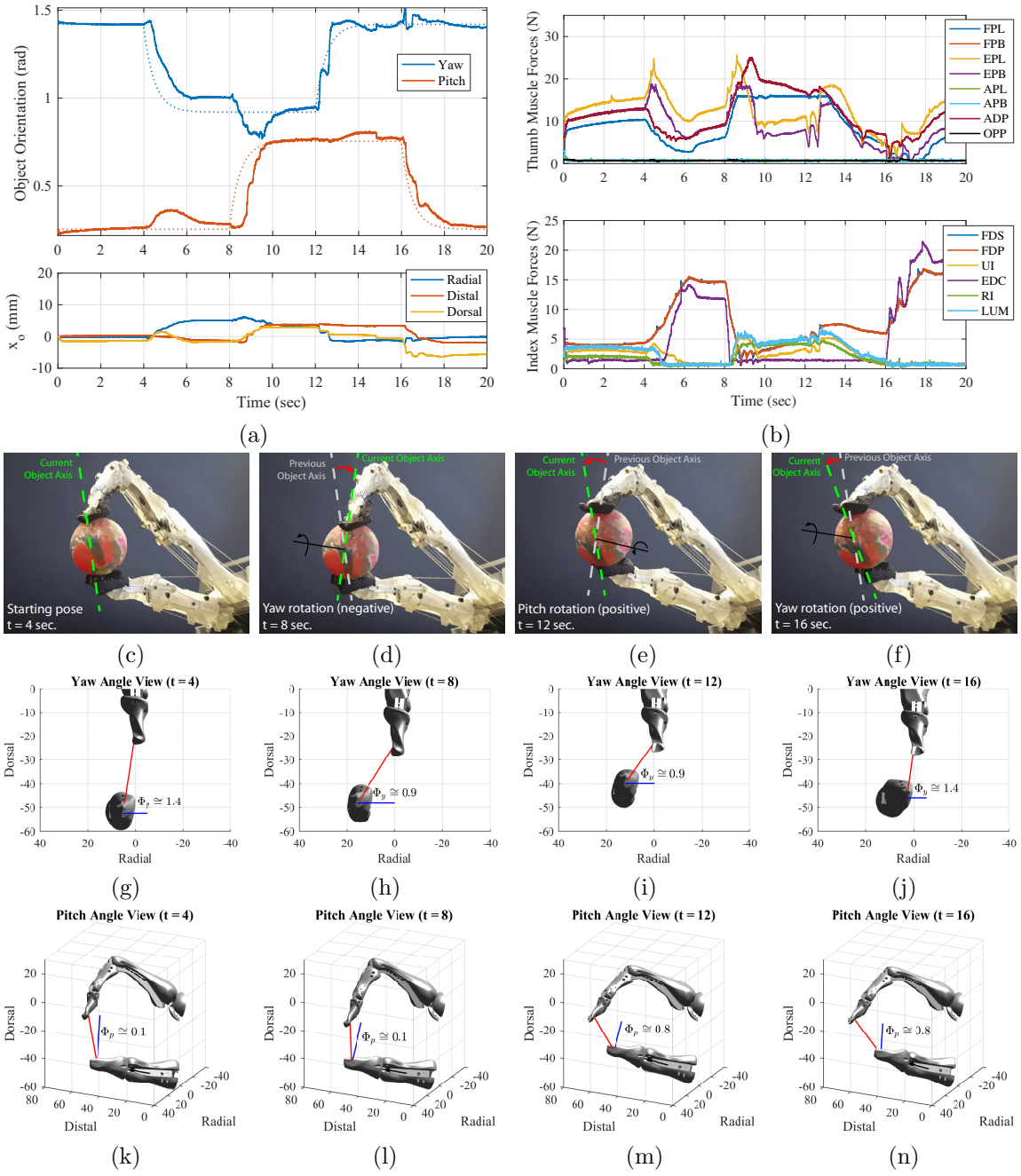

Figure 4.11: Two-fingered object manipulation with the ACT hand. (a) Object orientation and relative translation, actual (solid lines) and desired trajectories (dotted lines), for the task altering object orientation while maintaining 3-D position. (b) Thumb and index finger muscle forces. (c)-(f) Live snapshots at four times of interest: $t = 4$, 8, 12, and 16 seconds. (g)-(j) Visual recreations to show changes in object yaw angle. (k)-(n) Rotated viewpoints to show changes in object pitch angle.

4.3 Discussion

The novel contributions presented in this chapter are (i) the design of novel IR-based tension sensors for force feedback control of the ACT hand muscle-tendon actuators, (ii) the development of Cartesian control strategies for the human-like musculoskeletal structure of the ACT index finger and thumb using proprioceptive feedback, and (iii) the utilization of the developed endtip control capabilities to achieve two-fingered fine object manipulation. This work with the ACT hand provides insights into the unique functionality of the human musculoskeletal structure for achieving the tasks required of our hands during everyday tasks.

4.3.1 Tendon Structure and Joint Controllability

The human finger is not a fully controllable system, but this limitation does not hinder humans' fine manipulation capabilities. The DIP and PIP joints are passively coupled in human fingers, an important feature for shape adaptation and grasp closure during power grasps. This has inspired under-actuated robotic and prosthetic hands that provide robust grasping capabilities for various object sizes and shapes and uncertain environments, but which are generally not designed with fine manipulation as the primary goal (Dollar and Howe, 2010; Carrozza et al., 2004).

Conventional wisdom in robotic hand design dictates that for the task of fine manipulation, uncontrollable DOFs should be avoided to ensure that the finger's position and applied forces can be precisely regulated. Thus, anthropomorphic hands are commonly designed with controllable DIP joints, either through mechanical linkages that enforce a fixed relationship between the PIP and DIP joints (Bridgwater et al., 2012; Butterfaß et al., 2001; Liu et al., 2008) or by independently actuating the DIP

joint (Grebenstein et al., 2012).

Experiments with the ACT hand highlight the partially controllable nature of the DIP joint, particularly when the flexors are activated such as during manipulation tasks. As a result, the human finger is capable of functioning either as an under-actuated system during tasks like power grasping in which adaptability is useful, or as a fully actuated system during precise fine manipulation tasks. Future work with the ACT hand includes implementing DIP joint regulation during manipulation tasks as a secondary control objective, such that the contact surface on the finger pad can be adjusted for improved grasp stability.

4.3.2 Thumb Control Space

In the thumb, a tendon controllability analysis tells us that the thumb has four controllable joint DOFs. However, as discussed in Section 4.2.3, independently controlling all four joint DOFs, or equivalently the corresponding four Cartesian DOFs, is not ideal due to the high muscle activations required to produce even small magnitudes of joint torque. In this work, thumb control is demonstrated in a reduced subset defined by the three thumb-tip Cartesian DOFs. The choice to reduce the number of controlled DOFs from four to three is supported by the human thumb kinematic study of Li and Tang (2007), who found that during thumb opposition tasks, the CMC flex, MCP flex, and IP joints tend to move in a coupled manner, such that the functional DOFs of the thumb can be adequately represented by only three components. Potential future research could focus on utilizing the ACT thumb to develop a clearer understanding of the thumb control space that the human neuromuscular system might be acting within.

4.3.3 Functionality of Human Hand Structure for Coordinated Manipulation

Manipulation experiments with the ACT hand demonstrate the roles of the different digits, joints, and muscles in achieving various tasks. For example, when the index finger MCP is in a flexed position, lateral fingertip manipulability is reduced because the fingertip is near the yaw joint axis. In the human finger, lateral mobility is even further reduced due to tightening of the collateral ligaments (Sancho-Bru et al., 2001). Therefore, object rotation about the yaw axis, as defined in this work, during an opposition pinch grasp would be expected to be achieved primarily through thumb flexion/extension. This is confirmed when we analyze experimental ACT hand motions for an object yaw rotation (e.g. the negative rotation in Figures 4.11g-h and positive rotation in Figures 4.11i-j). Analogously, due to the relatively higher manipulability of the index finger in the distal direction compared to the thumb, changes in pitch angle are achieved primarily through index finger motions (see Figures 4.11l-m). Analysis of muscle forces gives insight into the critical roles that different muscles have in specific task scenarios. For the given fine manipulation task, only four thumb muscles (FPL, EPL, EPB, and ADP) are utilized to produce a thumb opposition force, while in the index finger the flexor muscles are constantly active to produce grasping force and the relative activations of all six muscles vary depending on the direction of desired fingertip force.

There exist a few limitations to how far our results with the ACT hand can be applied to studying human biomechanics. While the mechanical joint and tendon structure is replicated closely, the viscoelastic properties, extremely low levels of joint and tendon friction, and tactile sensing capabilities of human hands are difficult to duplicate in a robotic system. Nonetheless, performing complex manipulation tasks

with the ACT hand's human-like structure can potentially provide significant insights into the underlying mechanisms of human hand dexterity.

Our results demonstrate the effective implementation of object-level control strategies with the extremely complex and nonlinear transmission and actuation of the ACT hand. This work validates the effectiveness of existing robotic manipulation strategies for even highly complex tendon-driven systems, provided adequately accurate fine end-tip control capabilities and object models are available. It also shows the feasibility of utilizing only non-collocated musculotendon sensing to perform complex tasks in end-tip-space. The tight space constraints and robustness/safety requirements of robotic hands are such that confining the majority of sensitive electronics within the forearm is beneficial from a design standpoint (Grebenstein et al., 2012). With the resulting reduction in link-side sensory feedback, accurate internal models such as the ones presented in this work are required to allow accurate control capabilities in joint-, end-tip-, and object-space.

Chapter 5

Human-Inspired Control of the ACT Hand

As previously discussed, a common control strategy for dexterous manipulation is object-level impedance control, which allows intuitive control of the object's 3-D position and orientation, applied external forces/torques, and internal grasp forces (Schneider and Cannon, 1992). However, for robotic hands with intrinsically compliant designs, the range of achievable object-space stiffness gains for such a control strategy can be severely limited, reducing manipulation capabilities and performance. In order to achieve a specified object-space stiffness, the robotic system must be capable of emulating appropriate corresponding tendon-, joint-, or Cartesian-space stiffnesses through control (Cutkosky and Kao, 1989), but researchers have shown that the achievable stiffness of a robotic system is bounded based on its inherent passive stiffness (Rao et al., 2017; Albu-Schäffer et al., 2007). Thus, object stiffness gains can only be increased to certain levels before instability and grasp failures will occur. For example, in the ACT manipulation experiments of the previous chapter, limited stable object stiffness gains were unable to overcome friction, making significant integral control action necessary to produce acceptable tracking performance.

While designing robotic hand systems with higher intrinsic stiffness would mitigate this issue, there are crucial advantages offered by passive compliance that would be lost, such as increased robustness, safe environmental interactions, and improved fine force control capabilities. Similar advantages have been identified by the designers

of robotic hands such as the variable stiffness DLR Awiwi Hand (Grebenstein et al., 2012) and twisted-string actuated UB Hand IV (Melchiorri et al., 2013). Additionally, in systems with highly geared position-controlled actuators, such as Robonaut 2 (Niehues et al., 2014), or with tension sensors that operate based on load-based deflection (Palli and Pirozzi, 2011), a level of series elasticity is required to achieve fine force control.

By contrast, in human hands, the effective object-space stiffness during grasping arises almost entirely from the natural impedance-like behavior of muscles, which is exploited by the central nervous system (CNS) to allow for robust reactions to rapid disturbances (Burdet et al., 2001; Gribble et al., 1998). In this way, humans are able to perform dexterous manipulation despite significant feedback delays between the sensory organs, CNS, and muscles which would make pure feedback control infeasible (Morasso, 2011). This type of hierarchical control strategy seen in the human neuromuscular system might also be beneficial if implemented in robotic hands, helping to ensure grasp stability for a wide range of system parameters and manipulation task scenarios.

In this chapter, first the limitations on achievable object stiffness gains are analyzed as a function of robotic system design and manipulation task parameters for a two-fingered pinch grasp. Then, experimental testing is performed with the previously developed ACT hand object-space stiffness controller to demonstrate the stable object stiffness boundaries for various manipulation task scenarios.

Next, drawing inspiration from the human neuromuscular system, I develop a novel control strategy which implements low-level stiffness in *muscle-space* to ensure grasp stability, while a high-level controller gradually updates muscle resting

lengths to emulate an object-space stiffness in quasi-static conditions. Experimental results demonstrate the ability of this control strategy to significantly increase the quasi-static object-space stiffness of the system, leading to significantly improved manipulation capabilities in compliant robotic hand systems.

5.1 Stiffness Transformations

To begin, generalized equations are presented for transforming stiffness matrices between frames located in tendon-, joint-, end-tip-, and object-space for a tendon-driven robotic hand performing two-fingered grasping and manipulation (see Figure 4.10). The position and force/torque transformations between these spaces have been previously defined in Section 3.1.

For a single digit, the conservative congruence transformation of Chen and Kao (2000) is utilized to describe the stiffness transformations between tendon-, joint-, and end-tip-space as follows:

$$K_\theta = R(\boldsymbol{\theta}) K_m R^T(\boldsymbol{\theta}) + \left[\frac{\partial R(\boldsymbol{\theta})}{\partial \boldsymbol{\theta}} \mathbf{f}_m \right] \tag{5.1}$$

$$K_\theta = J^T(\boldsymbol{\theta}) K_x J(\boldsymbol{\theta}) + \left[\frac{\partial J^T(\boldsymbol{\theta})}{\partial \boldsymbol{\theta}} \mathbf{f}_x \right] \tag{5.2}$$

The above equations include not only the direct transformation of stiffness matrices, but also load-dependent terms associated with configuration-dependent geometry changes in $R(\boldsymbol{\theta})$ and $J(\boldsymbol{\theta})$.

Defining the object-space coordinates and grasp matrix as in Section 4.2.4 (see Figure 4.10 for schematic), the combined end-tip stiffness matrix K_x as a block diagonal matrix of index finger Cartesian end-tip stiffness $K_{x,f}$ and thumb-tip stiffness $K_{x,t}$, and object stiffness K_z through the relation $\mathbf{f}_z = K_z d\mathbf{z}$, the stiffness transformation

from end-tip-space to object-space is:

$$K_z = W(\mathbf{z})K_x W^T(\mathbf{z}) + \left[\frac{\partial W(\mathbf{z})}{\partial \mathbf{z}} W^{-1}(\mathbf{z})\mathbf{f}_z\right] \tag{5.3}$$

See Appendix B.3 for the complete analytical calculation of this equation.

5.1.1 Passivity Analysis

In order to ensure system passivity, it has been shown that the difference between passive and active stiffness must remain positive semi-definite (Rao et al., 2017). If this passivity condition holds, then by definition the actuators will tend to dissipate energy, and system stability can be guaranteed.

The joint-space passivity bound of Rao et al. (2017) can be also be transformed to object-space as:

$$K_{z,pass} - K_{z,d} \geq 0 \tag{5.4}$$

where $K_{z,pass}$ is the object-space passive stiffness, calculated from the system's passive compliance elements (e.g. tendon stiffness $K_{m,pass}$) and operating force/torque conditions using Equations (5.1), (5.2), and (5.3). This effectively places an upper bound on the active object stiffness $K_{z,d}$, e.g. for the object-space stiffness control law presented in the next section. If the passivity bound in Equation (5.4) is violated, the system becomes non-passive and potentially unstable.

The factors that determine the value of $K_{z,pass}$ can be separated into two categories: system parameters, determined by the robotic hand's design, and task parameters like object size/shape and grasp force.

5.1.1.1 Effect of Robotic Hand Design on Grasp Stability

The passive stiffness of the robotic system itself, represented by the effective end-tip stiffnesses $K_{x,pass}$ of each digit, is the most obvious contributor to $K_{z,pass}$, and should be considered a key design parameter when attempting to achieve a desired range of object stiffness gains $K_{z,d}$ for a set of grasping tasks. For each digit, $K_{x,pass}$ is a function of passive stiffness values (e.g. $K_{m,pass}$), joint structure ($J(\boldsymbol{\theta})$), tendon moment arms ($R(\boldsymbol{\theta})$), and loading conditions. Informed modifications to robotic hand design can alter $K_{z,pass}$ such that a specified range of $K_{z,d}$ satisfies Equation (5.4) for a given set of tasks.

However, major design modifications may be limited or infeasible for some systems. Joint structure, actuation, and transmission of robotic hands are usually specifically designed to fulfill tight space constraints while producing optimal grasping kinematics, force production capabilities, and dynamic properties, leaving little design freedom for modifications. In the special case of the ACT hand, alterations to joint structure or tendon moment arms are not possible without losing anatomical correctness, for which the testbed is specifically designed. Directly increasing the stiffness of elastic elements can also lead to undesirable consequences, such as poor impact robustness and high-frequency noise transmission, and a level of passive compliance is usually required for accurate force control, i.e. through force sensors or series elastic actuation. For these reasons, an upper bound exists on feasible system passive stiffness $K_{x,pass}$.

5.1.1.2 Effect of Task Parameters on Grasp Stability

Object manipulation task parameters, such as object width w_{obj} and grasp force f_{int}, also play a significant role in determining $K_{z,pass}$. Increasing w_{obj} leads to a corresponding increase in object rotational stiffness $k_{\Phi,pass}$ proportional to w_{obj}^2, because object width corresponds to the effective moment arm transforming from end-tip stiffness K_x to object-space rotational stiffness k_Φ.

The effect of grasp force f_{int} on $K_{z,pass}$ appears in the last term of Equation (5.3). Letting K_g represent the last term $\left[\frac{\partial W}{\partial \mathbf{z}} W^{-1}\mathbf{f}_z\right]$, all elements of K_g will be zero except the two diagonal elements k_{g,Φ_y} and k_{g,Φ_p} corresponding to rotational stiffnesses about Φ_y and Φ_p, respectively. Analytically, these two values are found to be:

$$\begin{aligned} k_{g,\Phi_y} &= -f_{int} w_{obj} \cos^2(\Phi_p) \\ k_{g,\Phi_p} &= -f_{int} w_{obj} \end{aligned} \tag{5.5}$$

Please refer to Appendix B.3 for details on the calculation of K_g.

Thus, increasing grasp force f_{int} tends to decrease k_Φ (Cutkosky and Kao, 1989), which further reduces the set of gains $K_{z,d}$ that satisfy the passivity criteria of Equation (5.4). Note that the $\cos^2(\Phi_p)$ term above appears because the effective moment arm between the yaw joint axis and the contact points and changes as a function of Φ_p, due to our definition of Φ_y and Φ_p in Equation (4.10). Additional load-dependent effects that arise from (5.1)-(5.2) should also be accounted for.

5.2 Object-Space Stiffness Control

5.2.1 Control Law

To manipulate object position/orientation within the hand, an object-space stiffness controller is designed to produce an object-level force/torque based on the

stiffness relation

$$\mathbf{f}_z = K_{z,d}(\mathbf{z}_d - \mathbf{z}) \tag{5.6}$$

where $K_{z,d}$ is the desired object-space stiffness and $\mathbf{z}_d$ is desired object pose.

However, instead of using a stiffness relation to determine f_{int} based on Δw_{obj}, f_{int} is calculated analytically at each time step to satisfy a desired minimum normal force $f_{grip,min}$ at each contact point (see Appendix B.2), just as was done in Section 4.2.4. This has the effect of making the sixth diagonal element of $K_{z,d}$ equal to zero, while also introducing coupling terms along the sixth row and column of $K_{z,d}$. During a grasp, the sixth diagonal element of $K_{z,pass}$ includes the object's internal stiffness and thus tends to be large, creating an eigenvector of $K_{z,pass} - K_{z,d}$ closely aligned with the f_{int} direction with an eigenvalue $\gg 0$. Thus, it can be assumed that for sufficiently non-compliant objects the f_{int} direction will not contribute to stiffness passivity bound violations.

The resulting $\mathbf{f}_z$ is used to calculate desired $\mathbf{f}_x$ through Equation (4.15), which are then sent to the individual Cartesian force control algorithms of the ACT index fingers and thumb.

5.2.2 Experimental Testing with the ACT hand

In this section, object manipulation is performed with the ACT hand using the above object stiffness control law, focusing specifically on the task of changing object yaw angle (see Figure 5.1, left).

First, experimental testing is performed to study the effect of increasing $K_{z,d}$ on stability. As object rotational stiffness k_Φ is increased to the point that the passivity bound of Equation (5.4) is violated, the system becomes less stable, resulting in grasp

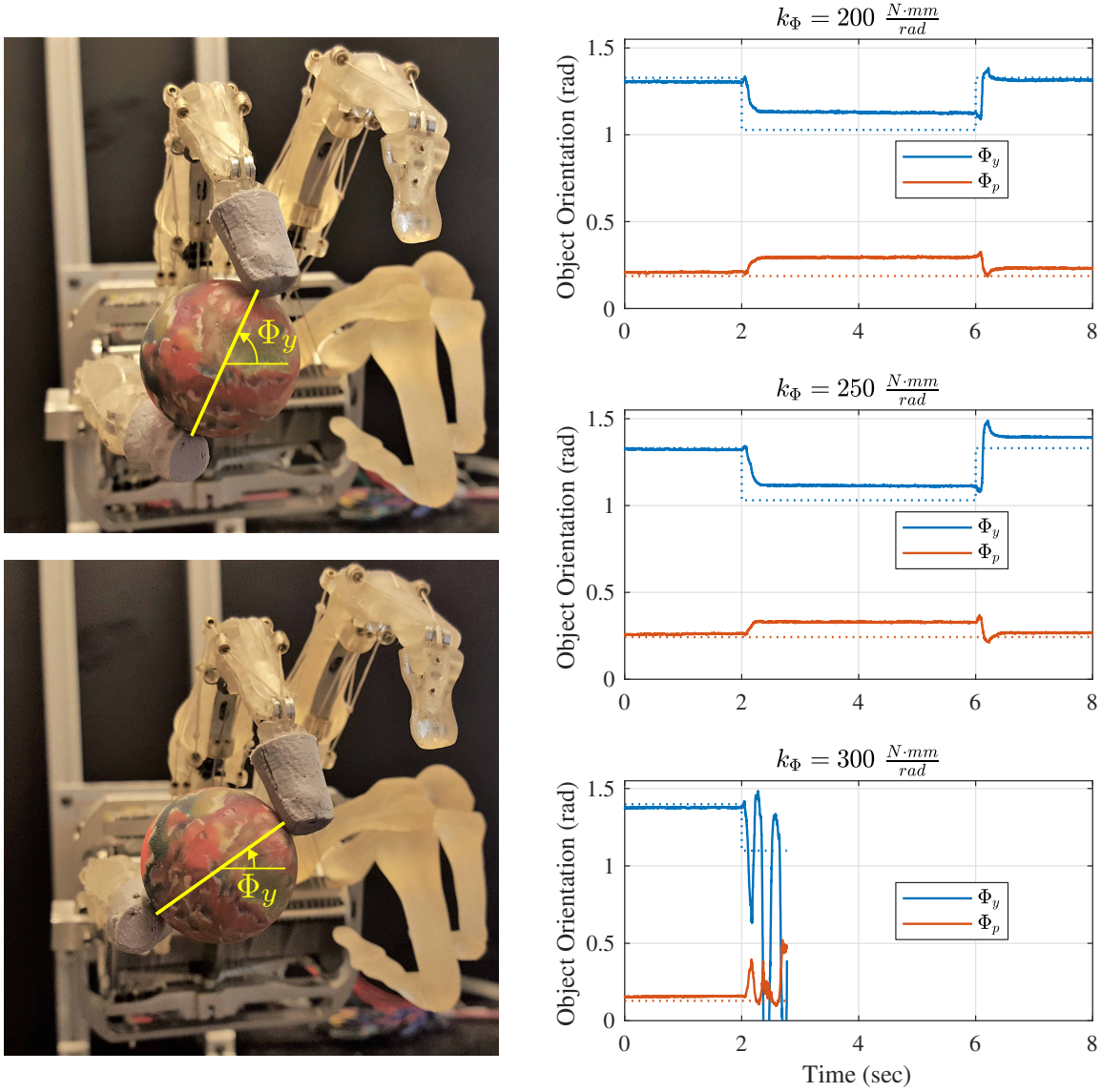

Figure 5.1: Object stiffness control for the task of tracking step changes to object yaw angle Φ_y. *Left:* Snapshots demonstrating the object rotation being performed (exaggerated changes to Φ_y for clarity). *Right:* Results for a range of orientation stiffness (k_Φ) values. Internal grasp force is set to $f_{grip,min} = 2$ N and translational components of object stiffness are $k_{o,x} = 0.1\ \frac{N}{mm}$ for all cases. As k_Φ increases past 250 $\frac{N \cdot mm}{rad}$, the passivity bound in Equation (5.4) is violated, and the system goes unstable.

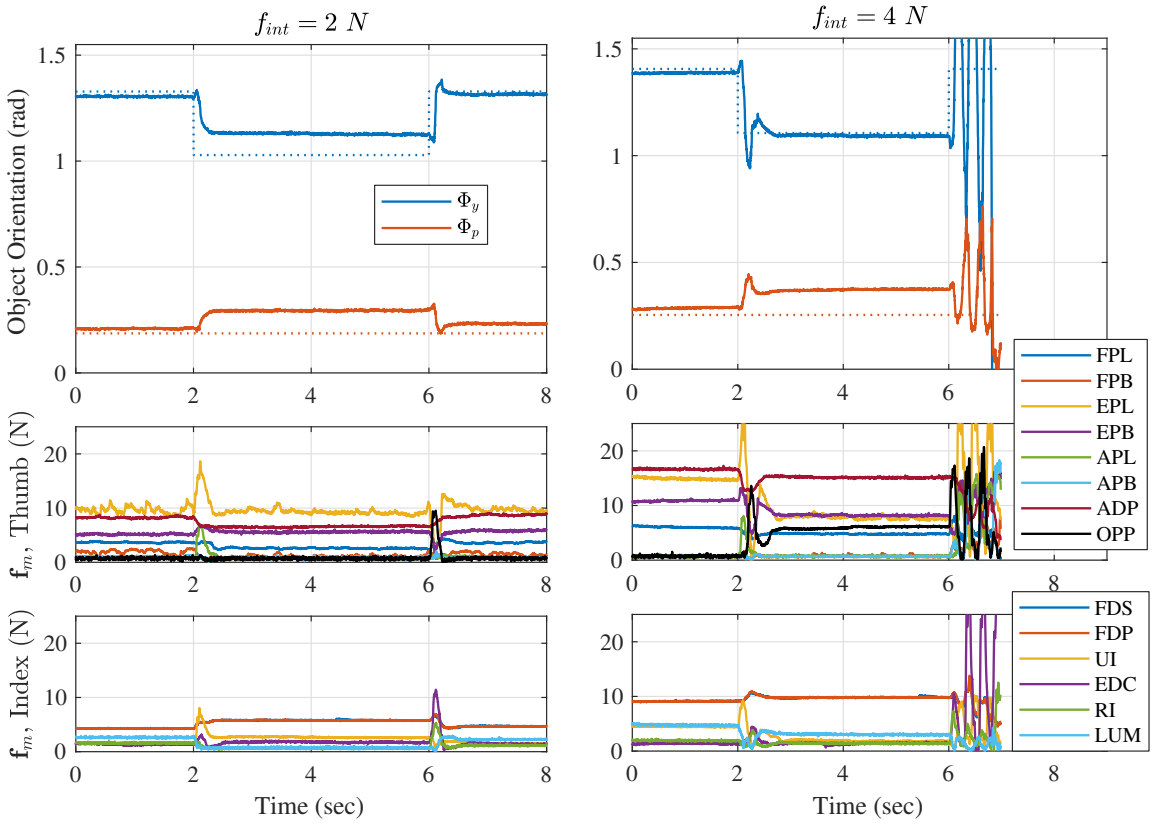

Figure 5.2: Object stiffness control results given different levels of internal grasp forces f_{int}. Object stiffness gains are set to the equivalent to those in the top plot of Figure 5.1 ($k_\Phi = 200\ \frac{N \cdot mm}{rad}$). The last two rows of plots indicate thumb and finger muscle forces, and are included to illustrate the higher muscle force magnitudes required for larger values of $f_{grip,min}$. As the applied grasp force increases from 2 to 4 N, the resulting changes to $K_{z,pass}$ are such that the passivity bound in Equation (5.4) is violated, and the system goes unstable.

failure (Figure 5.1, right).

Next, the effect of increasing applied grasp force $f_{grip,min}$ is tested. In Figure 5.2, for a case that was previously stable in Figure 5.1, increasing $f_{grip,min}$ from 2 to 4 N leads to grasp instability. This is because $K_{z,pass}$ is altered through Equation (5.5), reducing the set of achievable object gains $K_{z,d}$ that satisfy passivity as

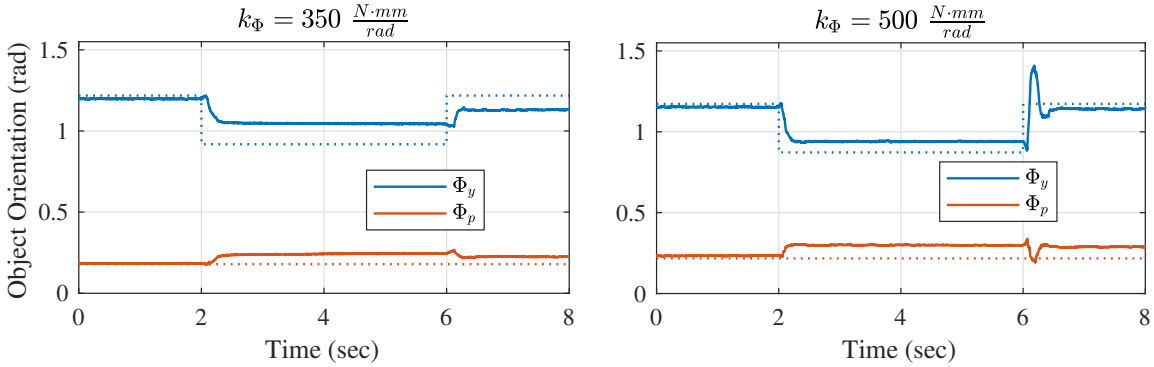

Figure 5.3: Object stiffness control results given an object of increased width compared to the cases in Figures 5.1-5.2 (from ∼30 mm wide ball to a ∼57 mm wide racquetball, the same used in the R2 experiments of Section 3.4). In this case, k_Φ can be increased to much higher levels (up to 500 $\frac{N \cdot mm}{rad}$) without causing grasp instability.

grasp force is increased.

Lastly, testing is performed to study the effect of changing object size. In Figure 5.3, w_{obj} is nearly doubled from previous cases, leading to a significantly increased range of stable $K_{z,d}$ values.

Based on this analysis and experimental results, object stiffness control requires carefully chosen $K_{z,d}$ gains, informed by both robotic system and manipulation task parameters, to ensure grasp stability. For compliant robotic systems or for tasks with small objects or large grasp forces, the achievable $K_{z,d}$ can be severely limited. In the next section, I develop a novel human-inspired muscle-space stiffness control strategy, with the goal of increasing achievable $K_{z,d}$ without compromising grasp stability.

5.3 Muscle-Space Stiffness Control

5.3.1 Inspiration from Human Neuromuscular System

Human biomechanical research has consistently pointed out that human system has a fundamentally hierarchical control structure. Low-level reflexes and inherent muscle impedance properties provide robustness and quick responses to disturbances, while higher-level CNS commands act to coordinate muscles toward a desired goal. For tasks like upright standing, the CNS must actively contribute feedback control actions to maintain stable posture (Casadio et al., 2005). By contrast, most hand tasks, like object grasping and manipulation, require faster corrective movements and thus rely heavily on muscle impedance properties for stability (Morasso, 2011).

There exist multiple hypotheses describing the form of internal neural control signals. One of the most prevalent is the equilibrium point hypothesis, first introduced in the work of Feldman (1986) (see also Feldman and Levin (2009)), which states that the CNS only directly controls the threshold lengths of muscles, while muscle forces arise naturally from inherent muscle properties, reflexes, and central control mechanisms, resulting in a nonlinear spring-like muscle behavior with the specified threshold length as the resting point.During object manipulation, the CNS updates its neural signals (i.e. muscle resting lengths) based on feed-forward models of expected object and environmental properties, along with reactionary adjustments to sensory cues (Flanagan et al., 2006). However, updates from the CNS occur at a relatively slow rate, such that the passive stiffness of the system for rapid disturbances is dominated by the inherent muscle properties (Hu et al., 2011).

In this section, I develop a human-inspired ACT hand control strategy that implements stiffness only in *muscle-space*, while muscle resting lengths are updated

gradually based on the task requirements. My primary interest is the quasi-static stiffness properties of the finger, and thus the complex effects of nonlinear damping properties, muscle activation dynamics, and biological delays lie outside the scope of this work.

5.3.2 Control Design

To begin, a muscle-space stiffness control relation is defined as follows:

$$\mathbf{f}_m = K_{m,d}(\boldsymbol{\ell}_{m,d} - \boldsymbol{\ell}_m) \tag{5.7}$$

where $K_{m,d}$ is a diagonal desired stiffness matrix and $\boldsymbol{\ell}_{m,d}$ is desired position in muscle-space.

Expressing the passivity bound from the previous section in muscle-space,

$$K_{m,pass} - K_{m,d} > 0 \tag{5.8}$$

it can be seen that ensuring system passivity becomes a straightforward element-wise comparison to check that active muscle stiffness $K_{m,d}$ remains lower than passive tendon stiffness $K_{m,pass}$.

The challenge for muscle-space stiffness control is determining appropriate desired muscle positions $\boldsymbol{\ell}_{m,d}$ to achieve a given task. For this, at each time step the object-space stiffness and Cartesian force control algorithms from the previous sections are utilized to calculate a set of muscle forces $\hat{\mathbf{f}}_m$ that can be considered an appropriate control action for a given desired object motion. We then calculate the "ideal" desired muscle positions $\hat{\boldsymbol{\ell}}_{m,d}$ as:

$$\hat{\boldsymbol{\ell}}_{m,d} = \boldsymbol{\ell}_m + K_{m,d}^{-1}\hat{\mathbf{f}}_m \tag{5.9}$$

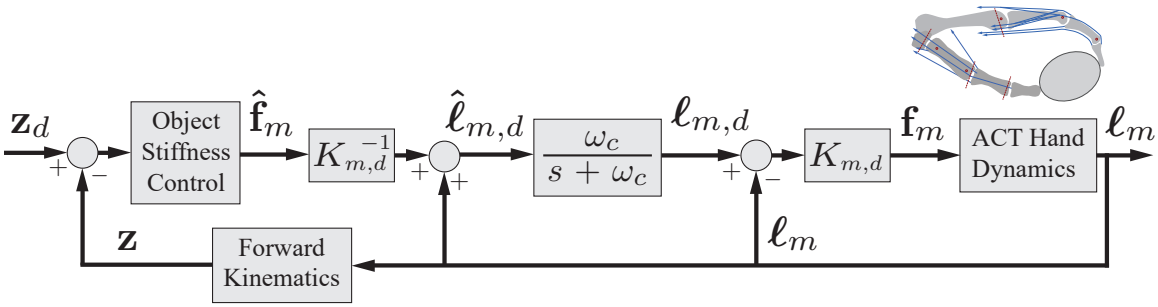

Figure 5.4: Control block diagram of muscle-space stiffness control strategy, with muscle lengths $\boldsymbol{\ell}_{m,d}$ updating through a low-pass filter with cut-off frequency ω_c based on an object stiffness control strategy.

If the desired muscle positions were simply set to $\boldsymbol{\ell}_{m,d} = \hat{\boldsymbol{\ell}}_{m,d}$ at each time step, the system would behave as a pure object stiffness controller. Instead, a low-pass filter is utilized to update $\boldsymbol{\ell}_{m,d}$ at a relatively slow rate compared to the system's dynamics:

$$\boldsymbol{\ell}_{m,d}^{k+1} = \boldsymbol{\ell}_{m,d}^{k} + \omega_c(\hat{\boldsymbol{\ell}}_{m,d}^{k+1} - \boldsymbol{\ell}_{m,d}^{k})\Delta t \tag{5.10}$$

where ω_c is the filter cutoff frequency in radians/sec. A block diagram of this control law can be found in Figure 5.4.

This combination of muscle- and object-space stiffness control has several unique characteristics. Because $\boldsymbol{\ell}_{m,d}$ is updated relatively slowly, the system's dynamics are dominated by muscle stiffness $K_{m,d}$, such that system passivity can be ensured through in a simple manner through Equation (5.8). However, as the system reaches quasi-static equilibrium and $\boldsymbol{\ell}_{m,d} \to \hat{\boldsymbol{\ell}}_{m,d}$, the chosen object-space stiffness gains $K_{z,d}$ will determine the relationship between object-space error and applied force/torque, such that external object interactions are intuitively decoupled and well-defined.

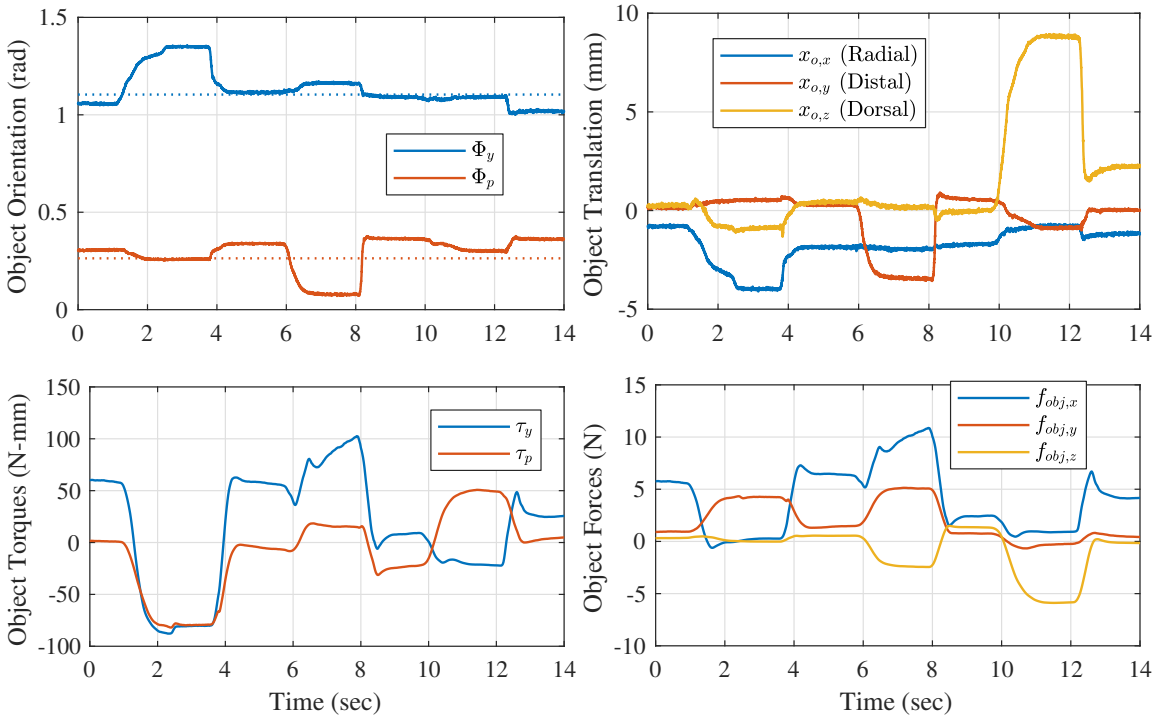

Figure 5.5: Disturbance response for a muscle-space stiffness controller while grasping an object with fixed $\boldsymbol{\ell}_{m,d}$, determined at the initial time step to produce a grasp force of $f_{grip,min} = 3$ N. Disturbances are successively applied and released in the Φ_y, Φ_p, and $x_{o,z}$ directions.

5.3.3 Experimental Results

To begin, disturbance testing is performed for the muscle stiffness controller in Equation (5.7) with constant, non-updating muscle resting lengths $\boldsymbol{\ell}_{m,d}$, which are determined at the initial time step to produce an internal force of 3 N. Muscle stiffness for every muscle is set to $k_m = 5\ \frac{N}{mm}$, which is slightly below the passive stiffness of the tendons and thus satisfies Equation (5.8).

In Figure 5.5, it can be seen that as disturbances are applied sequentially to Φ_y, Φ_p, and $x_{o,z}$, the system applies restoring object forces/torques $\mathbf{f}_z$ to return it to its original position (with some steady-state error due to friction). However,

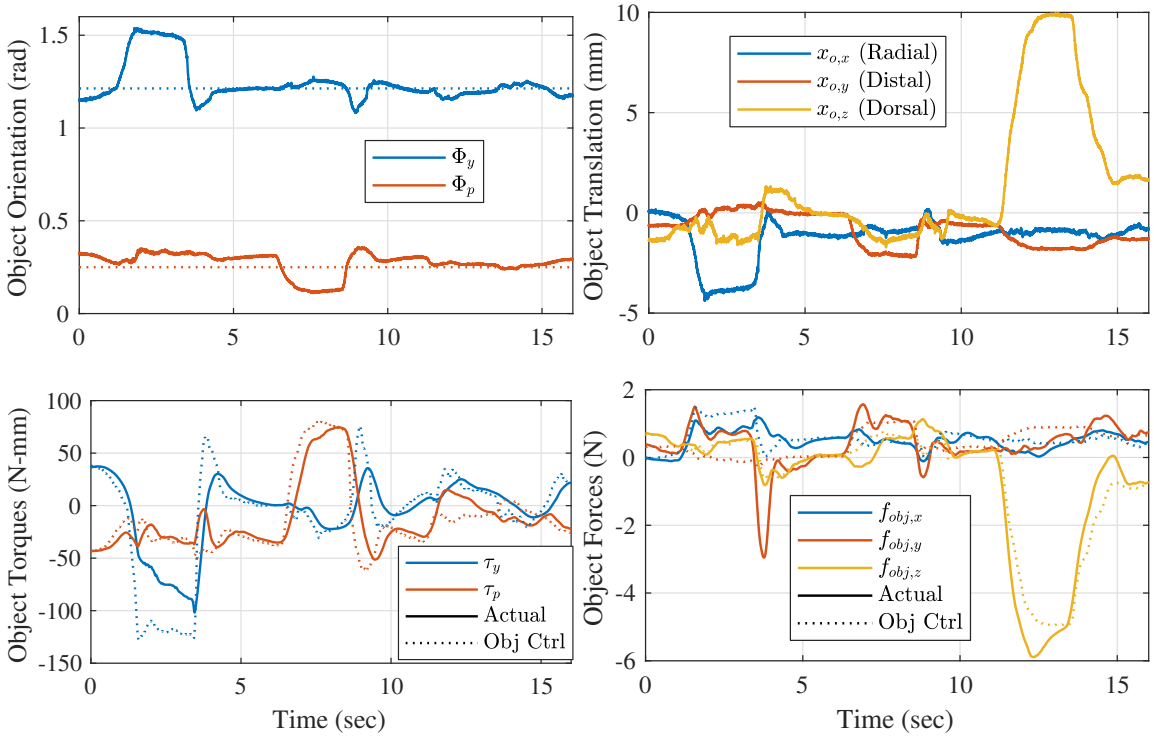

Figure 5.6: Disturbance response for a muscle-space stiffness controller with $\boldsymbol{\ell}_{m,d}$ updating based on an object-space stiffness control law. The low-pass filter cutoff frequency is $\omega_c = 0.5$ Hz, translational object stiffness in all directions is set to $k_{o,x} = 0.5\ \frac{N}{mm}$, rotational stiffness is $k_\Phi = 600\ \frac{N \cdot mm}{rad}$, and $f_{grip,min} = 3$ N. Disturbances are successively applied and released in the Φ_y, Φ_p, and $x_{o,z}$ directions.

the resulting effective object stiffness is highly coupled, such that a disturbance in any direction also results in significant components of $\mathbf{f}_z$ in the other rotational and translational directions.

We next performed disturbance testing for the muscle stiffness controller with updating $\boldsymbol{\ell}_{m,d}$ based on the object stiffness control law from Section 5.2. The results in Figure 5.6 demonstrate the ability to emulate an object-space rotational stiffness k_Φ that is doubled from the previously unstable value of 300 $\frac{N \cdot mm}{rad}$ while retaining stability. This is because muscle-space stiffness dominates the dynamics during rapid

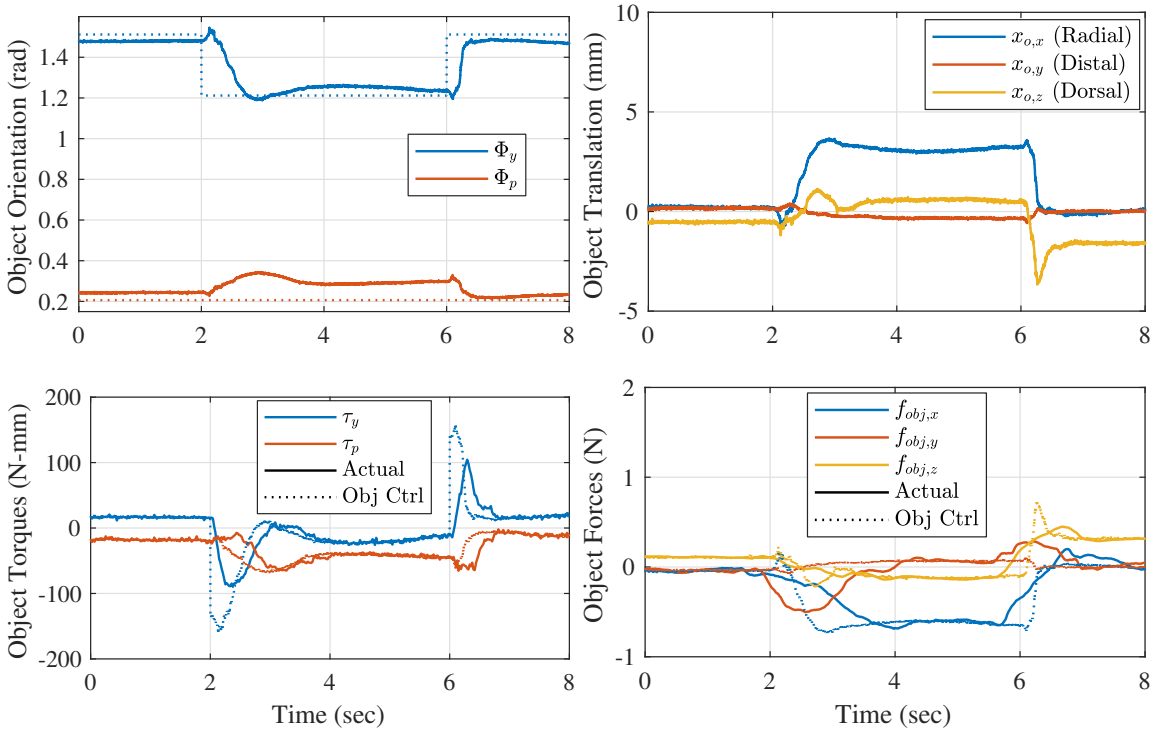

Figure 5.7: Trajectory tracking results for muscle-space stiffness control with step changes to Φ_y, given control parameters $\omega_c = 0.5$ Hz, $k_{o,x} = 0.2\ \frac{N}{mm}$, $k_\Phi = 600\ \frac{N \cdot mm}{rad}$, and $f_{grip,min} = 2$ N.

disturbances. As the system reaches quasi-static equilibrium after a disturbance, $\mathbf{f}_z$ approaches values corresponding to the desired object-space stiffness relationship $K_{z,d}$ (multiplied a scaling factor α when actuators reach saturation).

Finally, object manipulation is demonstrated for the same yaw angle tracking task as before (Figure 5.7). The ability to increase object stiffness gains without creating instability leads to reduced steady-state error compared to the object stiffness controller in Figure 5.1. Thus, the use of integral gains or friction compensation for reducing steady-state error can be avoided, which would otherwise result in nonlinear behaviors that shift the system's dynamic response away from the desired impedance.

5.4 Discussion

In this chapter, I explored the inherent limitations of object-space stiffness control, and then developed a novel human-inspired control strategy that (i) produces quasi-static object-space stiffnesses well above what is possible with a typical object stiffness controller and (ii) ensures grasp stability for a wider range of manipulation task scenarios. First, mathematical analysis and experimental testing with the ACT hand is used to demonstrate the limitations on achievable object stiffness gains as a function of a robotic hand's compliance properties and the object manipulation task to be performed. Then, a novel muscle-space stiffness control strategy is developed and tested with the ACT hand, and results show that a previously unachievable object-space stiffness can be emulated in quasi-static conditions without resulting in grasp instability, provided $K_{m,d}$ and ω_c are properly chosen.

While the results presented in this work are specific to the ACT hand system, the control algorithm and passivity bounds are generalized and can be employed for any robotic hand system and in any coordinate space, based on its design, actuation, and passive compliance properties. By utilizing such a control strategy, robotic hands can utilize passive compliance to provide increased impact robustness, safer interactions, and force sensing without sacrificing hand dexterity and object manipulation capabilities.

Chapter 6

Conclusions

This dissertation has sought to explore the fundamental differences between the human hand musculoskeletal and neuromuscular systems and robotic hand design and control, with the goal of improving robotic hand dexterity. The human hand is a complex system with significant biological limitations, yet displays superior dexterity and manipulation capabilities compared to existing robotic and prosthetic hands. Through system modeling, analysis, and controller development for anthropomorphic and anatomical robotic hands, this work gleans insights into the advantages and challenges that arise from the unique musculoskeletal, biomechanical, and neuromuscular features of our hands.

This work makes several contributions to the field of biomechanical hand modeling. Chapter 2 presents a novel and powerful methodology for modeling the finger extensor mechanism, and then determines realistic musculotendon paths that replicate observed human thumb mechanics by utilizing the ACT thumb as a physical testbed. Additionally, the development of models and controllers for the ACT hand in Chapter 4 contribute to the biomechanics field by elucidating the unique mechanical effects and control challenges that arise from the human hand's unique musculotendon structure.

Then, contributions are made to the field of tendon-driven robotic hand control through the development and testing of control strategies for the anthropomorphic

Robonaut 2 hand in Chapter 3 and the ACT hand in Chapter 4 for achieving fine object manipulation. While the human-like tendon structure of the ACT hand requires significantly more modeling effort, the control strategies utilized for both the straightforward tendon transmission in Robonaut 2 and the ACT hand are remarkably similar. Demonstration of fine manipulation capabilities with the complex ACT hand structure is a significant milestone in the field of tendon-driven control, which we hope will encourage the development of innovative tendon-driven robotic and prosthetic hand designs that continue pushing forward their dexterous capabilities.

Finally, contributes are made to both the field of robotic hand control and the study of the human neuromuscular system through the development and testing of the human-inspired control algorithm in Chapter 5. Experimental results show that this control strategy can improve the manipulation capabilities of compliant robotic hands by increasing the achievable object stiffness emulated by the controller without sacrificing grasp stability. Human neuromuscular control acts similar to the developed control law, which provides evidence that the neuromuscular system's hierarchical control structure is crucial to human hand stability during manipulation tasks.

6.1 Future Work

Several possibilities exist for future research with the ACT hand. The control work could be extended to three-fingered object manipulation by incorporating the middle finger. Increasing the available sensory feedback from purely proprioceptive by adding joint angle and tactile sensing would lead to significantly improved modeling accuracy and control capabilities for the ACT hand. Mechanical design improvements focused on reducing friction and introducing more human-like stiffness and damping

properties would bring the system's dynamics closer to the human hand.

Secondly, using the advances in ACT hand control presented in this work, more in-depth ACT hand research can be performed studying human hand neuromuscular control. More realistic muscle models with nonlinear stiffness properties could be implemented, and the control strategies could be subsequently extended to account for the additional co-contraction stiffness variable that would be introduced. Also, it is not universally accepted by the research community that the human hand system acts as a fundamentally stiffness-controlled system (Venkadesan and Valero-Cuevas, 2008), as is the basic assumption in this work. Thus, research into other theorized human motor control models could be tested with the ACT hand, with the results compared with measured in vivo human hand data.

Finally, the insights gained from work could be applied toward the development of an innovative human-inspired robotic/prosthetic hand system. The design would likely be simplified and modified compared to the ACT hand for practical considerations, including reduction in actuator count and lowering of friction, but researchers could still learn from this work to determine the appropriate joint structure, tendon routing, and control strategies that will allow it to approach human levels of dexterity.

Appendices

Appendix A

ACT Hand Joint Kinematics

A.1 Index Finger

The ACT fingers can be modeled as serial chain linkages using the Denavit-Hartenberg (D-H) parameters (Hartenberg and Denavit, 1964) in Table A.1. Also listed are the index finger link lengths and location/orientation of the base frame. Note that the ACT hand also has a middle finger with the same joint configuration and slightly longer links, but it is not used in this work and is thus omitted here.

Table A.1: Parameters for a kinematic model of the ACT index finger.

Finger D-H Parameters				
Joint i	a_i	α_i	r_i	θ_i [a]
1	0	$-\pi/2$	0	θ_1
2	L_1	0	0	θ_2
3	L_2	0	0	θ_3
4	L_3	0	0	θ_4
Index Finger Parameter Values				
$\{L_1, L_2, L_3\}$	$\{51.55, 26.9, 18\}$ mm			
${}^{G}r_0$ [b]	$[-22.0, -7.0, 115.4]^T$ mm			
${}^{G}_{0}\mathbf{R}$ [c]	$\begin{bmatrix} -0.139 & 0.988 & -0.065 \\ 0.488 & 0.126 & 0.864 \\ 0.862 & 0.088 & -0.500 \end{bmatrix}$			

[a] The θ variables correspond to the finger MCP ab/ad, MCP flex, PIP, and DIP joints, in order.
[b] ${}^{G}r_0$ refers to the 3-D position of the base "0" frame, located at the MCP joint, with respect to a global "G" frame located in the center of the ACT hand's wrist, where the x, y, and z coordinates refer to the global ulnar, dorsal, and distal directions, respectively.
[c] ${}^{G}_{0}\mathbf{R}$ refers to the rotation matrix from frame "G" in the wrist to frame "0" of the finger.

Table A.2: Parameters for a kinematic model of the ACT thumb.

Thumb D-H Parameters				
Joint i	a_i	α_i	r_i	θ_i [a]
1	L_1	$\pi/2$	0	θ_1
2	0	$5\pi/6$	$L_2 \tan(\pi/3)$	$\theta_2 + \pi/2$
3	0	$\pi/2$	$L_2/\cos(\pi/3)$	$-\theta_3 + \pi/2$
4	L_3	0	0	$\theta_4 + \pi/6$
5	L_4	0	0	θ_5
Thumb Parameter Values				
$\{L_1, L_2, L_3, L_4\}$	$\{23.1, 43.2, 36.5, 26\}$ mm			
${}^{G}r_0$ [b]	$[-31.2, -8.6, 30.4]^T$ mm			
${}^{G}_{0}\mathbf{R}$ [c]	$\begin{bmatrix} 0 & 0.956 & 0.293 \\ -0.479 & -0.257 & 0.839 \\ 0.877 & -0.141 & 0.459 \end{bmatrix}$			

[a] The θ variables correspond to the thumb CMC flex, CMC ab/ad, MCP ab/ad, MCP flex, and IP joints, in order.

[b] ${}^{G}r_0$ refers to the 3-D position of the base "0" frame, located at the CMC flex joint, with respect to a global "G" frame located in the center of the ACT hand's wrist, where the x, y, and z coordinates refer to the global ulnar, dorsal, and distal directions, respectively.

[c] ${}^{G}_{0}\mathbf{R}$ refers to the rotation matrix from frame "G" in the wrist to frame "0" of the thumb.

A.2 Thumb

The thumb has a more complex joint structure than the fingers, as can be seen in Figure 2.10 and from the D-H parameters in Table A.2. Note that offsets are added to θ values to make it so that when all joint angles are zero, the thumb will be in an extended pose pointing in the approximate global distal direction. Also, a sign change for θ_3 is necessary so that CMC ab/ad and MCP ab/ad joint motions are in the same direction, i.e. positive angle changes to either joint tend to move the thumb in the ulnar direction.

Appendix B

Object-Space Transformations and Control

B.1 Grasp Matrix

First, a full calculation of the grasp matrix is presented for a two-fingered grasp object-space coordinates as defined in Equation (4.10). Given the inverse object kinematics function $\mathbf{x}(\mathbf{z})$ defined in Equations (4.11)-(4.12) and the grasp matrix calculation in Equation (4.13), the full expression for grasp matrix can be found as:

$$W(\mathbf{z}) = \begin{bmatrix} 1 & 0 & 0 & 1 & 0 & 0 \\ 0 & 1 & 0 & 0 & 1 & 0 \\ 0 & 0 & 1 & 0 & 0 & 1 \\ \frac{w_{obj}}{2}c_p s_y & 0 & \frac{w_{obj}}{2}c_p c_y & -\frac{w_{obj}}{2}c_p s_y & 0 & -\frac{w_{obj}}{2}c_p c_y \\ \frac{w_{obj}}{2}s_p c_y & \frac{w_{obj}}{2}c_p & -\frac{w_{obj}}{2}s_p s_y & -\frac{w_{obj}}{2}s_p c_y & -\frac{w_{obj}}{2}c_p & \frac{w_{obj}}{2}s_p s_y \\ -\frac{1}{2}c_p c_y & \frac{1}{2}s_p & \frac{1}{2}c_p s_y & \frac{1}{2}c_p c_y & -\frac{1}{2}s_p & -\frac{1}{2}c_p s_y \end{bmatrix} \quad \text{(B.1)}$$

where $c_p = \cos(\Phi_p)$, $s_p = \sin(\Phi_p)$, $c_y = \cos(\Phi_y)$, and $s_y = \sin(\Phi_y)$.

Then, the inverse of the grasp matrix can be calculated as:

$$W^{-1}(\mathbf{z}) = \begin{bmatrix} \frac{1}{2} & 0 & 0 & \frac{s_y}{w_{obj}c_p} & \frac{s_p c_y}{w_{obj}} & -c_p c_y \\ 0 & \frac{1}{2} & 0 & 0 & \frac{c_p}{w_{obj}} & s_p \\ 0 & 0 & \frac{1}{2} & \frac{c_y}{w_{obj}c_p} & \frac{-s_p s_y}{w_{obj}} & c_p s_y \\ \frac{1}{2} & 0 & 0 & \frac{-s_y}{w_{obj}c_p} & \frac{-s_p c_y}{w_{obj}} & c_p c_y \\ 0 & \frac{1}{2} & 0 & 0 & \frac{-c_p}{w_{obj}} & -s_p \\ 0 & 0 & \frac{1}{2} & \frac{-c_y}{w_{obj}c_p} & \frac{s_p s_y}{w_{obj}} & -c_p s_y \end{bmatrix} \quad \text{(B.2)}$$

Notice that the last column of W^{-1}, which corresponds to the internal force variable f_{int} for the inverse force/torque relation $\mathbf{f}_x = W^{-1}\mathbf{f}_z$ in Equation (4.15), contains two unit vectors pointing outwards along the line between the index finger and thumb, such that increasing f_{int} leads to a corresponding decrease in the internal grasp force being applied, and vice versa. However, for simplicity in the text, Also, W^{-1} is undefined when $\cos(\Phi_p) = 0$ or $w_{obj} = 0$, which corresponds to the singularity positions of the grasp matrix W.

B.2 Internal Grip Force Calculation

In this work, object-space control is achieved using the inverse grasp matrix relation defined in Equation (4.15):

$$\mathbf{f}_x = W^{-1}(\mathbf{z})\mathbf{f}_z \tag{4.15}$$

The last term of $\mathbf{f}_z$ is an internal force term f_{int}, which in the object-space control laws in this work is calculated analytically at each time step to guarantee a minimum normal contact force is being applied at each contact point. In this section, we will describe how f_{int} is calculated.

To begin, the unit vectors corresponding to the directions of internal grasp force at each contact point are calculated. These can be found in the last column of W^{-1}, where the first three elements correspond to the unit internal force vector $\hat{\mathbf{f}}_{int,f}$ corresponding to the finger, and the last three elements correspond to the unit internal force vector $\hat{\mathbf{f}}_{int,t}$ for the thumb. Note that these unit vectors are pointing outward from the object's center.

Then, after first calculating an initial value of $\mathbf{f}_x = [\mathbf{f}_{x,f}^T,\ \mathbf{f}_{x,t}^T]^T$ using Equation (4.15) with $f_{int} = 0$, we find the magnitude of the contact force vectors $\mathbf{f}_{x,f}$ and

$\mathbf{f}_{x,t}$ projected onto their corresponding internal force vectors:

$$f_{int,f} = \mathbf{f}_{x,f} \cdot \hat{\mathbf{f}}_{int,f} \tag{B.3}$$

$$f_{int,t} = \mathbf{f}_{x,t} \cdot \hat{\mathbf{f}}_{int,t} \tag{B.4}$$

Then, given a specified minimum normal contact force $f_{grip,min}$ to be applied by each finger, the internal force term f_{int} is calculated as:

$$f_{int} = -f_{grip,min} - \max(f_{int,f}, f_{int,t}) \tag{B.5}$$

Using this f_{int} value inserted into $\mathbf{f}_z$, the re-calculation of the object-space equation in Equation (4.15) results in contact forces $\mathbf{f}_{x,f}$ and $\mathbf{f}_{x,t}$ that will apply a minimum normal contact force of $f_{grip,min}$.

B.3 Stiffness Transformation

Here, the transformation from end-tip-space (K_x) to object-space (K_z) is calculated, including load-dependent stiffness terms due to internal grasp force. Reiterating Equation (5.3), this transformation can be defined as follows:

$$K_z = W(\mathbf{z})K_x W^T(\mathbf{z}) + \left[\frac{\partial W(\mathbf{z})}{\partial \mathbf{z}} W^{-1}(\mathbf{z})\mathbf{f}_z\right] \tag{5.3}$$

Assuming the effective end-tip stiffnesses K_x is known, the first term can be easily calculated using the grasp matrix from Equation (B.1).

The last term of Equation (5.3), which for simplicity is denoted in this work as K_g, is slightly more difficult to calculate. Using methods outlined by Chen and Kao (2000) for joint- and Cartesian-space, K_g can be found as:

$$\begin{aligned} K_g &= \left[\frac{\partial W(\mathbf{z})}{\partial \mathbf{z}} W^{-1}(\mathbf{z})\mathbf{f}_z\right] \\ &= \left[\left(\frac{\partial W(\mathbf{z})}{\partial z_1} W^{-1}\mathbf{f}_z\right) \quad \left(\frac{\partial W(\mathbf{z})}{\partial z_2} W^{-1}\mathbf{f}_z\right) \quad \ldots \quad \left(\frac{\partial W(\mathbf{z})}{\partial z_6} W^{-1}\mathbf{f}_z\right)\right] \end{aligned} \tag{B.6}$$

Analytically simplifying this equation, the following expression for K_g can be found.

$$K_g = \begin{bmatrix} 0 & 0 & 0 & 0 & 0 & 0 \\ 0 & 0 & 0 & 0 & 0 & 0 \\ 0 & 0 & 0 & 0 & 0 & 0 \\ 0 & 0 & 0 & \tau_p c_p s_p - f_{int} w_{obj} c_p^2 & -\tau_y \tan(\Phi_p) & \frac{\tau_y}{w_{obj}} \\ 0 & 0 & 0 & -\tau_y \tan(\Phi_p) & -f_{int} w_{obj} & \frac{\tau_p}{w_{obj}} \\ 0 & 0 & 0 & \frac{\tau_y}{w_{obj}} & \frac{\tau_p}{w_{obj}} & 0 \end{bmatrix} \tag{B.7}$$

Note that for the calculation of K_g, $\mathbf{f}_z$ corresponds to the external forces/torques being applied to the fingers. Thus, although for inverse grasp matrix calculations, positive f_{int} values produce outward fingertip forces, for the calculation of K_g positive values of f_{int} correspond to increasing the applied grasp force.

For the case of an unloaded grasp, i.e. no external forces/torques are being applied to the object or fingers, only the internal grasp force f_{int} will be present. In this case, K_g is a matrix with all elements equal to zero except two diagonal elements $k_{g,\Phi_y} = -f_{int} w_{obj} \cos^2(\Phi_p)$ and $k_{g,\Phi_p} = -f_{int} w_{obj}$. The implications of this finding is discussed in greater detail in Section 5.1.1.2.

Bibliography

Muhammad E Abdallah, Robert Platt, Charles W Wampler, and Brian Hargrave. Applied joint-space torque and stiffness control of tendon-driven fingers. In *IEEE-RAS International Conference on Humanoid Robots (Humanoids)*, pages 74–79, 2010.

Alin Albu-Schäffer, Christian Ott, and Gerd Hirzinger. A unified passivity-based control framework for position, torque and impedance control of flexible joint robots. *The International Journal of Robotics Research*, 26(1):23–39, 2007.

Kai-Nan An, Y Ueba, EY Chao, WP Cooney, and RL Linscheid. Tendon excursion and moment arm of index finger muscles. *Journal of Biomechanics*, 16(6):419–425, 1983.

Luigi Biagiotti, Hong Liu, Gerd Hirzinger, and Claudio Melchiorri. Cartesian impedance control for dexterous manipulation. In *IEEE/RSJ International Conference on Intelligent Robots and Systems (IROS)*, volume 4, pages 3270–3275, 2003.

Antonio Bicchi. Hands for dexterous manipulation and robust grasping: A difficult road toward simplicity. *IEEE Transactions on Robotics and Automation*, 16(6): 652–662, 2000.

Paul W Brand and Anne Hollister. *Clinical mechanics of the hand*. Mosby Incorporated, 1999.

Lyndon B Bridgwater, CA Ihrke, Myron A Diftler, Muhammad E Abdallah, Nicolaus A Radford, JM Rogers, S Yayathi, R Scott Askew, and D Marty Linn. The Robonaut 2 hand – Designed to do work with tools. In *IEEE International Conference on Robotics and Automation (ICRA)*, pages 3425–3430, 2012.

N Brook, J Mizrahi, M Shoham, and J Dayan. A biomechanical model of index finger dynamics. *Medical Engineering & Physics*, 17(1):54–63, 1995.

Helmut J Buchner, Margaret J Hines, and Hooshang Hemami. A dynamic model for finger interphalangeal coordination. *Journal of Biomechanics*, 21(6):459–468, 1988.

Etienne Burdet, Rieko Osu, David W Franklin, Theodore E Milner, and Mitsuo Kawato. The central nervous system stabilizes unstable dynamics by learning optimal impedance. *Nature*, 414(6862):446–449, 2001.

Jörg Butterfaß, Markus Grebenstein, Hong Liu, and Gerd Hirzinger. DLR-Hand II: Next generation of a dextrous robot hand. In *IEEE International Conference on Robotics and Automation (ICRA)*, volume 1, pages 109–114, 2001.

Maria Chiara Carrozza, C Suppo, Fabrizio Sebastiani, Bruno Massa, Fabrizio Vecchi, Roberto Lazzarini, Mark R Cutkosky, and Paolo Dario. The SPRING hand: Development of a self-adaptive prosthesis for restoring natural grasping. *Autonomous Robots*, 16(2):125–141, 2004.

Maura Casadio, Pietro G Morasso, and Vittorio Sanguineti. Direct measurement of ankle stiffness during quiet standing: Implications for control modelling and clinical application. *Gait & Posture*, 21(4):410–424, 2005.

Maxime Chalon, Werner Friedl, Jens Reinecke, Thomas Wimboeck, and Alin Albu-Schaeffer. Impedance control of a non-linearly coupled tendon driven thumb. In *IEEE/RSJ International Conference on Intelligent Robots and Systems (IROS)*, pages 4215–4221, 2011.

Lillian Y Chang and Yoky Matsuoka. A kinematic thumb model for the ACT hand. In *IEEE International Conference on Robotics and Automation (ICRA)*, pages 1000–1005, 2006.

EY Chao and Kai-Nan An. Graphical interpretation of the solution to the redundant problem in biomechanics. *Journal of Biomechanical Engineering*, 100(3):159–167, 1978.

Shih-Feng Chen and Imin Kao. Conservative congruence transformation for joint and Cartesian stiffness matrices of robotic hands and fingers. *The International Journal of Robotics Research*, 19(9):835–847, 2000.

Mark R Cutkosky and Imin Kao. Computing and controlling compliance of a robotic hand. *IEEE Transactions on Robotics and Automation*, 5(2):151–165, 1989.

Ashish D Deshpande, Ravi Balasubramanian, Ralph Lin, Brian Dellon, and Yoky Matsuoka. Understanding variable moment arms for the index finger MCP joints through the ACT hand. In *IEEE RAS & EMBS International Conference on Biomedical Robotics and Biomechatronics (BioRob)*, pages 776–782, 2008.

Ashish D Deshpande, Jonathan Ko, Dieter Fox, and Yoky Matsuoka. Anatomically Correct Testbed hand control: Muscle and joint control strategies. In *IEEE International Conference on Robotics and Automation (ICRA)*, pages 4416–4422, 2009.

Ashish D Deshpande, Ravi Balasubramanian, Jonathan Ko, and Yoky Matsuoka. Acquiring variable moment arms for index finger using a robotic testbed. *IEEE Transactions on Biomedical Engineering*, 57(8):2034–2044, 2010.

Ashish D Deshpande, Jonathan Ko, Dieter Fox, and Yoky Matsuoka. Control strategies for the index finger of a tendon-driven hand. *The International Journal of Robotics Research*, 32(1):115–128, 2013a.

Ashish D Deshpande, Zhe Xu, Michael J Vande Weghe, Benjamin H Brown, Jonathan Ko, Lillian Y Chang, David D Wilkinson, Sean M Bidic, and Yoky Matsuoka. Mechanisms of the Anatomically Correct Testbed hand. *IEEE/ASME Transactions on Mechatronics*, 18(1):238–250, 2013b.

Aaron M Dollar and Robert D Howe. The highly adaptive SDM hand: Design and performance evaluation. *The International Journal of Robotics Research*, 29(5): 585–597, 2010.

James N Dreyfus and Thomas J Schnitzer. Pathogenesis and differential diagnosis of the swan-neck deformity. In *Seminars in Arthritis and Rheumatism*, volume 13, pages 200–211. Elsevier, 1983.

Anatol G Feldman. Once more on the equilibrium-point hypothesis (λ model) for motor control. *Journal of Motor Behavior*, 18(1):17–54, 1986.

Anatol G Feldman and Mindy F Levin. The equilibrium-point hypothesis–past, present and future. In *Progress in motor control*, pages 699–726. Springer, 2009.

Fanny Ficuciello, Gianluca Palli, Claudio Melchiorri, and Bruno Siciliano. Experimental evaluation of postural synergies during reach to grasp with the UB Hand IV.

In *IEEE/RSJ International Conference on Intelligent Robots and Systems (IROS)*, pages 1775–1780, 2011.

J Randall Flanagan, Miles C Bowman, and Roland S Johansson. Control strategies in object manipulation tasks. *Current Opinion in Neurobiology*, 16(6):650–659, 2006.

NK Fowler, Alexander C Nicol, B Condon, and D Hadley. Method of determination of three dimensional index finger moment arms and tendon lines of action using high resolution MRI scans. *Journal of biomechanics*, 34(6):791–797, 2001.

Werner Friedl, Maxime Chalon, Jens Reinecke, and Markus Grebenstein. FRCEF: The new friction reduced and coupling enhanced finger for the Awiwi hand. In *IEEE-RAS International Conference on Humanoid Robots (Humanoids)*, pages 140–147, 2015.

Marc Garcia-Elias, Kai-Nan An, Lawrence Berglund, Ronald L Linscheid, William P Cooney, and Edmund YS Chao. Extensor mechanism of the fingers. I. A quantitative geometric study. *The Journal of Hand Surgery*, 16(6):1130–1136, 1991a.

Marc Garcia-Elias, Kai-Nan An, Lawrence J Berglund, Ronald L Linscheid, William P Cooney, and Edmund YS Chao. Extensor mechanism of the fingers. II. Tensile properties of components. *The Journal of Hand Surgery*, 16(6):1136–1140, 1991b.

DJ Giurintano, AM Hollister, WL Buford, DE Thompson, and LM Myers. A virtual five-link model of the thumb. *Medical Engineering & Physics*, 17(4):297–303, 1995.

Craig M Goehler and Wendy M Murray. The sensitivity of endpoint forces produced by the extrinsic muscles of the thumb to posture. *Journal of Biomechanics*, 43(8): 1553–1559, 2010.

Markus Grebenstein, Maxime Chalon, Werner Friedl, Sami Haddadin, Thomas Wimböck, Gerd Hirzinger, and Roland Siegwart. The hand of the DLR hand arm system: Designed for interaction. *The International Journal of Robotics Research*, 31(13):1531–1555, 2012.

Paul L Gribble, David J Ostry, Vittorio Sanguineti, and Rafael Laboissière. Are complex control signals required for human arm movement? *Journal of Neurophysiology*, 79(3):1409–1424, 1998.

Richard Scheunemann Hartenberg and Jacques Denavit. *Kinematic synthesis of linkages*. McGraw-Hill, 1964.

Neville Hogan. Impedance control: An approach to manipulation. *Journal of Dynamic Systems, Measurement, and Control*, 107:1–24, 1985.

Anne Hollister, William L Buford, Loyd M Myers, David J Giurintano, and Andrew Novick. The axes of rotation of the thumb carpometacarpal joint. *Journal of Orthopaedic Research*, 10(3):454–460, 1992.

Anne Hollister, David J Giurintano, William L Buford, Loyd M Myers, and Andrew Novick. The axes of rotation of the thumb interphalangeal and metacarpophalangeal joints. *Clinical Orthopaedics and Related Research*, 320:188–193, 1995.

Katherine RS Holzbaur, Wendy M Murray, and Scott L Delp. A model of the upper extremity for simulating musculoskeletal surgery and analyzing neuromuscular control. *Annals of Biomedical Engineering*, 33(6):829–840, 2005.

Xiao Hu, Wendy M Murray, and Eric J Perreault. Muscle short-range stiffness can

be used to estimate the endpoint stiffness of the human arm. *Journal of Neurophysiology*, 105(4):1633–1641, 2011.

Léna Jami. Golgi tendon organs in mammalian skeletal muscle: Functional properties and central actions. *Physiological Reviews*, 72(3):623–666, 1992.

M Elise Johanson, Francisco J Valero-Cuevas, and Vincent R Hentz. Activation patterns of the thumb muscles during stable and unstable pinch tasks. *The Journal of Hand Surgery*, 26(4):698–705, 2001.

Jeffrey Kerr and Bernard Roth. Analysis of multifingered hands. *The International Journal of Robotics Research*, 4(4):3–17, 1986.

Raymond J King. *Development and validation of a bond graph tendon model of the human finger with the Anatomically Correct Testbed (ACT) Hand.* PhD thesis, The University of Utah, 2015.

Hiroaki Kobayashi, Kazuhito Hyodo, and Daisuke Ogane. On tendon-driven robotic mechanisms with redundant tendons. *The International Journal of Robotics Research*, 17(5):561–571, 1998.

Sang Wook Lee, Hua Chen, Joseph D Towles, and Derek G Kamper. Effect of finger posture on the tendon force distribution within the finger extensor mechanism. *Journal of Biomechanical Engineering*, 130(5):051014, 2008.

Young-Tae Lee, Hyouk-Ryeol Choi, Wan-Kyun Chung, and Youngil Youm. Stiffness control of a coupled tendon-driven robot hand. *IEEE Control Systems*, 14(5):10–19, 1994.

JNAL Leijnse and JJ Kalker. A two-dimensional kinematic model of the lumbrical in the human finger. *Journal of Biomechanics*, 28(3):237–249, 1995.

JNAL Leijnse, JE Bonte, JMF Landsmeer, JJ Kalker, JC Van der Meulen, and CJ Snijders. Biomechanics of the finger with anatomical restrictions – the significance for the exercising hand of the musician. *Journal of Biomechanics*, 25(11): 1253–1264, 1992.

JNAL Leijnse, PM Quesada, and CW Spoor. Kinematic evaluation of the finger's interphalangeal joints coupling mechanism – variability, flexion-extension differences, triggers, locking swanneck deformities, anthropometric correlations. *Journal of Biomechanics*, 43(12):2381–2393, 2010.

Zong-Ming Li and Daniel A Harkness. Circumferential force production of the thumb. *Medical engineering & physics*, 26(8):663–670, 2004.

Zong-Ming Li and Jie Tang. Coordination of thumb joints during opposition. *Journal of Biomechanics*, 40(3):502–510, 2007.

Hong Liu, Ke Wu, Peter Meusel, Nikolaus Seitz, Gerd Hirzinger, MH Jin, YW Liu, SW Fan, T Lan, and ZP Chen. Multisensory five-finger dexterous hand: The DLR/HIT Hand II. In *IEEE/RSJ International Conference on Intelligent Robots and Systems (IROS)*, pages 3692–3697, 2008.

Mark Malhotra, Eric Rombokas, Evangelos Theodorou, Emanuel Todorov, and Yoky Matsuoka. Reduced dimensionality control for the ACT hand. In *IEEE International Conference on Robotics and Automation (ICRA)*, pages 5117–5122, 2012.

Warren S McCulloch and Walter Pitts. A logical calculus of the ideas immanent in nervous activity. *The Bulletin of Mathematical Biophysics*, 5(4):115–133, 1943.

Claudio Melchiorri, Gianluca Palli, Giovanni Berselli, and Gabriele Vassura. Development of the UB Hand IV: Overview of design solutions and enabling technologies. *IEEE Robotics & Automation Magazine*, 20(3):72–81, 2013.

Theodore E Milner, David W Franklin, Hiroshi Imamizu, and Mistuo Kawato. Central control of grasp: Manipulation of objects with complex and simple dynamics. *NeuroImage*, 36(2):388–395, 2007.

Pietro Morasso. Brute force vs. gentle taps in the control of unstable loads. *The Journal of Physiology*, 589(3):459–460, 2011.

JR Napier. The attachments and function of the abductor pollicis brevis. *Journal of Anatomy*, 86(Pt 4):335, 1952.

Raviraj Nataraj, Musa L Audu, and Zong-Ming Li. Digit mechanics in relation to endpoint compliance during precision pinch. *Journal of Biomechanics*, 48(4):672–680, 2015.

Taylor D Niehues and Ashish D Deshpande. Variable thumb moment arm modeling and thumb-tip force production of a human-like robotic hand. *Journal of Biomechanical Engineering*, 139(10):101005, 2017.

Taylor D Niehues, Julia Badger, Myron Diftler, and Ashish D Deshpande. Cartesian-space control and dextrous manipulation for multi-fingered tendon-driven hand. In *IEEE International Conference on Robotics and Automation (ICRA)*, pages 6777–6783, 2014.

Taylor D Niehues, Raymond J King, Ashish D Deshpande, and Sean Keller. Development and validation of modeling framework for interconnected tendon networks in robotic and human fingers. In *IEEE International Conference on Robotics and Automation (ICRA)*, pages 4181–4186, 2017.

Lael U Odhner and Aaron M Dollar. Stable, open-loop precision manipulation with underactuated hands. *The International Journal of Robotics Research*, 34(11): 1347–1360, 2015.

Allison M Okamura, Niels Smaby, and Mark R Cutkosky. An overview of dexterous manipulation. In *IEEE International Conference on Robotics and Automation (ICRA)*, pages 255–262, 2000.

Gianluca Palli and Salvatore Pirozzi. Miniaturized optical-based force sensors for tendon-driven robots. In *IEEE International Conference on Robotics and Automation (ICRA)*, pages 5344–5349, 2011.

Jonathan L Pearlman, Stephanie S Roach, and Francisco J Valero-Cuevas. The fundamental thumb-tip force vectors produced by the muscles of the thumb. *Journal of Orthopaedic Research*, 22(2):306–312, 2004.

Prashant Rao, Gray C Thomas, Luis Sentis, and Ashish D Deshpande. Analyzing achievable stiffness control bounds of robotic hands with coupled finger joints. In *IEEE International Conference on Robotics and Automation (ICRA)*, pages 3447–3452, 2017.

Eric Rombokas, Mark Malhotra, and Yoky Matsuoka. Task-specific demonstration and practiced synergies for writing with the ACT hand. In *IEEE International Conference on Robotics and Automation (ICRA)*, pages 5363–5368, 2011.

JL Sancho-Bru, A Perez-Gonzalez, M Vergara-Monedero, and D Giurintano. A 3-D dynamic model of human finger for studying free movements. *Journal of Biomechanics*, 34(11):1491–1500, 2001.

Veronica J Santos and Francisco J Valero-Cuevas. Reported anatomical variability naturally leads to multimodal distributions of Denavit-Hartenberg parameters for the human thumb. *IEEE Transactions on Biomedical Engineering*, 53(2):155–163, 2006.

Stanley A Schneider and Robert H Cannon. Object impedance control for cooperative manipulation: Theory and experimental results. *IEEE Transactions on Robotics and Automation*, 8(3):383–394, 1992.

Shadow Robot Company. Shadow Dexterous Hand, 2017. URL `shadowrobot.com`.

W Paul Smutz, Apichai Kongsayreepong, Richard E Hughes, Glen Niebur, William P Cooney, and Kai-Nan An. Mechanical advantage of the thumb muscles. *Journal of Biomechanics*, 31(6):565–570, 1998.

Joseph D Towles, Vincent R Hentz, and Wendy M Murray. Use of intrinsic thumb muscles may help to improve lateral pinch function restored by tendon transfer. *Clinical Biomechanics*, 23(4):387–394, 2008.

Francisco J Valero-Cuevas, Felix E Zajac, and Charles G Burgar. Large index-fingertip forces are produced by subject-independent patterns of muscle excitation. *Journal of Biomechanics*, 31(8):693–703, 1998.

Francisco J Valero-Cuevas, M Elise Johanson, and Joseph D Towles. Towards a realistic biomechanical model of the thumb: The choice of kinematic description

may be more critical than the solution method or the variability/uncertainty of musculoskeletal parameters. *Journal of biomechanics*, 36(7):1019–1030, 2003.

Francisco J Valero-Cuevas, Jae-Woong Yi, Daniel Brown, Robert V McNamara, Chandana Paul, and Hood Lipson. The tendon network of the fingers performs anatomical computation at a macroscopic scale. *IEEE Transactions on Biomedical Engineering*, 54(6):1161–1166, 2007.

Madhusudhan Venkadesan and Francisco J Valero-Cuevas. Neural control of motion-to-force transitions with the fingertip. *Journal of Neuroscience*, 28(6):1366–1373, 2008.

Thomas Wimböck, Christian Ott, and Gerd Hirzinger. Passivity-based object-level impedance control for a multifingered hand. In *IEEE/RSJ International Conference on Intelligent Robots and Systems*, pages 4621–4627, 2006.

Thomas Wimböck, Christian Ott, Alin Albu-Schäffer, Andreas Kugi, and Gerd Hirzinger. Impedance control for variable stiffness mechanisms with nonlinear joint coupling. In *IEEE/RSJ International Conference on Intelligent Robots and Systems (IROS)*, pages 3796–3803, 2008.

Thomas Wimböck, Christian Ott, Alin Albu-Schäffer, and Gerd Hirzinger. Comparison of object-level grasp controllers for dynamic dexterous manipulation. *The International Journal of Robotics Research*, 31(1):3–23, 2012.

Sarah J Wohlman and Wendy M Murray. Bridging the gap between cadaveric and in vivo experiments: A biomechanical model evaluating thumb-tip endpoint forces. *Journal of Biomechanics*, 46(5):1014–1020, 2013.

Youngmok Yun, Priyanshu Agarwal, and Ashish D Deshpande. Accurate, robust, and real-time pose estimation of finger. *Journal of Dynamic Systems, Measurement, and Control*, 137(3):034505, 2015.

Vita

Taylor Douglas Niehues attended primary and secondary school in Garden City, TX. In 2007, he entered the Mechanical Engineering Department at Texas Tech University in Lubbock, TX, where he received the degree of Bachelor of Science in 2011. In Fall 2011, he entered the Mechanical Engineering graduate program at The University of Texas at Austin, and received the degree of Master of Science in 2013. From 2012 to 2017, he was employed as a graduate research assistant in the Rehabilitation and Neuromuscular (ReNeu) Robotics Lab.

Contact Email: taylor.niehues@utexas.edu

This dissertation was typeset with LaTeX[†] by the author.

[†]LaTeX is a document preparation system developed by Leslie Lamport as a special version of Donald Knuth's TeX Program.